Abelian dyons in the maximal Abelian projection of $SU(2)$ gluodynamics

M. N. Chernodub, F. V. Gubarev, and M. I. Polikarpov
Institute of Theoretical and Experimental Physics, 117259 Moscow, Russia

(Submitted 21 December 1998)
Pis'ma Zh. Éksp. Teor. Fiz. **69**, No. 3, 161–165 (10 February 1999)

Correlations of the topological charge Q, the electric current J^e, and the magnetic current J^m in $SU(2)$ lattice gauge theory in the maximal Abelian projection are investigated. It is found that the correlator $\langle\langle QJ^eJ^m\rangle\rangle$ is nonzero for a wide range of values of the bare charge. It is shown that: *(i)* the Abelian monopoles in the maximal Abelian projection are dyons which carry *fluctuating* electric charge; *(ii)* the sign of the electric charge $e(x)$ coincides with that of the product of the monopole charge $m(x)$ and the topological charge density $Q(x)$. © *1999 American Institute of Physics.* [S0021-3640(99)00103-6]

PACS numbers: 12.38.Gc, 11.15.Ha, 14.70.Dj, 14.80.Hv

There are several approaches to the confinement problem in quantum chromodynamics (QCD).[1] The most popular is the model of the dual superconducting vacuum:[2] the vacuum is supposed to be a medium of condensed magnetic charges (monopoles). This model naturally explains the confinement phenomenon. During the last decade the method of Abelian projections[3] has been successfully used in lattice calculations in order to show that the vacuum of gluodynamics behaves as a dual superconductor (see, e.g., the reviews[4]). The numerical simulations have mostly been performed in the so-called maximal Abelian (MaA) projection.[5]

An old and rather popular model of the QCD vacuum is the instanton–anti-instanton medium (see Ref. 6 and the references cited therein). It is not clear whether the confinement phenomenon can be explained within this approach.[7] However, the instanton-based models may have some relation to the dual superconductor model, since the instantons and monopoles are interrelated, as was demonstrated analytically in Ref. 8 and numerically in Refs. 9 and 10. One can expect that the instantons may affect the properties of the Abelian monopoles in the MaA projection. Indeed, it has been shown by numerical calculations[10] that the Abelian monopole becomes the Abelian dyon in the field of a single instanton. In this paper we study the properties of the electric charge of the Abelian monopoles in the real vacuum of lattice $SU(2)$ gluodynamics.

In Section 1 we discuss the properties of Abelian monopoles in a self-dual non-Abelian field, and we introduce the lattice notation. The results of numerical simulations in the real and the cooled vacuum are described in Section 2.

1. Abelian monopoles and (anti-) self-dual fields. The (anti-) self-dual configuration of the $SU(2)$ gauge field is defined as follows:

$$F_{\mu\nu}(A) = \pm\frac{1}{2}\varepsilon_{\mu\nu\alpha\beta}F_{\alpha\beta}(A) \equiv \pm {}^*F_{\mu\nu}, \tag{1}$$

where $F_{\mu\nu}(A) = \partial_{[\mu}A_{\nu]} + i[A_\mu, A_\nu]$. In Ref. 10 the Abelian monopole in the MaA projection of lattice gluodynamics was studied in the self-dual field of the instanton. It was found that the current of the Abelian monopole is accompanied by the electric current.

The correlation of the electric and magnetic currents in the field of the instanton can be qualitatively explained as follows.[10] The MaA projection is defined[5] by the minimization of the functional $R[A^\Omega(x)]$ over the gauge transformations $\Omega(x)$, where $R[A] = \int d^4x[(A^1_\mu)^2 + (A^2_\mu)^2]$. Therefore, in this projection the off-diagonal gauge fields $A^\pm_\mu = A^1_\mu \pm iA^2_\mu$ are suppressed with respect to the diagonal gauge field A^3_μ. Thus, the commutator term $0.5\mathrm{Tr}(\sigma^3[A_\mu, A_\nu]) = \varepsilon^{3bc}A^b_\mu A^c_\nu$ in $F^3_{\mu\nu}$ is small compared to the Abelian field-strength $f_{\mu\nu}(A) = \partial_{[\mu}A^3_{\nu]}$. Therefore, in the MaA projection Eq. (1) yields:

$$f_{\mu\nu}(A) \approx \pm {}^*f_{\mu\nu}(A)\,. \tag{2}$$

Due to Eq. (2), the Abelian monopole currents must be correlated with the electric currents:

$$J^e_\mu = \partial_\nu f_{\mu\nu}(A) \approx \pm\,\partial_\nu {}^*f_{\mu\nu}(A) = J^m_\mu\,. \tag{3}$$

Therefore, in the MaA projection the Abelian monopoles are dyons on the background of (anti-) self-dual $SU(2)$ fields.

In the present publication we study the correlation of electric and magnetic currents in the vacuum of the $SU(2)$ lattice gluodynamics in the MaA projection. The definition of the Abelian monopole current on the lattice is[11]

$$J^m_\mu(y) = \frac{1}{4\pi}\sum_{\nu\lambda\rho}\varepsilon_{\mu\nu\lambda\rho}[\overline{\theta}_{\lambda\rho}(x+\hat{\nu}) - \overline{\theta}_{\lambda\rho}(x)]. \tag{4}$$

Here the function $\overline{\theta}_{\mu\nu}$ is the normalized plaquette angle $\theta_{\mu\nu}$: $\overline{\theta}_{\mu\nu} = \theta_{\mu\nu} - 2\pi k_{\mu\nu} \in (-\pi;\pi]$, $k_{\mu\nu} \in \mathbb{Z}$. The monopole current $J^m_\mu(x)$ is attached to the links of the dual lattice. One can easily show that the monopole currents are quantized, $J^m_\mu \in \mathbb{Z}$, and conserved, $\partial_\mu J^m_\mu = 0$.

The lattice electric current is defined as

$$K^e_\mu(x) = \frac{1}{2\pi}\sum_\nu\,[\overline{\theta}_{\mu\nu}(x) - \overline{\theta}_{\mu\nu}(x-\hat{\nu})]. \tag{5}$$

In the continuum limit, this equation corresponds to the usual definition: $K^e_\mu = \partial_\nu f_{\mu\nu}$. The electric currents K^e_μ are defined on the original lattice. These are conserved, i.e., $\partial_\mu K^e_\mu = 0$, but, contrary to the magnetic currents, are not quantized, i.e., $K^e_\mu \in R$.

In order to calculate the correlators of the electric and the magnetic currents, one has to define the electric current on the dual lattice or the magnetic current on the original lattice. We use the following definition of the electric current J^e_μ on the *dual* lattice:

$$J^e_\mu(y) = \frac{1}{16}\sum_{x \in {}^*C(y,\mu)}[K^e_\mu(x) + K^e_\mu(x-\hat{\mu})]\,, \tag{6}$$

where the summation in the right-hand side is over the eight vertices x of the three-dimensional cube $^*C(y,\mu)$, to which the current $J^e_\mu(y)$ is dual. As in Eq. (4), the point y lies on the dual lattice and the vertices x belong to the original lattice. The current J^e_μ defined by Eq. (6) has the standard continuum limit: $J^e_\mu = \partial_\nu f_{\mu\nu}$.

We use the simplest definition for the topological charge density:

$$Q(x) = \frac{1}{2^9 \pi^2} \sum_{\mu_1,\mu_2,\mu_3,\mu_4=-4}^{4} \varepsilon^{\mu_1,\mu_2,\mu_3,\mu_4} \mathrm{Tr}[U_{\mu_1\mu_2}(x) U_{\mu_3\mu_4}(x)], \tag{7}$$

where $U_{\mu_1\mu_2}(x)$ is the plaquette matrix. On the dual lattice the topological charge density $Q(y)$ corresponding to the monopole current $J^m_\mu(y)$ is defined by averaging over the sites nearest to the current $J^m_\mu(y)$:

$$Q(y) = \frac{1}{8} \sum_x Q(x); \tag{8}$$

the summation here is the same as in Eq. (6).

The simplest (connected) correlator of the electric and the magnetic currents is: $\langle\langle J^m_\mu J^e_\mu \rangle\rangle = \langle J^m_\mu J^e_\mu \rangle - \langle J^m_\mu \rangle \langle J^e_\mu \rangle \equiv \langle J^m_\mu J^e_\mu \rangle$, $\langle J^m_\mu \rangle = \langle J^e_\mu \rangle = 0$ is due to the Lorentz invariance. The correlator $\langle J^m_\mu J^e_\mu \rangle$ is zero due to the opposite parities of the operators J^m and J^e.

The nonvanishing correlator is $\langle\langle J^m_\mu(y) J^e_\mu(y) Q(y) \rangle\rangle$, which is both Lorentz and parity invariant. Due to equalities $\langle J^m_\mu(y) \rangle = \langle J^e_\mu(y) \rangle = \langle Q(y) \rangle = 0$ the connected correlator is:

$$G = \langle\langle J^m_\mu(y) J^e_\mu(y) Q(y) \rangle\rangle = \langle J^m_\mu(y) J^e_\mu(y) Q(y) \rangle . \tag{9}$$

The density of electric and magnetic charges depends strongly on β. To compensate this dependence we consider the normalized correlator $\overline{G}$:

$$\overline{G} = \frac{1}{\rho^e \rho^m} \langle J^m_\mu(y) J^e_\mu(y) q(y) \rangle , \tag{10}$$

where

$$\rho_{m,e} = \frac{1}{4V} \sum_l \langle |J^{m,e}_l| \rangle , \quad q(x) = \frac{Q(y)}{|Q(y)|} \equiv \mathrm{sign}\, Q(x) ,$$

V being the lattice volume (total number of sites).

2. Magnetic and electric currents: numerical study. We perform numerical simulations on the 8^4 lattice with periodic boundary conditions. We thermalize the lattice fields using the standard heat bath algorithm. All correlators for each value of β are calculated on 100 statistically independent configurations. To fix the MaA projection we use the overrelaxation algorithm of Ref. 12.

The correlator $\overline{G}$ given by Eq. (10) versus β is shown in Fig. 1. Since the product of electric and magnetic currents is correlated with the topological charge, we see that the Abelian monopole carries an electric charge which depends on the topological charge density at the Abelian monopole position.

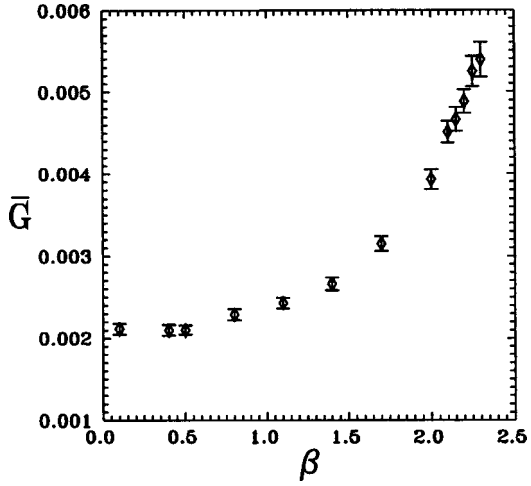

FIG. 1. The correlator $\bar{G}$, Eq. (10), versus β.

We have found that the correlator $\bar{G}$ grows during the cooling of the field configurations. This means that the strongest correlation of the electric and the magnetic charges is observed in (anti-) self-dual fields (e.g., for the instanton configuration).

In order clarify how our results are related to those of Ref. 10, we study the correlator

$$R = \frac{\langle J^m_\mu(y) J^e_\mu(y) q(y) \rangle}{\langle | J^m_\mu(y) J^e_\mu(y) q(y) | \rangle} \tag{11}$$

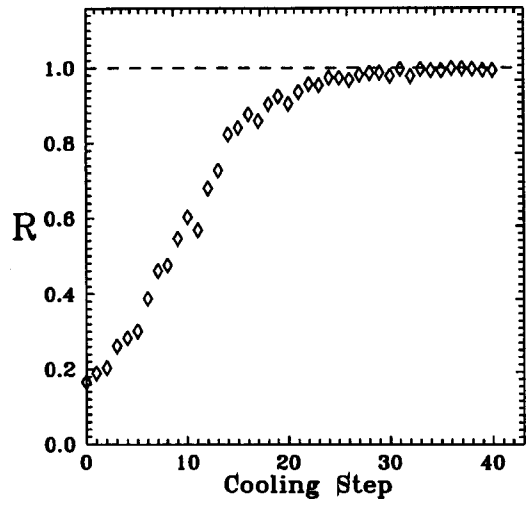

FIG. 2. The ratio R, Eq. (11), versus the number of cooling steps at $\beta = 2.2$.

in the cooled vacuum. The correlator R versus the number of the cooling steps n is shown in Fig. 2 at $\beta = 2.2$. The plateau $R = 1$ at $n > 25$ corresponds to the classical instanton configuration studied in Ref. 10. In the real (not cooled) vacuum, the field configurations are not self–dual, and we have $R < 1$ at $n = 0$.

Our results show that the Abelian monopoles in the MaA projection of $SU(2)$ gluodynamics carry a fluctuating electric charge. The sign of the electric charge is equal to that of the product of the topological charge density and the magnetic charge. The large electric charge is in the (anti-) self–dual vacuum, while in the real (not cooled) vacuum the induced charge is smaller.

M. I. P. acknowledges the kind hospitality of the Theoretical Department of the Kanazawa University, where a part of this work was done. F. V. G. is grateful for the kind hospitality of the Theoretical Physics Department of the Free University of Amsterdam. This work was supported by the grants INTAS-RFBR-95-0681, RFBR-96-02-17230a, and RFBR-96-15-96740.

[1] Yu. A. Simonov, Phys. Usp. **39**, 313 (1996); http://xxx.lanl.gov/abs/hep-ph/9709344.
[2] S. Mandelstam, Phys. Rep. **23C**, 245 (1976); G.'t Hooft, *High Energy Physics*, Zichichi, Editrice Compositori, Bolognia, 1976.
[3] G.'t Hooft, Nucl. Phys. B **190** [FS3], 455 (1981).
[4] T. Suzuki, Nucl. Phys. B (Proc. Suppl.) **30**, 176 (1993); M. I. Polikarpov, Nucl. Phys. B (Proc. Suppl.) **53**, 134 (1997); M. N. Chernodub and M. I. Polikarpov, preprint ITEP-TH-55/97; http://xxx.lanl.gov/abs/hep-th/9710205.
[5] A. S. Kronfeld, G. Schierholz, U.-J. Wiese, and M. L. Laursen, Phys. Lett. B **198**, 516 (1987); A. S. Kronfeld, G. Schierholz, and U.-J. Wiese, Nucl. Phys. B **293**, 461 (1987).
[6] T. Schaefer and E. V. Shuryak, http://xxx.lanl.gov/abs/hep-ph/9610451; Phys. Rev. D **53**, 6522 (1996).
[7] E. V. Shuryak, Phys. Lett. B **79**, 135 (1978); D. I. Diakonov and V. Yu. Petrov, Nucl. Phys. B **245**, 259 (1984); T. DeGrand, A. Hasenfratz, and T. G. Kovacs, Nucl. Phys. B **505**, 417 (1997).
[8] M. N. Chernodub, F. V. Gubarev, JETP Lett. **62**, 100 (1995); R. C. Brower, K. N. Orginos, and Chung-I Tan, Phys. Rev. D **55**, 6313 (1997).
[9] O. Miyamura and S. Origuchi, *RCNP Confinement 1995*, Osaka, Japan, March 22–26, 1995, p. 137; A. Hart and M. Teper, Phys. Lett. **371**, 261 (1996); S. Thurner *et al.*, Phys. Rev. D **54**, 3457 (1996); M. Feurstein, H. Markum, and S. Thurner, Phys. Lett. B **396**, 203 (1997); M. Fukushima *et al.*, Phys. Lett. B **399**, 141 (1997).
[10] V. Bornyakov and G. Schierholz, Phys. Lett. **384**, 190 (1996).
[11] T. A. DeGrand and D. Toussaint, Phys. Rev. D **22**, 2478 (1980).
[12] J. E. Mandula and M. Ogilvie, Phys. Low-Dimens. Semicond. Struct. **248**, 156 (1990).

Published in English in the original Russian journal. Edited by Steve Torstveit.

Effective monopole potential for $SU(2)$ lattice gluodynamics in the spatial maximal Abelian gauge

M. N. Chernodub, M. I. Polikarpov, and A. I. Veselov
Institute of Theoretical and Experimental Physics, 117259 Moscow, Russia

(Submitted 21 December 1998)
Pis'ma Zh. Éksp. Teor. Fiz. **69**, No. 3, 166–170 (10 February 1999)

We investigate the dual superconductor hypothesis in finite-temperature $SU(2)$ lattice gluodynamics in the *spatial* maximal Abelian gauge. This gauge is more physical than the ordinary maximal Abelian gauge due to absence of nonlocalities in the temporal direction. We show numerically that in the spatial maximal Abelian gauge the probability distribution of the Abelian monopole field is consistent with the dual superconductor mechanism of confinement: the Abelian condensate vanishes in the deconfinement phase and is nonzero in the confinement phase.
[S0021-3640(99)00203-0]

PACS numbers: 12.38.Gc, 11.15.Ha, 14.70.Dj, 14.80.Hv

The dual superconductor hypothesis of color confinement[1] in gluodynamics has been confirmed by various lattice calculations[2] in the so-called maximal Abelian (MaA) projection.[3] This hypothesis is based on a partial gauge fixing of a non-Abelian group up to its Abelian subgroup. After the gauge is fixed, Abelian monopoles arise due to singularities in the gauge-fixing conditions.[4] If monopoles are condensed, then the vacuum of gluodynamics behaves as a dual superconductor, and the electric charges (quarks) in such a vacuum are confined.

The MaA projection on the lattice is defined by the condition:[3]

$$\max_{\Omega} R_{\mathrm{MaA}}[U^{\Omega}], \quad R_{\mathrm{MaA}}[U]=\sum_{l} \mathrm{Tr}[\sigma_3 U_l^{+} \sigma_3 U_l], \quad l=\{x,\mu\}, \tag{1}$$

where the summation is over all lattice links and $U_{x,\mu}$ are the lattice $SU(2)$ gauge fields.

The gauge-fixing condition (1) contains time components of the gauge fields, $U_{x,4}$, and therefore Abelian operators in the MaA projection correspond to temporally nonlocal operators in terms of the original $SU(2)$ fields $U_{x,\mu}$. To show this let us consider the expectation value of the $U(1)$ invariant operator $\mathcal{O}$ in the MaA gauge:[5,6]

$$\langle \mathcal{O} \rangle_{\mathrm{MaA}}=\frac{1}{\mathcal{Z}_{\mathrm{MaA}}} \int \mathcal{D}U \exp\{-S[U]+\lambda R_{\mathrm{MaA}}[U]\} \Delta_{\mathrm{FP}}[U;\lambda] \mathcal{O}(U), \quad \lambda \to +\infty, \tag{2}$$

where $\mathcal{Z}_{\mathrm{MaA}}$ is the partition function in the fixed gauge. $\Delta_{\mathrm{FP}}[U;\lambda]$ is the Faddeev–Popov determinant:

$$1=\Delta_{\rm FP}[U;\lambda]\int \mathcal{D}\Omega\,\exp\{\lambda R_{\rm MaA}[U^{\Omega}]\},\quad \lambda\to+\infty.$$

Shifting the fields $U\to U^{\Omega^+}$ in Eq. (2) and integrating over Ω both in the nominator and denominator, we get:

$$\langle\mathcal{O}\rangle_{\rm MaA}=\langle\tilde{\mathcal{O}}_{\rm MaA}\rangle,\quad \tilde{\mathcal{O}}_{\rm MaA}(U)=\frac{\int \mathcal{D}\Omega\,\exp\{\lambda R_{\rm MaA}[U^{\Omega}]\}\,\mathcal{O}(U^{\Omega})}{\int \mathcal{D}\Omega\,\exp\{\lambda R_{\rm MaA}[U^{\Omega}]\}},$$

$\tilde{\mathcal{O}}_{\rm MaA}$ is the $SU(2)$ invariant operator. Since $\lambda\to+\infty$ we can use the saddle point approximation to calculate $\tilde{\mathcal{O}}_{\rm MaA}$:

$$\tilde{\mathcal{O}}_{\rm MaA}(U)=\frac{\Sigma_{j=1}^{N(U)}\,{\rm Det}^{1/2}M_{\rm MaA}[U^{\Omega^{(j)}}]\,\mathcal{O}(U^{\Omega^{(j)}})}{\Sigma_{k=1}^{N(A)}\,{\rm Det}^{1/2}M_{\rm MaA}[U^{\Omega^{(k)}}]},\tag{3}$$

where $\Omega^{(j)}$ corresponds to the N-degenerate global maxima of the functional $R_{\rm MaA}[U^{\Omega}]$ with respect to the regular gauge transformations Ω: $R_{\rm MaA}[U^{\Omega^{(j)}}]=R_{\rm MaA}[U^{\Omega^{(k)}}]$, $j,k=1,\ldots,N$. The matrix $M_{\rm MaA}$ is the Faddeev–Popov operator:[5]

$$M^{x,a;y,b}_{\rm MaA}[U]=\left.\frac{\partial^2 R_{\rm MaA}(U^{\Omega(\omega)})}{\partial\omega^a(x)\,\partial\omega^b(y)}\right|_{\omega=0},$$

$\Omega(\omega)=\exp\{i\omega^a T^a\}$, $T^a=\sigma^a/2$ are the generators of the gauge group, and σ^a are the Pauli matrices.

Since the gauge-fixing functional $R_{\rm MaA}$ contains time components of the gauge field U, the operator $\tilde{\mathcal{O}}(U)$ is nonlocal in time. For time-nonlocal operators there are obvious difficulties with the transition from the Euclidean to Minkowski space–time. Thus there are problems with the physical interpretation of the results obtained for Abelian operators in the MaA projection.

The MaA gauge condition can be easily modified to overcome this time-nonlocality problem. The corresponding gauge condition is given by:

$$\max_{\Omega} R_{\rm SMaA}[\hat{U}^{\Omega}],\quad R_{\rm SMaA}[U]=\sum_{\mathbf{l}}\,{\rm Tr}[\sigma_3 U^{+}_{\mathbf{l}}\sigma_3 U_{\mathbf{l}}],\quad \mathbf{l}=\{x,i\},\quad i=1,2,3,\tag{4}$$

where the summation is taken only over the spatial links $\mathbf{l}$. We refer to this projection as the spatial maximal Abelian (SMaA) projection.[1)] In the SMaA gauge the gauge-invariant operator (3) is local in time.

In this paper we study the Abelian monopole condensate Φ_c in SMaA projection. To calculate Φ_c we need the monopole creation operator $\Phi_{\rm mon}(x)$. This operator was found by Fröhlich and Marchetti[8] for compact electrodynamics and was studied numerically in Refs. 10. The Fröhlich–Marchetti operator was generalized to the Abelian projection of lattice $SU(2)$ gluodynamics in Refs. 10, where it was found that in the MaA projection the monopole field is condensed in the confinement phase and Φ_c vanishes in the deconfinement phase.[2)]

The construction[10] of the monopole creation operator for an arbitrary Abelian projection goes as follows. We parametrize the $SU(2)$ link matrix in the standard way: $U^{11}_{x\mu}=\cos\phi_{x\mu}\,e^{i\theta_{x\mu}}$; $U^{12}_{x\mu}=\sin\phi_{x\mu}\,e^{i\chi_{x\mu}}$; $U^{22}_{x\mu}=U^{11*}_{x\mu}$; $U^{21}_{x\mu}=-U^{12*}_{x\mu}$; $0\leqslant\phi\leqslant\pi/2$, $-\pi<\theta$, $\chi\leqslant\pi$. The plaquette action in terms of the angles ϕ, θ and χ can be written as follows: $S_P=0.5\mathrm{Tr}\,U_1U_2U_3^+U_4^+=S^a+S^n+S^i$, where

$$S^a=\cos\theta_P\cos\phi_1\cos\phi_2\cos\phi_3\cos\phi_4,$$

S^n and S^i describe the interaction of the fields θ and χ and self–interaction of the field χ (Ref. 5); here the subscripts $1,\ldots,4$ correspond to the links of the plaquette: $1\to\{x,x+\hat{\mu}\}$, $\ldots$, $4\to\{x,x+\hat{\nu}\}$. For a fixed Abelian projection, each term S^a, S^n, and S^i is invariant under the residual $U(1)$ gauge transformations: $\theta_{x\mu}\to\theta_{x\mu}+\alpha_x-\alpha_{x+\hat{\mu}}$, $\chi_{x\mu}\to\chi_{x\mu}+\alpha_x+\alpha_{x+\hat{\mu}}$.

The operator $\Phi_{\mathrm{mon}}(x)$ creates the monopole at the point x on the dual lattice with a cloud of dual photons; it is defined as follows:[10]

$$\Phi_{\mathrm{mon}}(x)=\exp\left\{\sum_P\tilde{\beta}[-\cos(\theta_P)+\cos(\theta_P+W_P(x))]\right\}, \tag{5}$$

where $\tilde{\beta}=\beta\cos\phi_1\cos\phi_2\cos\phi_3\cos\phi_4$, W_P is defined as[8] $W_P=2\pi\delta\Delta^{-1}(D_x-\omega_x)$. The integer valued 1-form $*_{\omega_x}$ represents the Dirac string attached to the monopole[8] and satisfies the equation $\delta{}^*\omega_x={}^*\delta_x$. The function $D_x=d_{(3)}\Delta^{-1}_{(3)}\delta_x$ represents the cloud of dual photons. Here $*_{\delta_x}$ is the lattice delta function, it is equal to unity at the site x of the dual lattice and is zero at the other sites; $d_{(x)}$ and $\Delta^{-1}_{(3)}$ are the lattice derivative and the inverse Laplace operator on a three-dimensional time-slice which includes the point x.

We study the monopole creation operator Φ_{mon} in the SMaA projection (4) on the lattices[3] $4\cdot L^3$, for $L=8,10,12,14,16$. We extrapolate the value of the monopole condensate to the infinite spatial volume ($L\to\infty$), since near the deconfinement phase transition there are strong finite-volume effects. We also impose the so-called C-periodic boundary conditions in space for the gauge fields, since the periodic boundary conditions are forbidden due to the Gauss law: we put a magnetic charge into the finite box. The C-periodic boundary conditions for the non-Abelian gauge fields[13] correspond to antiperiodic spatial boundary conditions for Abelian fields. In the case of $SU(2)$ gauge group the C-periodic boundary conditions are almost trivial: on the boundary we have $U_{x,\mu}\to\Omega^+U_{x,\mu}\Omega$, $\Omega=i\sigma_2$. Note that the gauge-fixing functionals for MaA (1) and for SMaA (4) gauges are invariant under this transformation.

The effective potential $V(\Phi)$ for the monopole field is defined via the probability distribution of the operator Φ_{mon}:[9,10]

$$V(\Phi)=-ln(\langle\delta(\Phi-\Phi_{\mathrm{mon}}(x))\rangle). \tag{6}$$

We calculate this potential numerically by the Monte Carlo method. We generate the gauge fields by the standard heat bath method, taking 2000 update sweeps to thermalize the system at each value of β. The number of gauge-fixing iterations is set by the standard condition:[14] the iterations are stopped when the matrix of the gauge transformation $\Omega(x)$ becomes close to the unit matrix: $\max_x\{1-0.5\mathrm{Tr}\,\Omega(x)\}\leqslant10^{-5}$. We check that more accurate fixing of the SMaA gauge (4) does not change our results. To calculate the probability distribution for each value of β at the lattice of definite size, we use 100

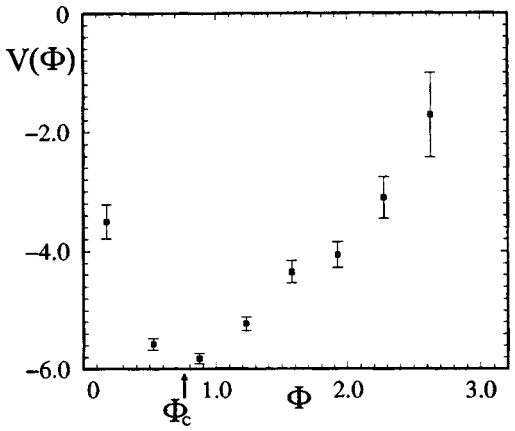

FIG. 1. Effective potential $V(\Phi)$, Eq. (6), for the confinement phase, $\beta = 1.5$.

gauge field configurations separated by 300 Monte Carlo sweeps. Then for each field configuration we calculate the value of the monopole creation operator (5) at 20 randomly chosen lattice points.

In Fig. 1 we show the effective potential (6) for the confinement phase; the lattice is 4×12^3. This potential corresponds to the Higgs type potential.[4)] The value of the monopole field Φ_c at the minimum of the minimum is equivalent to the value of the monopole condensate.

The minimum of the potential, Φ_c, versus the inverse lattice size $1/L$ is shown in Fig. 2 for two values of β. We fit the data for $\Phi_c(L)$ by the formula $\Phi_c = AL^{\alpha} + \Phi_c^{\inf}$, where A, α and $\Phi_c^{\inf}$ are the fitting parameters. We find that the best fit gives $\alpha = -1$ within the statistical errors.

Figure 3 shows the value of the monopole condensate, extrapolated to the infinite spatial volume, $\Phi_c^{\inf}$. We conclude from Fig. 3 that in the SMaA projection the infinite-

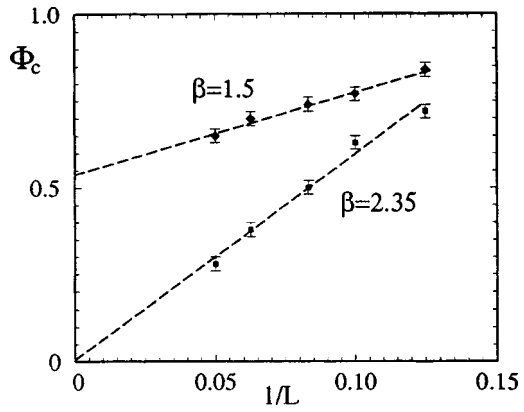

FIG. 2. Finite volume monopole condensate, Φ_c, versus the inverse spatial size of the lattice, $1/L$, at $\beta = 1.5$ and $\beta = 2.35$.

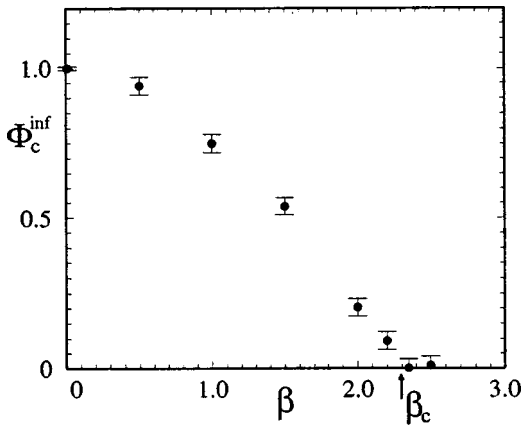

FIG. 3. Monopole condensate extrapolated to infinite volume, $\Phi_c^{\rm inf}$, versus β. The phase transition is at $\beta=\beta_c\approx 2.3$.

volume condensate $\Phi_c^{\rm inf}$ vanishes at the point of the phase transition,[5)] $\beta=\beta_c$. Thus in the SMaA projection the confining vacuum of $SU(2)$ gluodynamics behaves as a dual superconductor.

We are grateful to U.–J. Wiese and to E.–M. Ilgenfritz for interesting discussions and to E.–M. Ilgenfritz, H. Markum, M. Müller-Preussker and S. Thurner for informing us about their results prior to publication. M. N. Ch. acknowledges the kind hospitality of the Theory Division of the Max-Planck-Institute for Physics, Werner Heisenberg Institute, M. I. P. feel much obliged for the kind hospitality extended to him by the staff of Centro de Física das Interacções Fundamentais, Edifício Ciência, Instituto Superior Técnico (Lisboa) where a part of this work has been done. This work was partially supported by the grants INTAS-96-370, INTAS-RFBR-95-0681, RFBR-96-02-17230a, RFBR-97-02-17491a and RFBR-96-15-96740. The work of M. N. Ch. was supported by the INTAS Grant 96-0457 within the research program of the International Center for Fundamental Physics in Moscow.

[1)]This gauge, which was discussed by U.-J. Wiese in 1990, was recently rediscovered by D. Zwanzinger (private communication to M. I. P.), and discussed by M. Müller-Preussker at the 1997 Yukawa International Seminar on ''Non-perturbative QCD – Structure of QCD Vacuum'' (YKIS'97), 2–12 December, 1997, Yukawa Institute for Theoretical Physics, Kyoto, Japan (Ref. 7).

[2)]Similar results have been obtained for other definitions of $\Phi_{\rm mon}(x)$.[11,12]

[3)]These lattices correspond to finite temperature field theory, $T=1/4a$, where a is the lattice spacing.

[4)]In Fig. 1 the only the right half of the potential is shown on account of the positivity of the monopole operator (5); see Refs. 10 for a discussion.

[5)]It is well known that for $\beta=\beta_c\approx 2.3$ ($\beta>\beta_c$) the $SU(2)$ gauge field is in the confinement (deconfinement) phase on the lattice $L^3\times 4$.

[1] S. Mandelstam, Phys. Rep. **23C**, 245 (1976); G.'t Hooft, *High Energy Physics*, Zichichi, Editrice Compositori, Bolognia, 1976.

[2] T. Suzuki, Nucl. Phys. B (Proc. Suppl.) **30**, 176 (1993); M. I. Polikarpov, Nucl. Phys. B (Proc. Suppl.) **53**, 134 (1997); M. N. Chernodub and M. I. Polikarpov, in *Confinement, Duality and Nonperturbative Aspects of QCD*, edited by P. van Baal, Plenum Press, 1998, p. 387; http://xxx.lanl.gov/abs/hep-th/9710205; G. S. Bali, talk given at Confinement III, Newport News, VA, June 1998, http://xxx.lanl.gov/abs/hep-ph/9809351; R. W. Haymaker, to be published in Phys. Rep., http://xxx.lanl.gov/abs/hep-lat/9809094.
[3] A. S. Kronfeld, G. Schierholz, U.-J. Wiese, and M. L. Laursen, Phys. Lett. B **198B**, 516 (1987); A. S. Kronfeld, G. Schierholz, and U.-J. Wiese, Nucl. Phys. B **293**, 461 (1987).
[4] G.'t Hooft, Nucl. Phys. B **190**, [FS3] 455 (1981).
[5] M. N. Chernodub, M. I. Polikarpov, and A. I. Veselov, Phys. Lett. B **342**, 303 (1995).
[6] M. N. Chernodub, F. V. Gubarev, M. I. Polikarpov, and A. I. Veselov, Prog. Theor. Phys. **131**, 309 (1998); http://xxx.lanl.gov/abs/hep-lat/9802036.
[7] E.-M. Ilgenfritz, H. Markum, M. Müller-Preussker, and S. Thurner, talk at Lattice'98, http://xxx.lanl.gov/abs/hep-lat/9809154; S. Thurner, H. Markum, E.-M. Ilgenfritz, and M. Müller-Preussker, talk presented at ICHEP98, http://xxx.lanl.gov/abs/hep-lat/9809153; E.-M. Ilgenfritz, H. Markum, M. Müller-Preussker *et al.*, Prog. Theor. Phys. Suppl. **131**, 353 (1998); http://xxx.lanl.gov/abs/hep-lat/9804031.
[8] J. Fröhlich and P. A. Marchetti, Commun. Math. Phys. **112**, 343 (1987).
[9] L. Polley and U.-J. Wiese, Nucl. Phys. B **356**, 629 (1991); M. I. Polikarpov, L. Polley and U.-J. Wiese, Phys. Lett. B **253**, 212 (1991).
[10] A. I. Veselov, M. I. Polikarpov, and M. N. Chernodub, JETP Lett. **63**, 411 (1996); M. N. Chernodub, M. I. Polikarpov, and A. I. Veselov, Phys. Lett. B **399**, 267 (1997); Nucl. Phys. Proc. Suppl. **49**, 307 (1996).
[11] L. Del Debbio, A. Di Giacomo, and G. Paffuti, Phys. Lett. B **349**, 513 (1995); L. Del Debbio, A. Di Giacomo, G. Paffuti, and P. Pieri, Phys. Lett. B **355**, 255 (1995).
[12] N. Nakamura *et al.*, Nucl. Phys. Proc. Suppl. **53**, 512 (1997).
[13] U.-J. Wiese, Nucl. Phys. B **375**, 45 (1992); A. S. Kronfeld and U.-J. Wiese, Nucl. Phys. B **401**, 190 (1993).
[14] V. G. Bornyakov *et al.*, Phys. Lett. B **261**, 116 (1991); G. I. Poulis, Phys. Rev. D **56**, 161 (1997).

Published in English in the original Russian journal. Edited by Steve Torstveit.

The polarization of radiation in single crystals in the semiclassical approach

S. M. Darbinyan and N. L. Ter-Isaakyan*
Yerevan Physics Institute, 375036 Yerevan, Armenia

(Submitted 21 December 1998)
Pis'ma Zh. Éksp. Teor. Fiz. **69**, No. 3, 171–175 (10 February 1999)

The radiation emission spectra of polarized photons emitted from charged particles in single oriented crystals are obtained in Bayer–Katkov–Strakhovenko semiclassical approach. The results of numerical calculations are presented in the region of small angles of incidence for which the coherent theory fails but the magnetic bremsstrahlung region is not yet achieved. © *1999 American Institute of Physics.* [S0021-3640(99)00303-5]

PACS numbers: 78.70.En, 41.50.+h

The process of photon emission from charged particles at high energies in oriented single crystals is widely applied in experimental physics for the production of polarized photon beams. For sufficiently large angles of incidence ϑ_0 to the crystal axis/planes, $\vartheta_0 \gg \vartheta_v$, where ϑ_v is the characteristic angle given by $\vartheta_v = U_0/m$ (U_0 is the scale of axial/planar potential and m is the electron mass) this process is well described in the theory of coherent bremsstrahlung (CB).[1] This theory is constructed in the framework of the first Born approximation in the crystalline potential and fails at small angles and very high energies.

Recently V. N. Bayer and co-authors developed a general theory for radiation emission from high-energy particles and pair production by high-energy photons in strong crystalline fields.[2] This theory is not restricted by the first Born approximation and is based on the semiclassical character of motion of ultrarelativistic particles in strong fields. For $\vartheta_0 \gg \vartheta_v$ this theory reduces to the standard theory of CB. At very small angles $\vartheta_0 \ll \vartheta_v$ the semiclassical theory reproduces the results of the constant field approximation (CFA). For intermediate angles, $\vartheta_0 \sim \vartheta_v$, the numerical calculations in the exact theory face serious mathematical difficulties, and some approximation and modeling methods have been developed for obtaining specific numerical results. The first numerical results of the radiation emission spectra in the semiclassical theory were published in Ref. 3 (in the framework of an additional modeling assumption); exact calculations were presented in Ref. 4. In Ref. 5 an analytical method of calculation in the framework of the semiclassical approach was developed, and new numerical results were presented. Those papers demonstrate an essential difference of the exact spectra from the corresponding results of coherent theory at small angles $\vartheta_0 \leqslant \vartheta_v$. There is good agreement between the first experimental results at small angles[6,7] and those calculations.

It is very important to investigate polarization phenomena at very high energies in oriented crystals, where the CB theory doesn't work. If we could find optimal crystal orientations, which bring about large intensity enhancements of essentially polarized photons at high frequencies, it will afford us an interesting possibility for producing high-energy polarized photon beams.

In this paper the formulas for the radiation emission spectra of polarized photons are derived in the Bayer–Katkov–Strakhovenko semiclassical approach. We also present preliminary results of numerical calculations in the most interesting region of intermediate angles $\vartheta_0 \leqslant \vartheta_v$ for a planar orientation of crystal, where maximal polarization effects are expected. To carry out the ensuing time integrals of complicated oscillatory functions we have developed a computational algorithm and a special integration program which is very efficient, especially at small angles.

We start from the general semiclassical formula,[2] which gives the spectral distribution of polarized photon energy, averaged over the initial and summed over the final electron polarizations:

$$dE = \alpha \frac{d^3k}{(2\pi)^2} \int_{-\infty}^{\infty} dt_1 \int_{-\infty}^{\infty} dt_2 \frac{1}{4\varepsilon'^2} \Bigg[(\varepsilon+\varepsilon')^2 (\mathbf{e}\cdot\mathbf{v}_2)(\mathbf{e}^*\cdot\mathbf{v}_1) - \omega^2 (\mathbf{e}\cdot\mathbf{v}_1)(\mathbf{e}^*\cdot\mathbf{v}_2) + \omega^2 \left(\mathbf{v}_1\cdot\mathbf{v}_2 - 1 + \frac{1}{\gamma^2} \right) (\mathbf{e}\cdot\mathbf{e}^*) \Bigg] e^{ik'(x_1-x_2)}, \tag{1}$$

where $\alpha = 1/137$ is the fine structure constant and $k^\mu = (\omega, \mathbf{k})$ and $\mathbf{e}$ stand for the photon 4-momentum and polarization vector, respectively; ε and $\varepsilon' = \varepsilon - \omega$ are the initial and final electron energies, $k'^\mu = k^\mu \varepsilon/\varepsilon'$, $\gamma = \varepsilon/m$; $\mathbf{r}_{1,2} = \mathbf{r}(t_{1,2})$ and $\mathbf{v}_{1,2} = \mathbf{v}(t_{1,2})$ are the electron coordinates and velocities at the times $t_{1,2}$, and $x_{1,2} = (t_{1,2}, \mathbf{r}_{1,2})$.

We are going to find the radiation emission spectra of polarized photons, integrated over the emitted photon angles ϑ, φ. Therefore, the photon polarization vectors should be defined in relation to the direction that remains fixed (keeping in mind the smallness of $\vartheta, \vartheta \sim 1/\gamma$) after integration over ϑ, φ. We choose two independent polarization vectors in the following form:

$$\mathbf{e}_1 = \frac{\mathbf{n}_2 \times \mathbf{n}}{|\mathbf{n}_2 \times \mathbf{n}|}, \quad \mathbf{e}_2 = \mathbf{n} \times \mathbf{e}_1, \tag{2}$$

where $\mathbf{n} = \mathbf{k}/\omega$ and $\mathbf{n}_2$ is a unit vector transverse to the incident electron velocity $\mathbf{v}_0$; the exact direction of $\mathbf{n}_2$ can be fixed by the experimental layout. We choose $\mathbf{n}_2$ transverse to the crystal axis along which the incident electron is aligned. At $\vartheta \ll 1$ the polarization vectors $\mathbf{e}_1$ and $\mathbf{e}_2$ have the same fixed directions for any φ, and the Stokes parameters defined in terms of these vectors correspond to definite directions after integration over emitted photon angles.

Utilizing the method derived in Ref. 2, we integrate (1) over photon angles ϑ, φ and go over to the intensity $I = dE/dt$. If the longitudinal length of crystal is much larger than the radiation formation length, after averaging over electron trajectories in the crystal we can neglect the time dependence of the intensity.[2] Finally, we present the polarized photon emission spectra in terms of the Stokes parameters ξ_1, ξ_2, ξ_3:

$$\frac{dI}{d\omega}=\frac{\alpha}{\pi}\frac{m^2\omega}{\varepsilon^2}\int\frac{d^3r_0}{V}F(\mathbf{r_0},\vartheta_0)\Bigg[\int_0^\infty\frac{d\tau}{\tau}[(T_0+\gamma^2\xi_1T_1 + \gamma^2\xi_3T_3)\sin A_1+\gamma^2\xi_2T_2\cos A_1]-\frac{\pi}{2}\Bigg]. \tag{3}$$

Here $\mathbf{r}_0$ is the point of entry, V is the crystal volume, the integration over $\mathbf{r}_0$ performs an averaging over electron trajectories in the crystal, and $F(\mathbf{r}_0,\vartheta_0)$ is the coordinate distribution function at given value of ϑ_0. The quantities of $A_1=A_1(\tau)$ and $T_i=T_i(\tau), i=0,1,2,3,$ in (3) are defined as follows:

$$A_1=\frac{m^2\omega}{2\varepsilon\varepsilon'}\tau\left[1+\gamma^2\left[\frac{1}{\tau}\int_{-\tau/2}^{\tau/2}\mathbf{v}_\perp^2(t)\,dt-\mathbf{a}_\perp^2(\tau)\right]\right], \tag{4}$$

$$T_0=1+\tfrac{1}{4}\varphi(\varepsilon)\gamma^2(\mathbf{v}_{1\perp}-\mathbf{v}_{2\perp})^2\,, \tag{5}$$

$$T_1=-2a_xa_y+a_y(v_{1x}+v_{2x})+a_x(v_{1y}+v_{2y})-(v_{1x}v_{2y}+v_{1y}v_{2x}), \tag{6}$$

$$T_2=\frac{\varphi(\varepsilon)}{2}\mathbf{a}\cdot(\mathbf{v}_1\times\mathbf{v}_2), \tag{7}$$

$$T_3=a_y^2-a_x^2+a_x(v_{1x}+v_{2x})-a_y(v_{1y}+v_{2y})-(v_{1x}v_{2x}-v_{1y}v_{2y}), \tag{8}$$

where

$$\mathbf{a}(\tau)=\frac{1}{\tau}\int_{-\tau/2}^{\tau/2}\mathbf{v}(t)dt,\quad \varphi(\varepsilon)=\frac{\varepsilon'}{\varepsilon}+\frac{\varepsilon}{\varepsilon'},\quad \mathbf{v}_\perp=(v_x,v_y),$$

$$\mathbf{v}_1=\mathbf{v}(-\tau/2),\quad \mathbf{v}_2=\mathbf{v}(\tau/2).$$

The Stokes parameters and projections of vectors correspond to the frame defined by following unit vectors:

$$\hat{\mathbf{e}}_x=\mathbf{n}_2\times\mathbf{v}_0,\ \hat{\mathbf{e}}_y=\mathbf{n}_2\,,\ \hat{\mathbf{e}}_z=\mathbf{v}_0\,. \tag{9}$$

The formulas for the polarized photon emission spectra in the semiclassical approach were derived earlier, in Ref. 2, and an example of the numerical calculations was presented in Ref. 3. Our results for unpolarized photons (T_0) and circularly polarized photons (T_2) agree with those of Ref. 2. For linear polarization (T_1 and T_3) our formulas are completely different, and the results of our numerical calculations differ even qualitatively from those of Ref. 3. The difference stems from an improper choice of the photon polarization vectors in Ref. 2.[1)]

For further calculations we shall use the rectilinear trajectory approximation, which, strictly speaking, is valid for $\vartheta_0\gg\vartheta_c$, where ϑ_c is the Lindhard channeling angle.[10] We present the numerical calculations for $\varepsilon=150$ GeV and a $\langle 001\rangle$ aligned diamond single crystal at temperature $T=293$ K; ϑ_0 is the angle of the vector $\mathbf{v}_0$ to this axis, and φ_0 is the angle between the the plane $\{1\bar{1}0\}$ and the projection of $\mathbf{v}_0$ onto the $\{001\}$ plane. The calculations are carried out for a uniform distribution. We use the Molière potential of an isolated atom. In Fig. 1 the gradually changing intensity and polarization spectra are

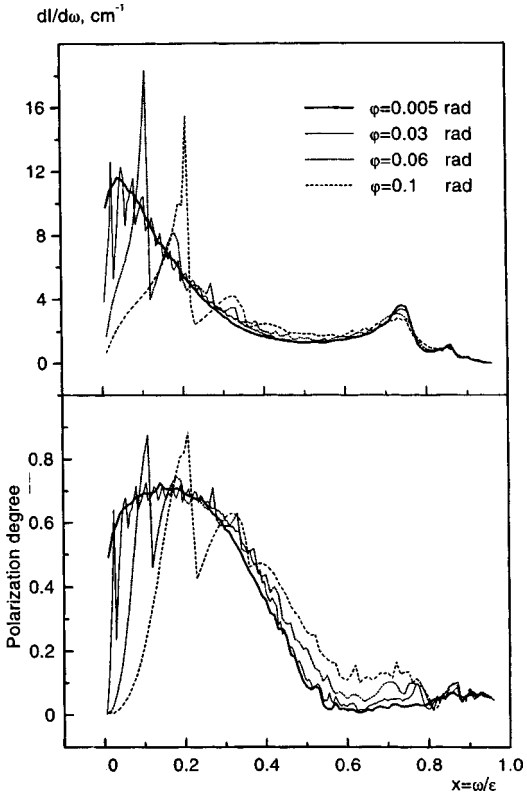

FIG. 1. Changes of intensity and polarization spectra for decreasing φ_0 at fixed ϑ_0.

presented for decreasing values of φ_0 at fixed ϑ_0 (transition to a purely planar orientation). The behavior of the unpolarized intensity generally agrees with the results of Ref. 4. The shape of the spectra is determined by the competition of coherent effects, which are determined by the long-time region $\tau \geqslant 1/q_z$ in the time integrals in (3), and magnetic bremsstrahlung effects, which come from the short-time region $\tau \ll 1/q_z$. As compared with the CB results, the intensity of the coherent peaks decreases, the peaks change their form and are shifted to lower frequencies ω. One can also see that new peaks and dips appear.[4] At the same time, as φ decreases, the magnetic bremsstrahlung effects begin to contribute and bring about an overall increase of the intensity. They are more strongly manifested at higher electron energies and lower radiated frequencies. Over a wide range of angles the radiation has an essentially linear polarization. The circular polarization doesn't vanish but is practically negligible ($\xi_2 \leqslant 0.01$). As in the CB theory, the spectral distribution of the degree of polarization repeats, in general, the structure of the intensity distribution, i.e., the peaks of intensity and peaks of polarization are situated at the same frequencies.

It is worth noting that in the most interesting region of large $x \geqslant 0.5-0.6$ the photon emission spectra and polarization could be satisfactory described in (unmodified) coherent theory down to rather small angles. In Fig. 2 we present a comparison of the semiclassical and coherent approaches.

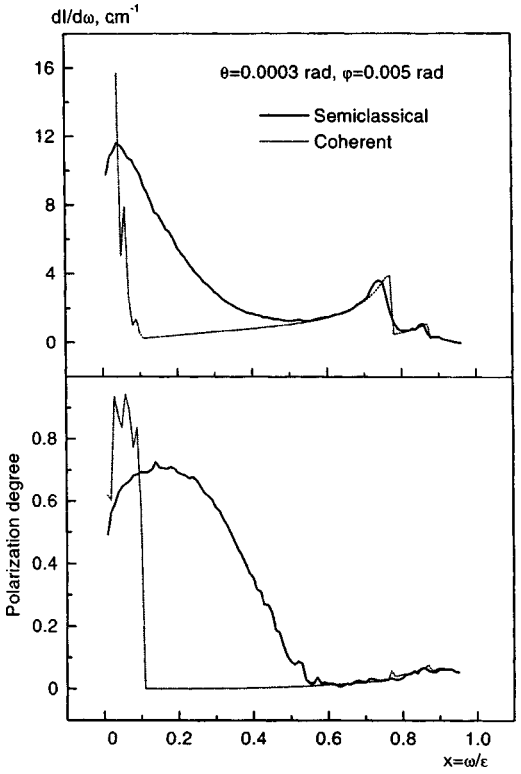

FIG. 2. Comparison of the spectral distributions of the intensity and degree of polarization in the coherent[1] and semiclassical[2] approaches at small angles of incidence.

When $\varphi_0 \to 0$ at fixed ϑ_0, the reciprocal vectors q_z which contribute to the sums in Eq. (3) form different groups such that each vector q_z from a given group tends to the same limit, $q_z \to q_z^{(i)}$, $(i=1,2,3,\ldots)$. The first group of vectors, which tend to zero, $q_z^{(i)}=0$, determine the magnetic bremsstrahlung contribution in the range of small ω. This contribution is what brought about the large maximum of the degree of linear polarization (0.6–0.8) at $x=\omega/\varepsilon=0.1-0.3$. The radiation is polarized in the $\{110\}$ plane $(\xi_1 \sim 0)$. The groups of vectors that tend to nonvanishing limits $(q_z^{(i)} \neq 0)$ correspond to a number of high frequency peaks. For sufficiently high frequencies $(x \geqslant 0.6)$ the shape and position of these peaks can be approximately described in the coherent theory (Fig. 2). The magnitude of the peaks is determined, approximately, as a sum of coherent contributions of reciprocal vectors with given $q_z^{(i)}$. For polarized spectra these contributions could be of different sign, or some contributions could vanish. Therefore, the polarization in the region of the high-ω peaks depends strongly on the crystal orientation and is relatively small. For instance, for a $\langle 001 \rangle$ aligned crystal, in the region of the main high-frequency peak the individual contributions practically compensate each other, and the degree of polarization is very small. For the $\langle 110 \rangle$ orientation, in the region of a similar peak the main contributions do not compensate one another, and the degree of polarization turns out to be substantially higher (Fig. 3). Pronounced high-energy-photon

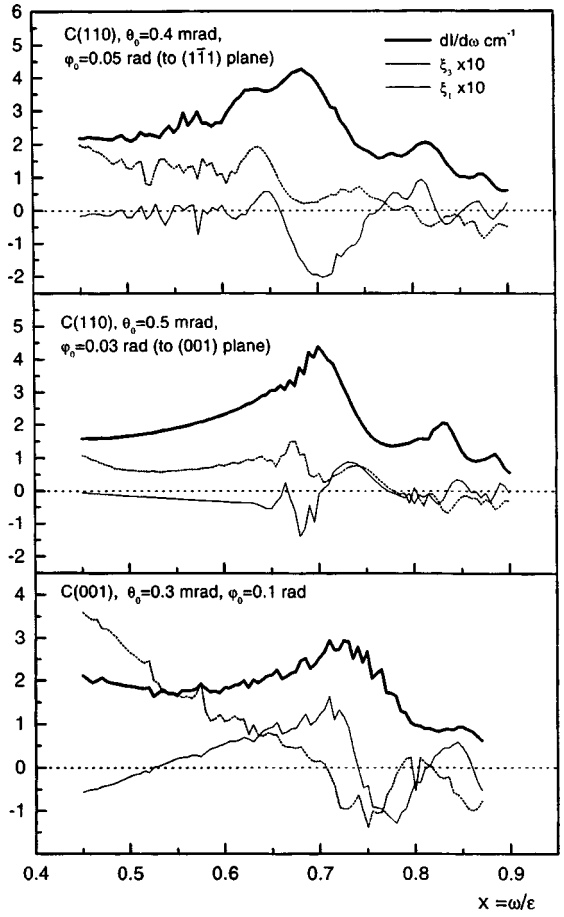

FIG. 3. The spectral distribution of the intensity and Stokes parameters in the region of the high-energy photon peaks for $\langle 001 \rangle$ and $\langle 110 \rangle$ oriented diamond single crystals at $\varepsilon = 150$ GeV.

maxima in the radiation emission have been observed experimentally at CERN[6] in diamond and Si crystals. A discussion is going on as to the possibility of utilizing this effect for producing high-energy polarized photon beams.

More-precise calculations for different crystal orientations over a wide range of incident electron angles and energies will be presented in subsequent papers.

This work was supported by the ISTC grant, Project A-099. One of us (N. T) is grateful to Prof. R. Avakian for invitation to participate in this project.

*e-mail: terisaak@jerewan1.yerphi.am

[1)]When the e-print version of this paper[8] was published, V. M. Strakhovenko informed us that in the updated English edition of their book[9] the polarized photon emission spectra have been corrected and now coincide with our corresponding Eqs. (6)–(8).

[1] M. L. Ter-Mikaelyan, *High Energy Electromagnetic Processes on Condensed Media*, Wiley-Interscience, New York, 1972.
[2] V. N. Bayer, V. M. Katkov, and V. M. Strakhovenko, *Electromagnetic Processes in Oriented Single Crystals at High Energy* [in Russian], Nauka, Novosibirsk, 1989.
[3] V. N. Bayer, V. M. Katkov, and V. M. Strakhovenko, Nucl. Instrum. Methods Phys. Res. B **69**, 258 (1992).
[4] Yu. V. Kononets and I. S. Tupitsyn, JETP Lett. **59**, 516 (1994).
[5] V. M. Strakhovenko, Nucl. Instrum. Methods Phys. Res. B **145**, 120 (1998).
[6] R. Mendenwaldt, S. P. Møller, B. N. Jensen *et al.*, Phys. Lett. B **281**, 153 (1992).
[7] A. Belkacen, G. Bologna, M. Chevallier *et al.*, Phys. Rev. Lett. **58**, 1196 (1987).
[8] S. M. Darbinyan, N. L. Ter-Isaakyan, http://xxx.lanl.gov/abs/hep-ph/9809559.
[9] V. N. Bayer, V. M. Katkov, and V. M. Strakhovenko, *Electromagnetic Processes at High Energies in Oriented Single Crystals*, World Scientific, Singapore, 1998.
[10] J. Lindhard, Mat. Fys. Medd. K. Dan. Vidensk. Selsk. **34**, 14 (1965).

Precocious asymptopia for charm from the running BFKL

N. N. Nikolaev*
Institut für Kernphysik, Forschungszentrum Jülich, D-52425 Jülich, Germany; L. D. Landau Institute of Theoretical Physics, Russian Academy of Sciences, 117940 Moscow, Russia

V. R. Zoller**
Institute of Theoretical and Experimental Physics, 117218 Moscow, Russia

(Submitted 22 December 1998)
Pis'ma Zh. Éksp. Teor. Fiz. **69**, No. 3, 176–180 (10 February 1999)

The running BFKL equation gives rise to a series of moving poles in the complex j plane. The corresponding eigenfunctions (color dipole cross sections) are oscillatory functions of the color dipole size r. The first nodes for all subleading solutions (color dipole cross sections) are clustered at $r_1 \sim 0.1$ fm. Therefore the processes dominated by dipole sizes $r \sim r_1$ are free of subleading BFKL corrections. An example of practical importance is the leptoproduction of charm. Over a wide range of Q^2 the calculated $F_2^{cc}(x,Q^2)$ is exhausted by the leading BFKL pole and gives a perfect description of the experimental data.
 [S0021-3640(99)00403-X]

PACS numbers: 12.38.Gc

The generalized Balitskii–Fadin–Kuraev–Lipatov (BFKL)[1] equation for the interaction cross section $\sigma(x,r)$ of the color dipole r with the target reads[2]

$$\frac{\partial \sigma(x,r)}{\partial \log(1/x)} = \mathcal{K} \otimes \sigma(x,r), \tag{1}$$

where x is the Bjorken variable. The kernel $\mathcal{K}$ is related to the flux of the Weizsäcker-Williams soft gluons $|\mathbf{E}(\boldsymbol{\rho}_1) - \mathbf{E}(\boldsymbol{\rho}_2)|^2$. Asymptotic freedom (AF) dictates that the chromoelectric fields $\mathbf{E}(\boldsymbol{\rho})$ be calculated with the running QCD charge $g_S(r_m) = \sqrt{4\pi\alpha_S(r_m)}$ taken at shortest relevant distance $r_m = \min\{r,\rho\}$, and

$$\mathbf{E}(\boldsymbol{\rho}) = g_S(r_m)\boldsymbol{\rho}/\rho^2 \times (\text{screening factor}).$$

Within the infrared regularization scheme described in Refs. 2–5

$$\mathbf{E}(\boldsymbol{\rho}) = g_S(r_m)\frac{\boldsymbol{\rho}}{\rho R_c} K_1(\rho/R_c)\,, \tag{2}$$

where $K_1(x)$ is the modified Bessel function. Our numerical results are for a Yukawa screening radius $R_c = 0.27$ fm. Analysis of the lattice QCD data on the field-strength

correlators suggests a similar value of R_c (Ref. 6). The running coupling thus introduced may not exhaust all NLO effects but it correctly describes the crucial enhancement of long-range and suppression of short-range effects by AF.

Our findings on the running BFKL equation which are of prime importance for the problem under discussion are as follows.[7,8] The spectrum of the running BFKL equation is a series of moving poles $\mathbb{P}_n$ in the complex j plane, with eigenfunctions

$$\sigma_n(x,r)=\sigma_n(r)\exp(\Delta_n \log(1/x)) \tag{3}$$

which are solutions of

$$\mathcal{K}\otimes\sigma_n=\Delta_n\sigma_n(r)\,. \tag{4}$$

The leading eigenfunction $\sigma_0(r)$ is node-free. The subleading $\sigma_n(r)$ has n nodes. The intercepts Δ_n closely, to better than 10%, follow the law

$$\Delta_n=\frac{\Delta_0}{(n+1)} \tag{5}$$

suggested earlier by Lipatov.[9] The intercept of the leading pole trajectory, with our specific choice of the infrared regulator, $R_c=0.27$ fm, is $\Delta_0\equiv\Delta_{\mathbb{P}}=0.4$. The subleading $\sigma_n(r)$ represented in terms of $\mathcal{E}(r)=\sigma_n(r)/r$ is, to a crude approximation, similar to Lipatov's quasi-classical eigenfunctions[9]

$$\mathcal{E}_n(r)\sim\cos[\phi(r)]\,.$$

With $R_c=0.27$ fm the node of $\sigma_1(r)$ is located at $r=r_1\simeq 0.05-0.06$ fm, and for larger n the first node moves to a somewhat larger distance $r\sim 0.1$ fm. Hence $\sigma(x,r_1)$ is dominated by $\sigma_0(x,r_1)$. This observation explains the precocious asymptopia for the dipole cross section

$$\sigma(x,r)\propto(1/x)^{\Delta_{\mathbb{IP}}}$$

at $r\sim 0.1$ fm, derived previously from numerical studies of the running BFKL equation.[3–5] Consequently, by zooming at $\sigma(x,r_1)$ one can readily measure $\Delta_{\mathbb{P}}$. The point we want to make here is that because $r_1\sim 1/m_c$, the excitation of open charm provides the desired zooming. Indeed, we shall demonstrate that the suppression of the subleading BFKL terms in $F_2^{c\bar{c}}(x,Q^2)$ is a remarkably strong effect.[1)]

The color dipole representation for the charm structure function (SF) reads[11]

$$F_2^{c\bar{c}}(x,Q^2)=\frac{Q^2}{4\pi\alpha_{em}}\langle\sigma\rangle=\frac{Q^2}{4\pi\alpha_{em}}\int_0^1 dz\int d^2\mathbf{r}\,|\Psi^{c\bar{c}}(z,r)|^2\sigma(x,r)\,. \tag{6}$$

Starting with the BFKL–Regge expansion

$$\sigma(x,r)=\sigma_0(r)(x_0/x)^{\Delta_0}+\sigma_1(r)(x_0/x)^{\Delta_1}+\sigma_2(r)(x_0/x)^{\Delta_2}+\ldots \tag{7}$$

with Δ_n as determined in Refs. 7 and 8, we arrive at the BFKL–Regge expansion for the charm SF,

$$F_2^{c\bar{c}}(x,Q^2)=\sum_n f_n^{c\bar{c}}(Q^2)(x_0/x)^{\Delta_n}\,, \tag{8}$$

where the charm eigen-SF is as follows:

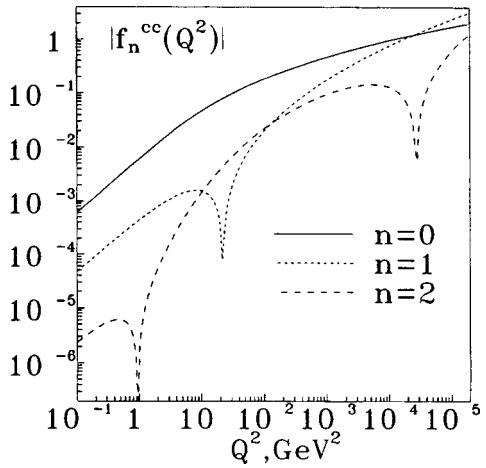

FIG. 1. Modulus of the charm eigen-SF $|f_n^{cc}(Q^2)|$ for the BFKL poles with $n=0,1,2$.

$$f_n^{cc}(Q^2)=\frac{Q^2}{4\pi\alpha_{em}}\langle\sigma_n\rangle\,. \tag{9}$$

In conjunction with the explicit form[11] of the $c\bar{c}$ light-cone wave function $\Psi^{cc}(z,r)$,

$$|\Psi_T^{cc}(z,r)|^2=\frac{8\alpha_{em}}{3(2\pi)^2}\{[z^2+(1-z)^2]\varepsilon^2K_1(\varepsilon r)^2+m_c^2K_0(\varepsilon r)^2\}, \tag{10}$$

where $K_{0,1}(x)$ are the modified Bessel functions, $\varepsilon^2=z(1-z)Q^2+m_c^2$, $m_c=1.5$ GeV is the c-quark mass, and z is the light-cone fraction of photon's momentum carried by the quark of the $c\bar{c}$ pair, Eqs. (6) and (9) show that the integral over r in (6) is dominated by

$$Q^{-2}\lesssim r^2\lesssim m_c^{-2}\,.$$

Indeed, making use of the properties of modified Bessel functions, after the z integration one can write

$$f_n^{cc}(Q^2)\propto\int_{1/Q^2}^{1/m_c^2}\frac{dr^2}{r^2}\,\frac{\sigma_n(r)}{r^2}\,. \tag{11}$$

TABLE I.

n	a_n	c_n	r_n^2, GeV^{-2}	R_n^2, GeV^{-2}	$z_n^{(1)}$	$z_n^{(2)}$	δ_n
0	0.0214	0.2619	0.3239	0.2846			
1	0.0782	0.0352	0.0793	0.2958	0.2499		1.9249
2	0.0044	0.0362	0.0884	0.2896	0.0175	3.447	1.7985

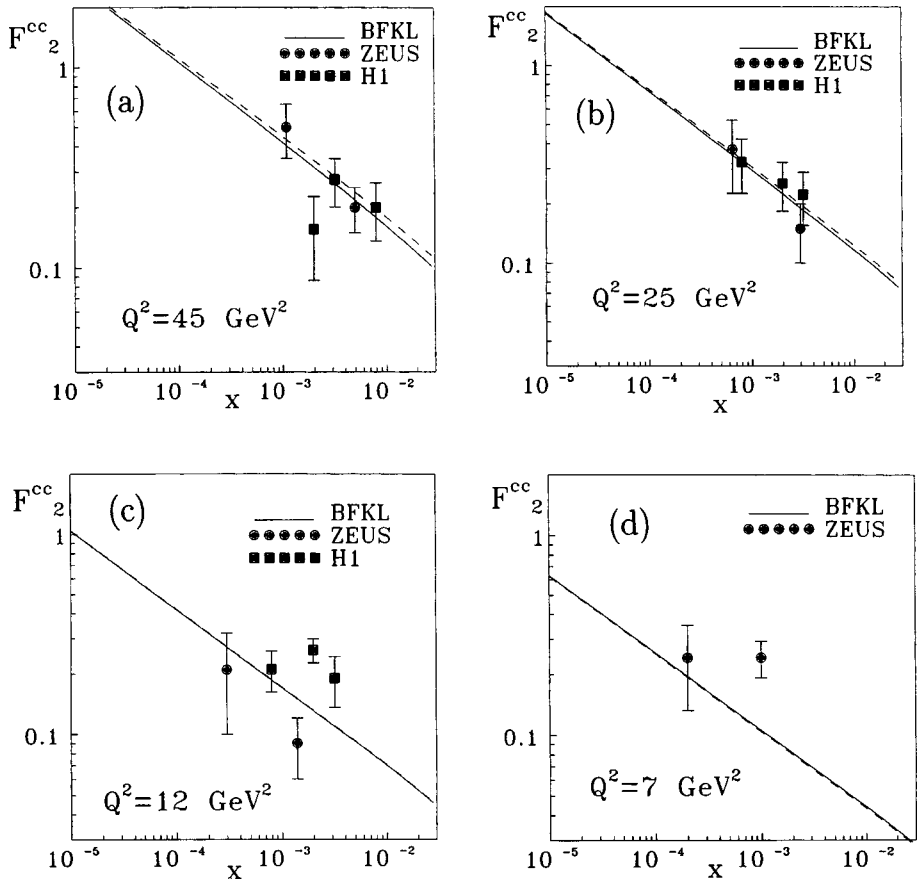

FIG. 2. The predicted charm structure function $F_2^{cc}(x,Q^2)$ (solid line) as compared with the H1 and ZEUS data. The contribution of the leading pole with $\Delta_{\mathbf{P}}=0.4$ is shown by the dashed line. a: $Q^2=45$ GeV^2, b: $Q^2=25$ GeV^2, c: $Q^2=12$ GeV^2, d: $Q^2=7$ GeV^2.

The dipole cross section $\sigma_n(r)$ in (11) is an oscillating function of r with the first node located inside the integration region. Then in a broad range of Q^2 one has strong cancellations in (11) for the subleading poles, which result in leading-pole dominance in charm production (Fig. 1). For large Q^2, far beyond the nodal region, the effect of the cancellations disappears, and

$$f_n^{cc}(Q^2)\propto[\alpha_S(Q^2)]^{-\gamma_n} \tag{12}$$

with $\gamma_n=4/3\Delta_n$.

For practical purposes it is convenient to represent $f_n^{cc}(Q^2)$ in an analytical form. The parametrization for the leading-pole SF reads

$$f_0(Q^2)=a_0\frac{R_0^2Q^2}{1+R_0^2Q^2}[1+c_0\log(1+r_0^2Q^2)]^{\gamma_0}, \tag{13}$$

where $\gamma_0=4/3\Delta_0$.

For $n \geqslant 1$ the functions $f_n(Q^2)$ can be approximated by

$$f_n(Q^2) = a_n f_0(Q^2) \frac{1+R_0^2 Q^2}{1+R_n^2 Q^2} \prod_{i=1}^{n} \left(1 - \frac{z}{z_n^{(i)}}\right), \tag{14}$$

where

$$z = [1 + c_n \log(1 + r_n^2 Q^2)]^{\gamma_n} - 1 \tag{15}$$

and

$$\gamma_n = \gamma_0 \delta_n \tag{16}$$

with the parameters listed in Table I.

In Fig. 2 our predictions for the charm structure function are compared with data from H1[12] and ZEUS.[13] We correct for threshold effects by the rescaling[14] $x \to x(1 + 4m_c^2/Q^2)$. It follows from both Fig. 1 and Fig. 2 that the charm production in a wide range of photon virtualities, $Q^2 \lesssim 10^2$ GeV^2, provides a unique opportunity for getting a hold on the elusive BFKL asymptotic behavior and measuring Δ_{P} at the currently available x.

*e-mail: kph154@ikp301.ikp.kfa-juelich.de
**e-mail: zoller@heron.itep.ru
[1)]The preliminary results were reported at the DIS'98 Workshop.[10]

[1] E. A. Kuraev, L. N. Lipatov, and V. S. Fadin, Sov. Phys. JETP **44**, 443 (1976); **45**, 199 (1977); Ya. Ya. Balitskii and L. N. Lipatov, Sov. J. Nucl. Phys. **28**, 822 (1978).
[2] N. N. Nikolaev, B. G. Zakharov, and V. R. Zoller, JETP Lett. **59**, 8 (1994).
[3] N. N. Nikolaev, B. G. Zakharov, and V. R. Zoller, JETP **105**, 1498 (1994).
[4] N. N. Nikolaev and B. G. Zakharov, Phys. Lett. B **327**, 157 (1994).
[5] N. N. Nikolaev and B. G. Zakharov, Phys. Lett. B **333**, 250 (1994).
[6] E. Meggiolaro, Report No. #hd-thep-98-34.
[7] V. R. Zoller, in *Proceedings of the Fifth International Workshop on DIS and QCD (DIS'97)*, Chicago, Ill., 1997.
[8] N. N. Nikolaev, B. G. Zakharov, and V. R. Zoller, JETP Lett. **66**, 138 (1997).
[9] L. N. Lipatov, Sov. Phys. JETP **63**, 904 (1986).
[10] V. R. Zoller, in *Proceedings of the Sixth International Workshop on DIS and QCD (DIS'98)*, Brussels, 1998.
[11] N. N. Nikolaev and B. G. Zakharov, Z. Phys. C **49**, 607 (1991).
[12] H1 collaboration (C. Adloff *et al.*), Z. Phys. C **72**, 593 (1996).
[13] ZEUS collaboration (J. Breitweg *et al.*), Phys. Lett. B **407**, 402 (1997).
[14] V. Barone, M. Genovese, N. N. Nikolaev *et al.*, Phys. Lett. B **268**, 279 (1991).

Published in English in the original Russian journal. Edited by Steve Torstveit.

Total rates of nuclear capture of negative muons in the isotopes ^{132}Xe and ^{40}Ar

T. N. Mamedov,* V. G. Grebinnik, K. I. Gritsaĭ, V. N. Duginov, V. A. Zhukov, V. G. Ol'shevskiĭ, and A. V. Stoĭkov
Joint Institute of Nuclear Research, 141980 Dubna, Moscow Region, Russia

(Submitted 10 January 1999)
Pis'ma Zh. Éksp. Teor. Fiz. **69**, No. 3, 181–183 (10 February 1999)

The lifetimes of a negative muon in the isotopes ^{132}Xe and ^{40}Ar in the solid phase are measured. The lifetime of μ^- in the $1s$ state of the isotope ^{132}Xe is $\tau(^{132}\text{Xe}) = 101.7 \pm 1.7$ ns, which corresponds to a total nuclear capture rate $\Lambda_c(^{132}\text{Xe}) = 9.4 \pm 0.2\ \mu\text{s}^{-1}$. The lifetime of μ^- in the isotope ^{40}Ar, viz., $\tau(^{40}\text{Ar}) = 568 \pm 6$ ns, corresponding to a capture rate $\Lambda_c(^{40}\text{Ar}) = 1.31 \pm 0.01\ \mu\text{s}^{-1}$, is obtained to several times better accuracy as compared to previously published results. © *1999 American Institute of Physics.* [S0021-3640(99)00503-4]

PACS numbers: 23.40.−s, 27.60.+j, 27.40.+z

The nuclear capture of negative muons is due to the weak interaction. One characteristic of this process, specifically, the total rate of nuclear capture of μ^- is important for constructing theoretical models describing this process, which can be useful for expanding our knowledge of nuclear structure. The rate of nuclear capture of negative muons has been measured for most elements in the periodic table.[1,2] Until recently, however, there has been no information about the rate of nuclear capture in the isotopes of Kr and Xe. At the same time, it is of interest to study these elements from the standpoint (besides that of filling in missing tabular data) of obtaining information about the isotopic dependence of the rate of μ^- capture and the dependence of the capture rate on the nuclear spin, since the Xe and Kr nuclei have a rich set of isotopes, some of which have nonzero spin.

We have previously[3] measured the rate of nuclear capture of μ^- in the isotopes ^{84}Kr and ^{132}Xe. In the present letter we report the results of measurements for the isotope ^{132}Xe and we present substantially refined data, compared with previous works,[4–6] on the μ^- capture rate in ^{40}Ar.

The experiment was performed in a separated beam of negative muons with a momentum 125 MeV/c from the synchrocylotron at the Laboratory of Nuclear Problems at the Joint Institute for Nuclear Research.[7] The experiment, performed by the conventional μSR method, consisted in measuring the total rate of vanishing of muons from the $1s$ state of the isotope under study by detecting the electrons from $\mu^- \to e^-$ decay. The experimental arrangement and the details of the setup are described in Ref. 8.

The experimental gas (Xe or Ar) was allowed to condense in a cooled target chamber and then frozen at a temperature close to the temperature of liquid nitrogen. The

materials for the target chamber were chosen so that the μ^- lifetime in them would differ substantially from the expected lifetime in Xe and Ar. The chamber for Xe was made of AD1-grade aluminum (99.5% pure) and the chamber for Ar was made of M1-grade copper (99.9% pure).

The composition of the xenon employed in the experiment was as follows: ^{132}Xe — 97.54%, ^{131}Xe — 2.45%, ^{134}Xe $<0.05\%$, other impurities $<0.01\%$. High-purity natural argon (^{40}Ar — 99.6%, ^{36}Ar — 0.337%, ^{38}Ar $<$ 0.063%) with the impurities of other gases not exceeding 0.002%, was used in the experiment.

The experiments were performed in a 1755 Oe external magnetic field directed perpendicular to the direction of the muon spin. The magnetic field was used to measure the residual polarization of the negative muons in the $1s$ level of the Ar and Xe atoms.

The time resolution of the apparatus (FWHM of the peak due to the transiting particles) was 2.5 ns.

The spectra obtained contained contributions from the stopping of muons in carbon, copper, or aluminum, which are present in the scintillators and target-chamber materials. For this reason the experimental data were fit with a function

$$N(t)=\sum_x N_x e^{-t/\tau(x)}[1+a_x\cos(\omega_x t+\varphi)]+\mathrm{Bg}, \tag{1}$$

where $N_x, \tau(x), a_x, \omega_x, \varphi_x$, and Bg are, respectively, the normalization factor, the muon lifetime in the $1s$ state, the observed asymmetry factor of the angular distribution of electrons from $\mu^-\to e^-$ decay, the muon spin precession frequency, the initial precession phase, and the random-coincidence background. The index x refers to ^{132}Xe (^{40}Ar), Al (Cu), and C.

The data were analyzed by the least-squares method. Aluminum and copper nuclei possess nonzero spin. As follows from the experimental data,[9,10] for aluminum and copper the precession amplitudes a_{Al} and a_{Cu} corresponding to the hyperfine interaction of the muon spin and the nuclear spins in the states $F^+=I\pm S_\mu$ are practically zero. For this reason, in analyzing the spectra for Xe and Ar we neglected the second term in the brackets for Al and Cu, respectively. The muon lifetimes in Al and Cu were obtained from the data in Ref. 2: $\tau(\mathrm{Al})=864.0\pm 2.0$ ns and $\tau(\mathrm{Cu})=163.5\pm 1.0$ ns. The parameters for the element under study and the carbon present in the scintillation counter and the Mylar windows of the vacuum housing of the cryostat were varied as free parameters. As a result of fitting the spectra, it was found that the random-coincidence background Bg in the measurements with Xe or Ar is no more than 0.3–0.4% of the total contribution $N_x(\Sigma N_x)$.

Residual polarization of the negative muons at the precession frequency of the free spin was not found in solid xenon and argon, within the limits of experimental error (1.5%).

The spectrum of the temporal distribution obtained for the electrons from $\mu^-\to e^-$ decay in the experiment with xenon is presented in Fig. 1. The contributions from the isotope under study and from impurities are clearly seen in this spectrum. Analysis of the spectra gave the following values of the lifetimes: $\tau(^{132}\mathrm{Xe})=101.7\pm 1.7$ ns and $\tau(^{40}\mathrm{Ar})=568\pm 6$ ns. The muon capture rate in Xe and Ar nuclei was calculated from the

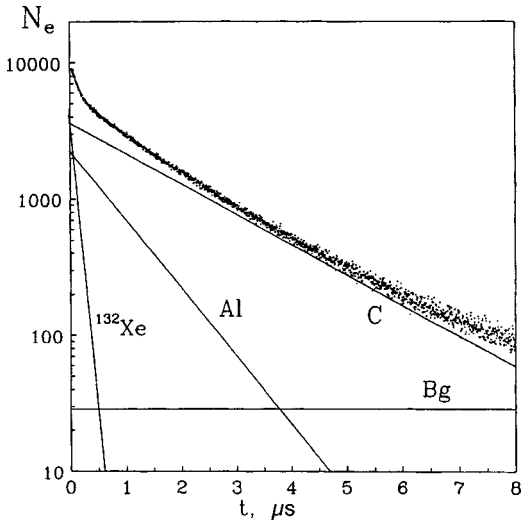

FIG. 1. Spectrum of the temporal distribution of the electrons from $\mu^- \to e^-$ decay. The target chamber is filled with solid ^{132}Xe. The straight lines show the contributions to the spectrum from the individual components.

formula $\tau^{-1} = Q\Lambda_d + \Lambda_c$, where Λ_d is the free-muon decay rate (for which the reciprocal of the μ^+ lifetime, equal to 2197.03 ± 0.04 ns,[11] was used), Q is the suppression factor for the decay rate of bound muons,[12] and Λ_c is the rate of nuclear capture of a muon. The factor Q is 0.91 for xenon and 0.99 for argon. The following capture rates were obtained as a result: $\Lambda_c(^{132}\text{Xe}) = 9.4 \pm 0.2\ \mu\text{s}^{-1}$ and $\Lambda_c(^{40}\text{Ar}) = 1.31 \pm 0.01\ \mu\text{s}^{-1}$. These values (like the rates of nuclear capture of μ^- which we obtained in a previous study[3] with the isotopes ^{136}Xe and ^{84}Kr) fall near the minima of the nuclear charge dependence of the reduced capture rate $\Lambda_c Z^4/Z_{\text{eff}}$. [2]

Comparing the values of the μ^- capture rates in the isotopes $\Lambda_c(^{136}\text{Xe}) = 8.6 \pm 0.4\ \mu\text{s}^{-1}$ and $\Lambda_c(^{132}\text{Xe})$ shows that a clear isotopic dependence is observed, though it is weaker than that predicted by the Goulard–Primakoff formula.[13]

In closing, we thank the personnel at the Scientific-Experimental Division of the Synchrocyclotron at the Laboratory of Nuclear Problems at JINR for providing uninterrupted, stable operation of the accelerator, V. B. Brudanin and V. I. Komarov for their interest in the present work and for encouragement, and G. D. Soboleva for assistance in composing this article.

This work was supported by the Russian Fund for Fundamental Research, Project 96-02-17582.

*e-mail: tmamedov@nu.jinr.ru

[1] V. V. Balashov, G. Ya. Korenman, and R. A. Éramzhyan, *Absorption of Mesons by Atomic Nuclei*, Atomizdat, Moscow, 1978.
[2] T. Susuki, D. F. Measday, and J. P. Poalsvig, Phys. Rev. C **35**, 2212 (1987).
[3] T. N. Mamedov, S. G. Barsov, A. L. Getalov *et al.*, JETP Lett. **67**, 318 (1998).
[4] V. A. Bashkirov, V. V. Govorov, Yu. P. Dobretsov *et al.*, JETP Lett. **29**, 271 (1979).

[5] A. Bertin, A. Vitale, and A. Placci, Phys. Rev. A **7**, 2214 (1973).
[6] G. Garboni, G. Gorini, G. Torelly *et al.*, Phys. Lett. **96B**, 206 (1980).
[7] *The Synchrocyclotron and Its Beams at the Laboratory of Nuclear Problems at JINR*, JINR No. 9-92-232 [in Russian], Dubna, 1992.
[8] T. N. Mamedov, V. G. Grebinnik, K. I. Gritsaĭ *et al.*, JINR Report No. R15-96-498 [in Russian], Dubna, 1996.
[9] T. N. Mamedov, V. N. Duginov, D. Gerlakh *et al.*, JETP Lett. **68**, 64 (1998).
[10] J. H. Brewer, Hyperfine Interact. **17–19**, 873 (1984).
[11] Particle Data Group, ''Review of particle properties,'' Phys. Rev. D **50**, 1193 (1994).
[12] R. W. Huff, Ann. Phys. **16**, 288 (1961).
[13] B. Goulard and H. Primakoff, Phys. Rev. C **10**, 2034 (1974).

Translated by M. E. Alferieff

Low-field electrodynamics of polycrystalline ternary molybdenum chalcogenides

S. L. Ginzburg, I. D. Luzyanin, I. R. Metskhvarishvili, É. G. Tarovik, and V. P. Khavronin

St. Petersburg Institute of Nuclear Physics, Russian Academy of Sciences, 188350 Gatchina, Russia

(Submitted 21 December 1998)
Pis'ma Zh. Éksp. Teor. Fiz. **69**, No. 3, 184–188 (10 February 1999)

The penetration of very weak magnetic fields into the polycrystalline low-temperature superconductor $SnMo_6S_8$ is studied experimentally. The experimental results agree satisfactorily with the theory of the critical state in the framework of low-field electrodynamics. It is found that the critical current density in this case does not depend on the dc magnetic field. © *1999 American Institute of Physics.* [S0021-3640(99)00603-9]

PACS numbers: 74.25.Ha, 74.25.Nf

It is well known that magnetic fields lower than the first critical field do not penetrate into a superconductor. However, this assertion becomes incorrect if the superconductor is a multiply connected system, for example, a polycrystal in which the crystallites are intercoupled by Josephson junctions. Since very weak fields can easily penetrate via the Josephson junctions, it can be inferred that such fields will penetrate polycrystalline superconductors. A similar situation occurs in ceramic HTSC materials in which granules are coupled by weak Josephson junctions. In this case a wide range of irreversible and nonlinear phenomena have been observed experimentally and have been explained on the basis of low-field electrodynamics.[1,2] However, as far as we know, low-field electrodynamics has still not been studied for low-temperature polycrystalline superconductors.

The present work is devoted to investigations of the penetration of ultraweak magnetic fields into the polycrystalline superconductor $SnMo_6S_8$ ($T_c \approx 13$ K). This choice was made because molybdenum chalcogenides have a high critical field H_{c2} and correspondingly a very short coherence length $\xi \approx 23$ Å . This makes them similar to HTSCs, in which ξ is of the order of several angstroms. Therefore there are grounds for expecting that for such values of ξ any, even a small, defect can act like a Josephson junction. Our experimental results have shown that, first, very weak magnetic fields of the order of several millioersteds do indeed penetrate into such a superconductor and, second, the experimental data obtained agree with the predictions of low-field electrodynamics.

We recall that the low-field electrodynamics of ceramic HTSCs is based on two assumptions.

1. A ceramic superconductor behaves like a classic type–II superconductor with $\kappa = H_{c2}/H_{c1} \approx 100$. Indeed, the true value of the first critical field $H_{c1} \sim eI/a$ (Ref. 1) is small because of the smallness of the characteristic energy I of a weak link (a is the

granule size) and is approximately 1–10 mOe. Since H_{c1} is small, the true penetration depth λ in such a multiply connected medium will also be large ($\lambda^2 \sim \Phi_0 / H_{c1}\mu_{\text{eff}} \gg a^2$, where $\mu_{\text{eff}} = f_n + f_s\mu_{\text{gr}}$ is the effective magnetic permeability of the ceramic, which takes into account the nonpenetration of the field into the granules). Here f_s is the fraction of the sample that is occupied by the superconducting material, $f_n = 1 - f_s$, and μ_{gr} is the magnetic permeability of the granules, which depends on the size, configuration, and London penetration depth λ_L of the granules. If $\lambda_L \ll a$, then $\mu_{\text{gr}} \ll 1$, and therefore μ_{eff} is also small if $f_n \ll 1$, as is typical for polycrystals.

2. The Bean model of the critical state is applicable to ceramic superconductors.[3] It is well known that the critical state of a superconductor is highly nonequilibrium and is described by a spatially nonuniform magnetic induction $B(r)$. It is determined using the equation of the critical state, which contains, specifically, the magnetic field dependence of the equilibrium induction $B_{eg}(h) \approx \mu_{\text{eff}} h$. Therefore the problem reduces to determining the nonuniform magnetic field $h(r)$ for which the equation of the critical state has the form[3–5]

$$|dh/dx| = 4\pi j_c(h), \tag{1}$$

where $j_c(h) = \alpha(h)/h$. The average induction for an infinite plate of thickness d is

$$\overline{B} = \frac{2}{d}\mu_{\text{eff}} \int_0^{d/2} h(x)dx. \tag{2}$$

In Eq. (1) $\alpha(h)$ is the pinning force and $j_c(h)$ has the meaning of the critical current density and is a phenomenological function of h. This function is an important characteristic, since it can be used for a rough classification of a superconductor.

We note that there exist several models which give different functions $j_c(h)$. An example is the function

$$j_c(h) = \frac{j_0 H_0}{|h| + H_0}$$

obtained experimentally in Ref. 6. Here H_0 is a characteristic field, which is of the order of 3 Oe for the ceramic YBaCuO.

The case $H_0 \to \infty$ leads to the Bean model,[3] where j_c does not depend on the magnetic field. The case $H_0 \to 0$, $j_0 H_0 =$ const corresponds to the Kim–Anderson model,[5] where the pinning force $\alpha(h)$ does not depend on h. Generally speaking, there is no theoretically substantiated choice of the function $j_c(h)$. Therefore there is an obvious need to determine this function experimentally.

In our work we have shown that the behavior of the linear and nonlinear susceptibilities in magnetic fields 10^{-2}–1 Oe can be described well by the theory of the critical state and that $j_c(h)$ does not depend on h. To discuss the experiment, we must make some simple theoretical predictions. As we have said, for $h \gg H_{c1}$ a granular superconductor is a highly nonequilibrium system, which, specifically, exhibits hysteresis. The existence of hysteresis leads to a strong nonlinearity of the field dependence of the susceptibility.

Let a field $h(t) = H + h_0 \cos \omega t$ be applied to such a superconductor. In this case the induction $B(t)$ can be expanded in a Fourier series as

$$B(t)=\frac{1}{2}a_0+\sum_n\ (a_n\cos n\omega t+b_n\sin n\omega t). \tag{3}$$

Performing some calculations similar to those in Ref. 2, we obtain in the adiabatic approximation in the case $h_0\ll H,H_0$ the following expressions for the coefficients a_n and b_n (these quantities were determined in our experiment):

$$\begin{aligned}
&a_0=2\mu_{\text{eff}}H,\quad a_1=\frac{\mu_{\text{eff}}h_0^2}{4\pi j_c(H)d},\\
&a_{2k+1}=0,\quad k\geqslant 1,\\
&b_{2k+1}=-\frac{\mu_{\text{eff}}h_0^2}{8\pi^2 j_c(H)d}\,\frac{1}{(k^2-1/4)(k+3/2)},\\
&a_2=\frac{\mu_{\text{eff}}h_0^3}{32\pi d}\,\frac{d}{dH}\,\frac{1}{j_c(H)},\quad a_{2k}=0,\quad k\geqslant 2,\\
&b_{2k}=-\frac{\mu_{\text{eff}}h_0^3}{16\pi^2 d}\,\frac{d}{dH}\left(\frac{1}{j_c(H)}\right)\frac{k}{(k^2-1/4)(k^2-9/4)}.
\end{aligned} \tag{4}$$

As one can see from these equations, all odd harmonics are proportional to h_0^2 and all even harmonics are proportional to h_0^3, the coefficients differing only in respect to the number of the harmonic. This signifies strong nonlinearity. We note that for $H=0$ the form of the expressions for the odd harmonics in Eq. (4) remains the same, while the even harmonics, naturally, vanish.

We note that for $j_c(H)=$ const there are no even harmonics, even for $H\neq 0$. This situation was realized in our case.

The investigations were performed on a polycrystalline sample of $SnMo_6S_8$ in the form of a disk 9.4 mm in diameter and 3.4 mm thick. The sample was placed in a measuring coil, which also serves for producing an ac magnetic field. The dc field was produced by an external solenoid. The dc and ac fields were parallel to one another and lay in the plane of the disk. The measurements were performed mainly at the frequency 20 kHz and in the interval of fields $10^{-2}\leqslant h_0\leqslant 1$ Oe, $H\leqslant 20$ Oe. We note that in our experiments a_1 and b_1 were determined in terms of the measured values of the real and imaginary parts of the susceptibility (χ' and χ''). It is obvious that $\chi'=-1/4\pi$ in the limit $h\to 0$. Therefore χ' can be represented as $\chi'(h_0)=-1/4\pi+\chi_h'(h_0)$. Then

$$\begin{aligned}
&a_1=(1+4\pi\chi')h_0=4\pi h_0\chi_h'(h_0),\\
&b_1=4\pi h_0\chi''(h_0).
\end{aligned} \tag{5}$$

The method of Ref. 2 was used to study the real and imaginary parts of the linear susceptibility (χ' and χ'') and the moduli of the amplitudes of the higher harmonics $c_n=(a_n^2+b_n^2)^{1/2}$ as functions of the field and temperature.

We now proceed directly to the experimental results. It follows from the temperature dependence of the real part of the linear susceptibility (Fig. 1) that for the experimental sample the transition to the superconducting states starts at $T\approx 13.5$ K, which is typical

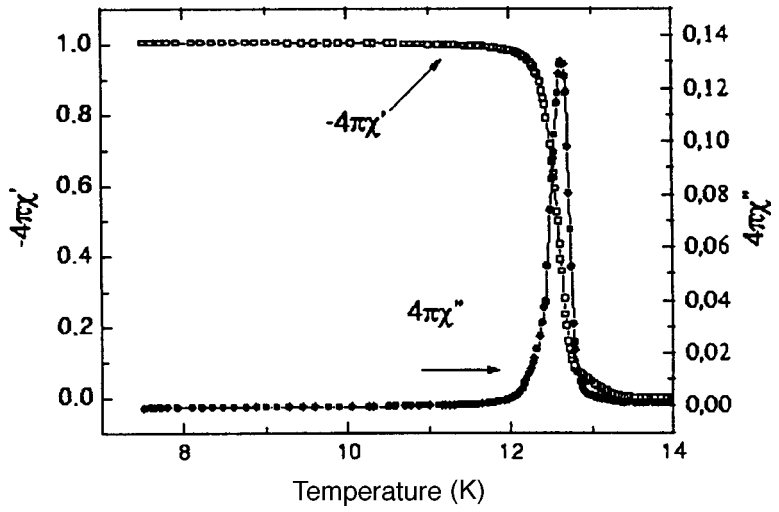

FIG. 1. Fragment of the temperature dependence of the real and imaginary parts of the linear susceptibility. $H=0$, $h_0=1$ Oe.

for compounds in this class (see, for example, Ref. 7). The same figure shows $\chi''(T)$, which at $T\approx 12.5$ K has the characteristic maximum exhibited by superconductors.

One should note first, however, that the polycrystal investigated has pronounced nonlinear properties. It is seen from the spectrum of the high harmonics (Fig. 2), which was obtained at $T<T_c$ in weak ac and dc magnetic fields, that the harmonics decrease weakly as the number of the harmonic increases and that the even harmonics are absent even for $H\neq 0$.

We note that in our experiments the temperature and field behavior of χ' and χ'' (which are directly related with a_1 and b_1) and of the moduli of the amplitudes of the third and fifth harmonics (c_3 and c_5) were studied in detail.

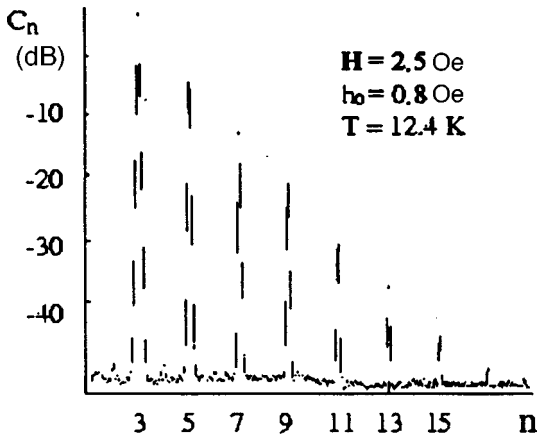

FIG. 2. Spectrum of high harmonics.

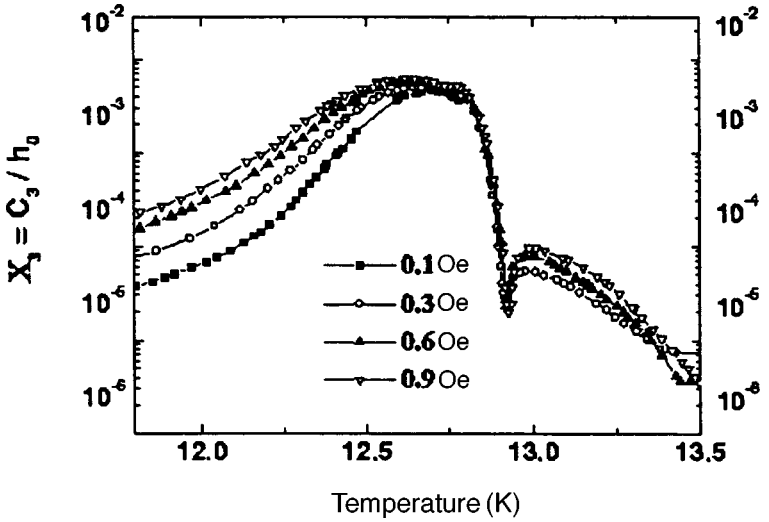

FIG. 3. Fragment of the temperature dependences of the nonlinear susceptibility c_3/h_0 obtained in the absence of a dc magnetic field H for different amplitudes of the ac field.

As an example, the temperature dependence of the susceptibility $\chi_3 = c_3/h_0$ is presented in Fig. 3 for different values of the amplitude h_0 of the ac field. This dependence turned out to be completely similar to that for ceramic HTSCs (see, for example, Ref. 2). A characteristic feature of the dependence presented is the presence of two maxima. The high-temperature maximum could be due to the penetration of the field into the crystallites, while the low-temperature maximum could be due to the penetration only into the Josephson medium formed by weak links between crystallites. The position of this maximum shifts in the direction of low temperatures with increasing h_0. This behavior is due to a transition from a regime where the field penetrated to the center of the sample to a regime where the field penetrated only into a part of the sample. In the latter case, the low-field condition $h_0 \ll H, H_0$ is easily satisfied and therefore, using expression (4), it is easy to check the applicability of the theory of the critical state to the polycrystalline material investigated.

Figure 4 displays a_1, b_1, c_3 and c_5 as functions of h_0 at $H=0$. As one can see from the figure, these quantities clearly show a quadratic dependence on h_0, which is characteristic for the critical state.

The equation (4) contains the two independent quantities μ_{eff} and j_0, which were not determined independently in our experiments. For this reason, to compare the theoretical and experimental results, it is reasonable to consider the ratios a_1/b_1, b_1/c_3, and so on, which, according to Eq. (4), should not depend on μ_{eff} and j_0. As it turned out, the experimentally determined ratios agree with the theoretical prediction to within 10–20%.

The investigations performed in dc fields showed that even in this case a quadratic dependence of the amplitudes of the odd harmonics on the amplitude of the ac field is observed, and there are no even harmonics. At the same time, it was found that the amplitudes of the odd harmonics do not depend on the magnitude of the dc field, at least

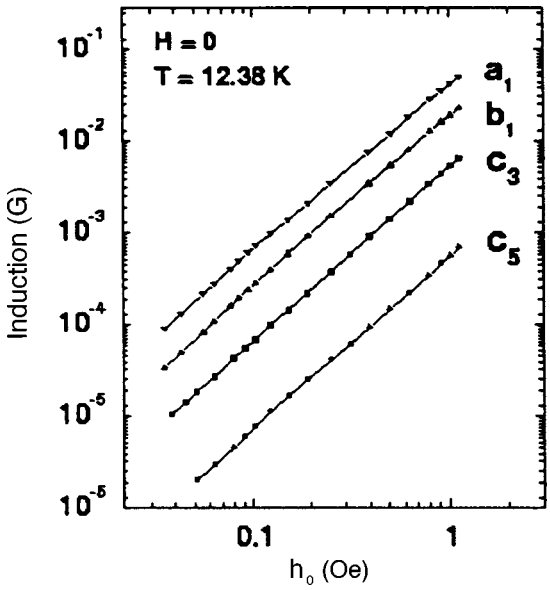

FIG. 4. a_1, b_1, c_3, and c_5 versus h_0 at $H=0$.

up to 20 Oe. This signifies that $j_c(H)$ does not depend on the magnetic field, i.e., $j_c(H)=j_0$.

In summary, the results of our experiments show that the critical state is indeed realized in polycrystalline low-temperature molybdenum chalcogenides in the low-field range. Therefore the basic ideas of low-field electrodynamics are applicable to such superconductors.

We thank A. V. Mitin for helpful discussions of the results of this work and for providing the sample and O. V. Gerashchenko for helpful discussions during the course of the experiment.

This work was supported by the Scientific Council on subprogram ''Superconductivity'' in the program ''Topical Problems in Condensed-Matter Physics'' and was performed as part of Project No. 96021 ''Profil'.'' This work was also supported by the subprogram ''Statistical Physics'' of the State Science and Technology Program ''Physics of Quantum and Wave Processes'' (Project VIII–3).

[1] J. R. Clem, Physica C **153-155**, 50 (1988).
[2] S. L. Ginzburg, V. P. Khavronin, G. Yu. Logvinova *et al.*, Physica C **174**, 109 (1991).
[3] C. P. Bean, Rev. Mod. Phys. **36**, 31 (1964).
[4] Y. B. Kim, C. F. Hempstead, and A. R. Strand, Phys. Rev. **131**, 2486 (1963).
[5] P. W. Anderson and Y. B. Kim, Rev. Mod. Phys. **36**, 39 (1964).
[6] I. D. Luzyanin, S. L. Ginzburg, V. P. Khavronin, and G. Yu. Logvinova, Phys. Lett. A **141**, 85 (1989).
[7] N. E. Alekseevskiĭ, A. V. Mitin, and E. P. Khlybov, Zh. Éksp. Teor. Fiz. **82**, 927 (1982) [Sov. Phys. JETP **55**, 543 (1982)].

Translated by M. E. Alferieff

Anisotropic negative magnetoresistance in one-dimensional channels of porous silicon

A. I. Yakimov* and A. V. Dvurechenskiĭ
Institute of Semiconductor Physics, Siberian Branch of the Russian Academy of Sciences, 630090 Novosibirsk, Russia

(Submitted 23 December 1998)
Pis'ma Zh. Éksp. Teor. Fiz. **69**, No. 3, 189–193 (10 February 1999)

It is found that the magnetoresistance of manganese-doped porous amorphous silicon in fields 0–5 T is negative and depends on the orientation of the magnetic field. The experimental curves of the magnetic-field dependence are described well by the theory of quantum corrections to the conductivity in the one-dimensional case. The phase coherence length in the material is ≈ 25 nm at $T=4.2$ K. © *1999 American Institute of Physics.* [S0021-3640(99)00703-3]

PACS numbers: 72.20.My, 72.80.Cw

The theory of quantum corrections to the conductivity of thin one-dimensional wires was formulated in the mid-1980s (see review[1]). However, to this day not all of the basic assumptions have been checked experimentally in detail. One such problem is the behavior of the resistance in a magnetic field. It is well known that the effect of a magnetic field on the interference correction to the conductivity of disordered metals and degenerate semiconductors leads to a negative magnetoresistance (NMR) in classically weak fields.[2–4] In the three-dimensional case the NMR is isotropic and depends on the magnetic field as B^2 in weak fields ($L_f \ll L_B$, where L_f is the phase coherence length, $L_B \equiv \sqrt{\hbar/2eB}$ is the magnetic length) and is proportional to $\sqrt{B}$ in the high-field limit. In two-dimensional (2D) films the correction to the conductivity varies as $\ln B$, and the magnetoresistance depends strongly on the orientation of the field relative to the film plane. Anisotropy of the NMR in a 2D system is a well-established experimental fact[1] and is due to the difference between the orbital motion of the electrons in a plane and in a thin channel. Al'tshuler and Aronov substantiated the existence of an anisotropic NMR in one-dimensional wires also.[5] However, an adequate experimental check of this assumption is difficult. The problem is that, as a rule, a 1D electron gas is formed by means of a geometric ''cutoff'' of a 2D system.[6–9] In such structures the width of a channel is always much greater than its thickness and, by analogy with 2D films, this can contribute an additional element of anisotropy in the observed magnetoresistance. An experimental arrangement where the channel dimensions are the same in the transverse direction should be more acceptable.

We showed in a previous work that, as a result of electrochemical etching of amorphous silicon (a-Si) in a solution of hydrofluoric acid, under certain conditions conducting regions of silicon, surrounded by depleted regions and pores, form in the material;

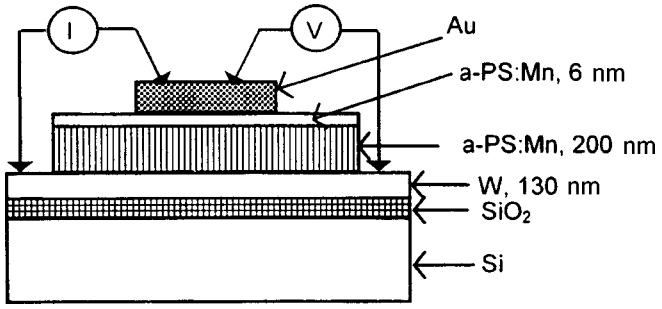

FIG. 1. Diagram of the experimental structure and measurements.

these regions are 5–8 nm in diameter and are extended perpendicular to the surface.[10] These conducting channels are weakly linked with one another and form a system of one-dimensional silicon filaments whose cross section is, on average, isotropic. A study of charge transfer on the insulator side of the Anderson transition showed that the conductivity in porous a-Si doped with manganese (a-PS:Mn) to $c=4$ and 7 at.% is governed by electron hops along quasi-one-dimensional trajectories bounded by the walls of the pores.[10] The average diameter of the conducting channels determined from the conductivity data was 6 nm. As the Mn concentration increases above 14 at.% the conductivity becomes ''metallic,'' and for $c \geqslant 18$ at.% the temperature dependence is described well by the interference correction in the one-dimensional case.[11] In the present work we investigated the effect of a magnetic field on the resistance of a-PS:Mn for two orientations of the field: along ($B_{\parallel}$) and perpendicular ($B_{\perp}$) to the silicon channels. The field was directed perpendicular to the sample surface in the first case and in the plane of the surface in the second case. As a result, we found anisotropy of the NMR, the change in resistance in the field being in good agreement with the theory of the NMR of a one-dimensional conductor.

It is very important to note one other advantage of the object chosen for investigating the quasiclassical diffusion regime of quantum wires. As the transverse dimensions of quasi-one-dimensional conductors produced by conventional methods on the basis of crystalline materials decreases, two factors which interfere with the check of the corresponding theory are encountered. First, if the mean free path becomes of the order of the diameter of the wire, then scattering by the boundaries is substantial and leads to a positive magnetoresistance.[7] Second, if the wire diameter equals the electron wavelength, then size-quantization effects start to affect the transport properties.[9] Our object of investigation does not have these drawbacks, since, in the first place, the mean free path in amorphous materials is very short (of the order of several interatomic distances) as a result of topological disorder and, in the second place, the high (up to 10^{22} cm^{-3}) solubility of transition-metal impurities (Mn, Fe) in amorphous silicon makes it possible to obtain an electron gas with a short (~ 1 nm) de Broglie wavelength. In this connection, size-quantization and boundary-scattering effects are not manifested even in ultrathin (~ 10 nm) amorphous wires.

The cross section of the structure is displayed in Fig. 1. A tungsten film (bottom) and a gold film (top) served as electrical contacts. The area of the top Au electrode was 5×10^{-3} cm^2. The porous layer consisted of two parts: a thin (~ 6 nm) contact layer at

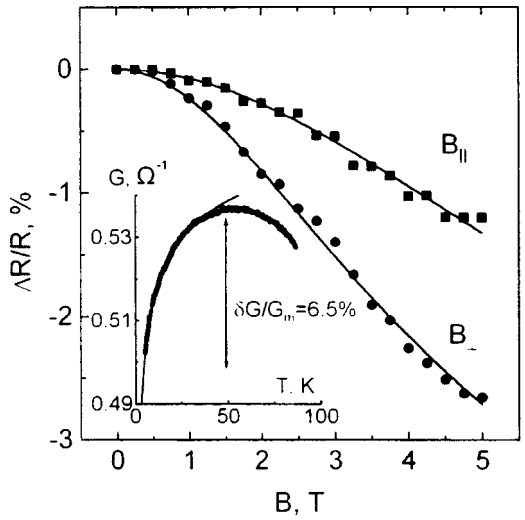

FIG. 2. Magnetoresistance of a porous layer of amorphous silicon doped with manganese to 22 at.%. The measurement temperature is 4.2 K. The $B_{\|}$ curve corresponds to magnetic field orientation parallel to the one-dimensional silicon channels (perpendicular to the sample surface) and the $B_{\perp}$ curve describes the magnetoresistance in the transverse geometry (field parallel to the sample surface and perpendicular to the channels). The solid lines were obtained by fitting expressions (1) and (2) to the experimental data. Inset: Temperature dependence of the conductivity of the same structure in zero field.

the top, with about 30% porosity, and an approximately 200-nm-thick main layer at the bottom, with 50–60% porosity. A detailed description of the structures and the method used to prepare them is given in Ref. 11. The conductivity was measured by the four-probe method using ac current. The current was 0.1 μA and the frequency was 1 kHz. The magnetoresistance was measured at $T=4.2$ K in fields up to 5 T.

The temperature dependence of the conductivity of a sample with 22 at.% Mn is shown in the inset in Fig. 2. At temperatures $T>50$ K the conductivity increases with decreasing temperature. This corresponds to the classical metallic behavior under conditions of scattering by phonons. At low temperatures the localization correction becomes substantial and the conductivity starts to decrease. In a previous work we showed that this correction depends on temperature as $\Delta G \propto T^{-1/3}$ (solid curve in the inset in Fig. 2). According to theoretical calculations,[12] electron–electron collisions with small energy transfer lead to such a law in one-dimensional systems. The phase coherence length can be estimated as[13] $L_f \approx b(\delta G/G_m)(k_F b)(k_F l)$, where b is the average diameter of the 1D conducting channels, k_F is the wave vector at the Fermi surface, l is the mean free path, and $\delta G/G_m$ is the relative change in the conductivity as a result of the interference correction. Near the Anderson transition it can be assumed that $k_F l \approx 1$. Then for $\delta G/G_m=6.5\%$ (see Fig. 2) and $b=6$ nm we obtain $L_f=21$ nm.

The magnetoresistance of the same sample at $T=4.2$ K and for two different field orientations is displayed in Fig. 2. In fields 0–5 T the magnetoresistance is negative and strongly anisotropic. The curves $\Delta R(B)/R$ cannot be described by a logarithmic law, characteristic for quantum corrections in 2D systems (otherwise, the curves would bend in the other direction). In addition, the presence of strong anisotropy argues against a

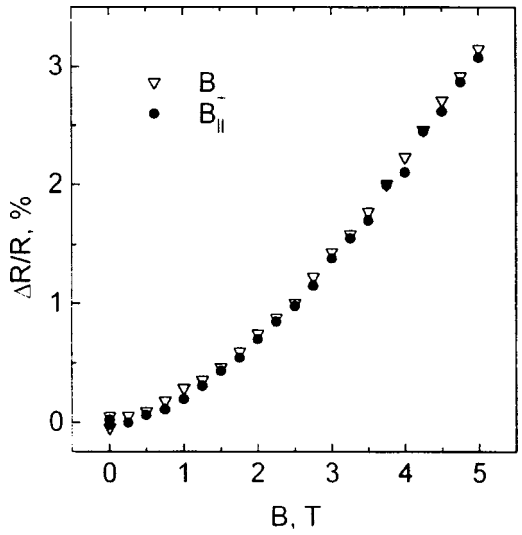

FIG. 3. Magnetoresistance of a compact layer of amorphous silicon doped with manganese to 22 at.% for two field orientations: perpendicular to and parallel to the surface of the sample. The measurement temperature is 4.2 K.

three-dimensional mechanism of magnetoresistance. Nonetheless, to verify this we measured the magnetoresistance of continuous (nonporous) a-$Si_{1-c}Mn_c$ layers with the same manganese concentration (Fig. 3). One can see that the behavior of the magnetoresistance in porous layers is strongly different from that in compact layers. The magnetoresistance of three-dimensional samples does not depend on the field orientation and is positive. Ordinarily, isotropic positive magnetoresistance is attributed to the suppression of the interaction of electrons with antiparallel spins, in which case the Zeeman splitting of the levels becomes equal to the thermal energy kT.

According to theory,[5] the relative change in the resistance R of a one-dimensional conductor in a magnetic field is given by the expressions

$$\frac{\Delta R}{R} = -R\frac{e^2}{\pi\hbar}\frac{L_f}{L}\left\{\left(1+\frac{b^2L_f^2}{32L_B^4}\right)^{-1/2}-1\right\} \tag{1}$$

for the field oriented parallel to the axis of the wire and

$$\frac{\Delta R}{R} = -R\frac{e^2}{\pi\hbar}\frac{L_f}{L}\left\{\left(1+\frac{b^2L_f^2}{12L_B^4}\right)^{-1/2}-1\right\} \tag{2}$$

if the field is oriented perpendicular to the axis of the wire. Here L is the length of the wire. The difference between expressions (1) and (2) lies in the numerical factors in the parentheses. This factor carries information about the relative orientation of the wire axis and the field. For the perturbation theory used to derive expressions (1) and (2) to be applicable, the inequality $b<L_B$ must be satisfied.[5] Otherwise, the sample should behave as a three-dimensional sample. Since $L_B>13$ nm For $B<5$ T, the above-indicated condition is indeed satisfied in our experiment. Expression (1) and (2) were obtained for an

isolated filament. In our case a large number of wires are connected in parallel and this, at first glance, precludes a direct application of Eqs. (1) and (2) for analyzing the experimental curves. We note, however, that the parameter combination $e^2L_f/\pi\hbar L$ is simply the quantum correction to the conductivity of a 1D system as a result of interference. For this reason, assuming that all channels in a-PS:Mn are independent, we can set $R(e^2L_f/\pi\hbar L)\approx\delta G/G_m$.

The results of fitting expressions (1) and (2) to the experimental data for $b=6$ nm and $\delta G/G_m=0.065$ are shown in Fig. 2 (solid lines). The coherence length L_f served as the adjustable parameter in both cases. One can see that the theory of the NMR of one-dimensional wires describes well the interference quantum correction to the conductivity of a-PS:Mn in a magnetic field with different orientations. The fit gives $L_f=25\pm2$ nm for $B_\perp$ orientation and $L_f=23\pm3$ nm in the case of a field oriented parallel to the axis of the channels. These values agree well both with each other and with the analysis of the temperature dependence of the conductivity. In addition, the values obtained for L_f do indeed satisfy the criterion for the interference correction to be of a one-dimensional character: $L_f>b$.

In conclusion, we wish to note that the observation of anisotropic magnetoresistance, which can be described by the same quantity L_f for various field orientations, is possible only if the length of the projection of the channel on the direction of the field $B_\perp$ is much shorter than the length of the projection on the direction $B_\parallel$ (the channels are highly extended perpendicular to the surface of the structure). Otherwise, fitting the theoretical expressions (1) and (2) to the experimental magnetic field dependences would give different values for the phase coherence length.

We thank A. I. Nikiforov and V. A. Dravin for assisting in the preparation of the samples. This work was supported by the Russian Fund for Fundamental Research (Grant No. 97-02-18507).

*e-mail: yakimov@isp.nsc.ru

[1] P. A. Lee and T. V. Ramakrishnan, Rev. Mod. Phys. **57**, 287 (1985).
[2] B. L. Altshuler, D. E. Khmel'nitzkii, A. I. Larkin, and P. A. Lee, Phys. Rev. B **22**, 5142 (1980).
[3] A. Kawabata, Solid State Commun. **34**, 431 (1980).
[4] B. A. Al'tshuler, A. G. Aronov, A. I. Larkin, and D. E. Khmel'nitskiĭ, Zh. Éksp. Teor. Fiz. **81**, 768 (1981) [Sov. Phys. JETP **54**, 410 (1981)].
[5] B. A. Al'tshuler and A. G. Aronov, JETP Lett. **33**, 499 (1981).
[6] P. Santhanam, S. Wind, and D. E. Prober, Phys. Rev. Lett. **53**, 1179 (1984).
[7] K. K. Choi, D. C. Tsui, and S. C. Palmateer, Phys. Rev. B **33**, 8216 (1986).
[8] K. K. Choi, D. C. Tsui, and K. Alavi, Phys. Rev. B **36**, 7751 (1987).
[9] Z. D. Kvon, M. M. Voronin, Kijoon Kim, and Hu Jong Lee, JETP Lett. **67**, 1029 (1998).
[10] A. I. Yakimov, A. V. Dvurechenskii, N. P. Stepina *et al.*, J. Phys.: Condens. Matter **9**, 889 (1997).
[11] A. I. Yakimov, A. V. Dvurechenskiĭ, V. A. Dravin, and Yu. Yu. Proskuryakov, JETP Lett. **67**, 284 (1998).
[12] B. L. Altshuler, A. G. Aronov, and D. E. Khmelnitsky, J. Phys. C **15**, 7367 (1982).
[13] A. A. Abrikosov, *Fundamentals of the Theory of Metals*, North-Holland, Amsterdam, 1988 [Russian original, Nauka, Moscow, 1987].

Translated by M. E. Alferieff

Interference ionization of an impurity by an electric field in a system of quantum wells

Yu. A. Aleshchenko,* I. P. Kazakov, V. V. Kapaev, Yu. V. Kopaev, N. V. Kornyakov, and A. E. Tyurin

P. N. Lebedev Physics Institute, Russian Academy of Sciences, 117924 Moscow, Russia

(Submitted 29 December 1998)
Pis'ma Zh. Éksp. Teor. Fiz. **69**, No. 3, 194–199 (10 February 1999)

A radical change in the ionization energy of the donor impurity Si in a GaAs/AlGaAs double-well heterostructure is observed experimentally when the electronic wave function is relocated in an electric field. The ionization energy of the impurity decreases from 15.5 meV to 0 when the voltage across the structure changes by less than 1 V. The Stark effect would give a change in the ionization energy of not more than 3 meV. © *1999 American Institute of Physics.*
[S0021-3640(99)00803-8]

PACS numbers: 73.20.Dx, 73.20.Hb

Quantum interference of the electronic states of coupled quantum wells (QWs) makes such a system very sensitive to external perturbations. Under these conditions even a comparatively weak external electric field applied parallel to the growth axis of the structure is sufficient to change radically the form of the electronic wave functions (WFs) and to relocate them from one QW into the other. This is reflected in most of the physical characteristics of the system. In Ref. 1 it was predicted that the impurity ionization energy E_{imp} should change upon a relocation of the electronic WF in a system of QWs. This effect is due to the inversion of the bottom size-quantization energy subbands of tunneling-coupled QWs when the subbands undergo anticrossing in an external electric field. As a result of the inversion, the binding energy and the form of the WF of a localized electronic state, formed mainly from the states of the lower subband, on an impurity atom change. In the present letter a direct experimental confirmation of the interference ionization of a donor impurity accompanying relocation in the GaAs/AlGaAs double-well structure is reported.

The experimental structure was grown on a GaAs(100) substrate with a 1 μm thick GaAs buffer layer by molecular-beam epitaxy. The active region of the structure, confined between undoped $Al_{0.34}Ga_{0.66}As$ spacers, each 200 Å thick, included an undoped 57 Å wide QW at the bottom, a 34 Å thick $Al_{0.34}Ga_{0.66}As$ barrier layer, and a 79 Å wide QW at the top containing a Si delta layer ($n=6.3\times10^{11}$ cm^{-2}) at the center. A Si-doped n^+-$Al_{0.34}Ga_{0.66}As$ ($\approx7\times10^{17}$ cm^{-3}) layer and a Si-doped n^+-GaAs (1×10^{18} cm^{-3}) protective layer, 200 and 100 Å thick, respectively, were grown on the top spacer. The top and bottom electrodes were formed by depositing a half-transmitting Ni film through a mask followed by etching of the structure around the film to the n^+-GaAs buffer layer.

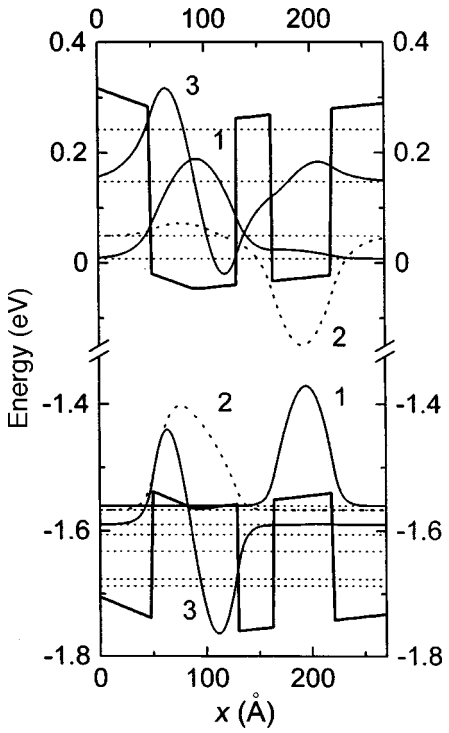

FIG. 1. Profile of the potential in the region of the QW of the experimental structure and the energy subbands as well as the computed WFs for the lower electron and heavy-hole subbands with a zero applied voltage. The numbers on the curves are the subband numbers. The energy scale of the valence band is magnified so that the details can be distinguished more clearly.

The parameters of the structure were chosen so as to provide, following Ref. 1, the most favorable conditions for electronic relocation in an external electric field from the doped QW closest to the surface into the more distant and narrower undoped QW.

The photoluminescence (PL) spectra in the temperature interval 20–90 K were excited by 4880 Å radiation from an Ar^+ laser and were analyzed with a DFS-24 double monochromator and detected with an FÉU-79 photomultiplier in the photon-counting mode.

Several factors complicate the measurement of E_{imp} in systems of QWs: the complexity of the PL spectrum of multiwell structures, the dominant role of the excitonic PL over the weak peaks due to interband transitions (relative to which E_{imp} must be measured), and the field dependence of most radiative transitions. In this connection, the PL peaks of the experimental structure were identified by comparing the experimental spectra measured at different temperatures using different intensities of the exciting radiation with the results of a theoretical calculation based on a solution of the Schrödinger and Poisson equations.

The potential profile of the QWs of the experimental structure and also the WFs for the bottom subbands of the energy spectrum of the electrons and heavy holes at zero applied voltage ($U=0$) are presented in Fig. 1. As one can see from Fig. 1, the distortion

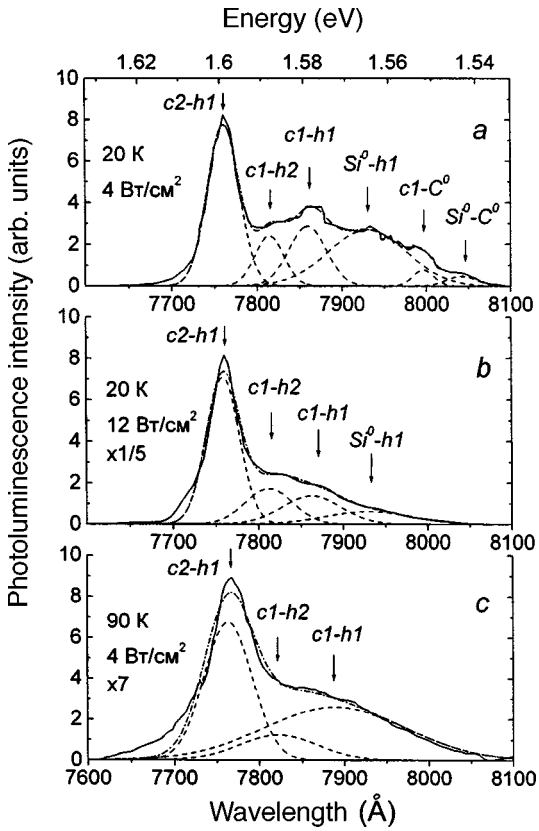

FIG. 2. Photoluminescence spectrum of a GaAs/AlGaAs double-well structure with no external field at 20 K and power density 4 W/cm^2 of the exciting radiation on the sample (a) and transformation of the spectrum with increasing power density of the exciting radiation (12 W/cm^2) (b) and with increasing temperature (90 K) (c). The dashed lines show the Gaussian contours used to approximate the spectra; the dot-and-dash line shows the resulting contours.

of the potential relief by the built-in field has the effect that the WFs of the electrons and holes in the ground state (curves *1*) are localized in different QWs. As a result, the overlap integral for transitions between the first size-quantization subbands of the electrons and heavy holes ($c1-h1$) is much smaller than for transitions between the second electronic subband and the first heavy-hole subband ($c2-h1$) as well as the first electronic subband and the second heavy-hole subband ($c1-h2$), for which the WFs are localized in one of the QWs.

The PL spectrum of the above-described structure, measured at $U=0$, temperature 20 K, and power density 4 W/cm^2 on the sample, is displayed in Fig. 2a (solid line). A narrow peak with a maximum at 1.599 eV, which adjoins on the low-energy side a wide band containing contributions from several overlapping peaks, dominates the spectrum. The decomposition of the spectrum into components gives six Gaussian contours (shown in the figure by dashed lines; the dot-and-dash line shows the total contour). One can see

from the figure that an approximation using six Gaussians reproduces the measured spectrum well.

Comparing the experimental data with the theoretical calculation shows that the peaks near 1.599, 1.588, and 1.576 eV are due to the excitonic transitions $c2-h1$, $c1-h2$, and $c1-h1$, respectively. The high intensity of the peaks that correspond to the transitions $c2-h1$ and $c1-h2$ is correlated with the computed WFs presented in Fig. 1. A similar anomalous ratio of the intensities of the transitions $c2-h1$, $c1-h2$, and $c1-h1$ was previously observed in the PL spectra of delta-doped isolated AlGaAs/InGaAs/GaAs QWs at room temperature[2] and was explained by a strong asymmetry of the potential relief.

The peaks with maxima at 1.566, 1.552, and 1.543 eV correspond to transitions with energies less than the energy of the excitonic transition $c1-h1$ (1.576 eV). Therefore they are more likely to be associated with impurities. In the temperature range 20–90 K all electron–impurity complexes with more than two particles should be ionized. Specifically, exciton complexes which are bound with neutral impurities and make the largest contribution to the impurity PL at low temperatures[3] are subject to thermal dissociation. In consequence, the peak at 1.566 eV, closest to the excitonic transition $c1-h1$ (1.576 eV), is most likely due to electronic transitions from neutral Si impurity atoms to the bottom heavy-hole subband (Si^0-h1).

The peak at 1.552 eV, lying next to the Si^0-h1 (1.566 eV) transition, is split from the peak $c1-h1$ (1.576 eV) by 24 meV. A peak was also observed in the PL spectra of a 70 Å wide GaAs QW at 20 K. In this case the peak was located 26 meV lower in energy than the peak due to the excitonic transition $c1-h1$ (Ref. 4). This peak was due to the residual acceptor carbon impurity C in a neutral charge state ($c1-C^0$). Since the main background acceptor in our samples is also C, it is natural to associate the peak at 1.552 eV to the transition $c1-C^0$. The remaining peak at 1.543 eV is the weakest peak in the spectrum, and in addition it is close in energy to the peak $c1-C^0$, so that its position is determined least accurately. However, since its energy splitting from the peak $c1-C^0$ is close to that of the peak Si^0-h1 relative to the peak $c1-h1$, the peak at 1.543 eV can be attributed to a transition between the ground states of neutral Si donors and C acceptors, i.e., Si^0-C^0.

To confirm the impurity nature of the peaks at low energies, measurements were performed of the dependence of the PL spectra on the intensity of the exciting radiation and on the temperature. As the power density of the exciting radiation increases, rapid saturation of the intensity of the peaks is observed at low energies in connection with the finite number of Si donors and C acceptors in the QWs. As an example, Fig, 2b displays the PL spectrum of the structure measured with a power density of the exciting radiation 12 W/cm^2 and five times weaker amplification than in the spectrum in Fig. 2a. Indeed, as the power of the exciting radiation increases, the contribution of the peaks on the low-energy side decreases compared with the contribution of the transition $c1-h1$. This confirms that these peaks are due to impurities. At the same time the intensities of the narrow peaks that we attributed to the transition $c2-h1$ and of the peak due to the transition $c1-h2$ increase rapidly. This is due to the small equilibrium population of the subbands $c2$ and $h2$ and, accordingly, to the possibility that this population changes sharply even under weak excitation. We note that because of the low intensity of the peaks in the spectrum at low energies in Fig. 2b, a good approximation in this region is

obtained by taking account of one peak, which we associate to the transition Si^0-h1, instead of three peaks, as in Fig. 2a.

As the temperature increases, the PL spectra become weaker. This is due to an increase in the probability of thermal transfer of carriers out of a well into the barrier layers, the intensity of the spectrum on the low-energy side decreasing more rapidly. The spectrum in Fig. 2c illustrates the transformation of the PL spectra with increasing temperature. This spectrum measured at 90 K with seven times greater amplification than the spectrum in Fig. 2a. The good fit of the spectrum by three contours (dashed lines) attests to the fact that at 90 K only the peaks due to the transitions $c2-h1$, $c1-h2$, and $c1-h1$ contribute to the spectrum. The observed effect is typical for the PL spectra of impurity states and is explained by the thermal ionization of donors and acceptors. Of all the impurity peaks, in what follows we shall be interested only in the peak due to the transition Si^0-h1, since for all other peaks associated with the background acceptor impurity C uniformly distributed in the QWs and in the barrier layers there should be no change in the ionization energy of the impurity upon relocation.

In the spectrum in Fig. 2a, measured with $U=0$, the impurity peak Si^0-h1 (1.566 eV) is split from the peak due to the excitonic transition $c1-h1$ (1.576 eV) by 10 meV. To determine E_{imp} the exciton binding energy E_{ex} must be added to this value. Our variational calculations taking account of the built-in field in the structure give $E_{ex}\approx 6$ meV. Then E_{imp} is close to 16 meV. This is greater than the known values of the ionization energy 12–13 meV obtained by different authors (see Refs. 5 and 6) for Si impurity at the center of an approximately 100 Å wide QW. In our case delta doping results in the appearance of a V-shaped potential at the center of the QW. This potential lowers the energy of the lowest levels with respect to the energy of the higher-lying states[7] and, correspondingly, increases E_{imp}. According to our calculations, for 6.3×10^{11} cm^{-2} delta doping the energy E_{imp} reaches 3–4 meV. In this case the position of the PL peak, 1.566 eV, agrees quite well with the theoretical calculations for the Si^0-h1 transition energy.

An external electric field shifts the PL peaks. Figure 3 shows the experimental data as well as the results of a theoretical calculation of the positions of the PL peaks as a function of the intensity of the electric field arising when a voltage from $+0.4$ to -2.4 V is applied to the half-transmitting electrode at the top. One can see that the peaks of the indirect transitions $c2-h1$ and $c1-h2$ rapidly shift with increasing field, since the electronic and hole subbands associated with these transitions belong to different QWs and they move in opposite directions as the field increases. At the same time, for less than 25 kV/cm fields, the position of the excitonic peak $c1-h1$ does not depend on the magnitude of the field, since the quadratic Stark effect is negligible for direct transitions. This behavior of the PL peaks in an external field for the transitions considered confirms our interpretation of these peaks.

For us, the anticrossing of the spectral lines $c1-h1$ and $c2-h1$ in Fig. 3 at a field intensity of about 30 kV/cm is most fundamental, since in this case relocation of the WFs of the lower subband from the doped into the undoped QW occurs. The field dependence of the energy of the peak Si^0-h1 near the relocation point can be explained on the basis of the ideas of Ref. 1. In the effective mass approximation $E_{\text{imp}}(F)=u^2(F)E_0$, where E_0 is the impurity ionization energy in an individual QW with the same parameters as the doped QW in the experimental structure. The coefficient $u(F)$, which depends on the

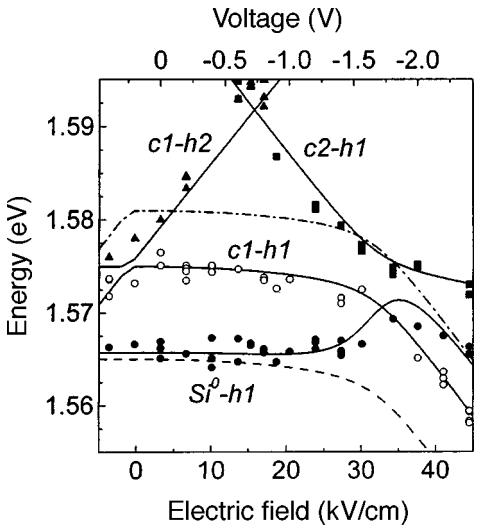

FIG. 3. Theoretical (solid lines) and experimental field dependences of the energies of the excitonic transitions $c1-h1$, $c1-h2$, and $c2-h1$ and the energy of the transition Si^0-h1 between an impurity level and the heavy-hole band. The dashed line shows the computed electric-field dependence of the energy of the impurity transition Si^0-h1 in the absence of a change in the impurity ionization energy. The experimental points obtained for several samples with excitation through the half-transmitting electrode are presented.

external electric field F, contains information about the part of the electronic wave function that is localized in the doped QW. When the WF is relocated into the undoped QW, this coefficient changes from 1 to 0 and E_{imp} decreases from E_0 to 0. A more detailed calculation in the approximation of a delta impurity potential makes it possible to refine the preceding formula and to obtain the expression

$$E_{\text{imp}}(F)=\pi^2 r\left[\exp\left(\frac{4\pi r}{ag|\psi(x_0,F)|^2}\right)-1\right]^{-1}, \quad r=\frac{\hbar^2}{2ma},$$

where m is the electron effective mass, a is the lattice parameter, g is the interaction constant of the electron with the impurity potential, $\psi(x,F)$ is the envelope of the WF for an electron in the bottom size-quantization subband, and x_0 is the coordinate of the impurity atom along the growth axis of the structure. The factor $|\psi(x_0,F)|^2$, which depends on the position of the impurity in the QW and on the field, leads to the strong field dependence of E_{imp}.

The solid line in Fig. 3 shows the field dependence, calculated in this manner, of the position of the peak Si^0-h1 of the impurity PL. For comparison, the field dependences of the position of the impurity peak in the absence of a change in ionization energy of the impurity (dashed line) and the corresponding dependence for the transition $c1-h1$ of free electrons and holes (dot-and-dash curve) are also shown there. The latter was obtained from the experimental field dependence of the energy of the excitonic transition $c1-h1$ with allowance for the theoretically computed binding energy of the $c1-h1$ exciton. As one can see from Fig. 3, in the field range 25–40 kV/cm, where relocation of the elec-

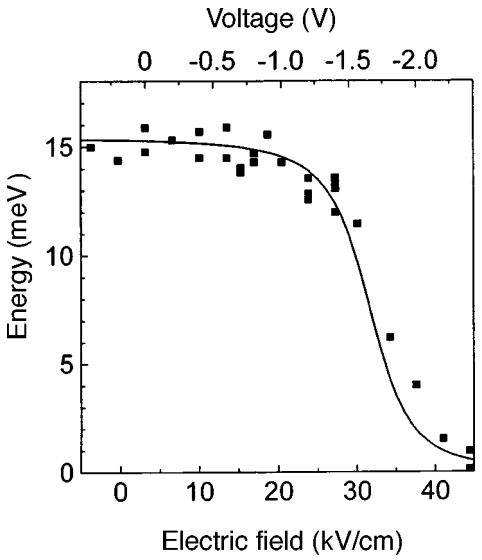

FIG. 4. Theoretical (solid line) and experimental (dots) curves of the ionization energy of a Si impurity in a QW as functions of the external electric field. The experimental data for several samples are presented.

tronic WFs from the wide QW into the narrow QW, located farther from the surface, occurs, the Si^0-h1 curve rapidly approaches the curve for the transition $c1-h1$ of free electrons and holes. This attests to a sharp decrease in $E_{\rm imp}$.

The theoretical and experimental electric-field dependences of $E_{\rm imp}$, which were obtained as the difference between the computed energy dependence of the transition $c1-h1$ of free electrons and holes and the theoretical and experimental dependences for the transition Si^0-h1, are presented in Fig. 4. As one can see from the figure, $I_{\rm imp}$ reaches 15.5 meV in a weak field and drops to zero as the field increases. This sharp change in $E_{\rm imp}$ is due to the relocation of the electronic WFs accompanying anticrossing of the lower subbands in an electric field and cannot be explained by the Stark effect, which we estimate to be no greater than 3 meV.

In summary, in the present letter the existence of a previously predicted sharp change in the impurity ionization energy accompanying relocation of the electronic WF in the system of QWs in an external electric field was confirmed experimentally.

We thank V. I. Tsekhosh for growing the structures and S. S. Shmelev for lithography and for preparing the contacts. This work was supported by the Russian Fund for Fundamental Research, the Russian Interdisciplinary Science and Technology Program ''Physics of Solid-State Nanostructures'' and the Federal Target Program ''Integratsiya.''

*e-mail: yuriale@sci.lebedev.ru

[1] V. I. Belyavskiĭ, Yu. V. Kopaev, N. V. Kornyakov, and S. V. Shevtsov, JETP Lett. **61**, 1039 (1995).
[2] W. Lu, G.-I. Ng, B. Jogai *et al.*, J. Appl. Phys. **82**, 1345 (1997).
[3] D. C. Reynolds, C. E. Leak, K. K. Bajaj *et al.*, Phys. Rev. B **40**, 6210 (1989).
[4] J. P. van der Ziel, X. Tang, and R. Johnson, Appl. Phys. Lett. **71**, 791 (1997).

[5] P. O. Holtz, B. Monemar, M. Sundaram *et al.*, Phys. Rev. B **47**, 10596 (1993).
[6] Z. H. Huang, S. D. Liang, C. Y. Chen, and D. L. Lin, J. Phys.: Condens. Matter **10**, 1985 (1998).
[7] R. Sasagawa, H. Sugawara, Y. Ohno *et al.*, Appl. Phys. Lett. **72**, 719 (1998).

Translated by M. E. Alferieff

Observation of fractional harmonics in the NMR signal from superfluid ^{3}He-B

V. V. Dmitriev, I. V. Kosarev, and D. V. Ponarin
P. L. Kapitsa Institute of Physics Problems, Russian Academy of Sciences, 117334 Moscow, Russia

(Submitted 29 December 1998)
Pis'ma Zh. Éksp. Teor. Fiz. **69**, No. 3, 200–205 (10 February 1999)

Unusual spin-precession states of ^{3}He-B in which the magnetization is half the equilibrium value are investigated by continuous-wave NMR methods. Signals at frequencies equal to 1/2 and 3/2 of the magnetization precession frequency are observed in two such states. Such signals exist because the order parameter of superfluid ^{3}He in these states precesses with frequency equal to half the magnetization precession frequency. © *1999 American Institute of Physics.*
[S0021-3640(99)01003-8]

PACS numbers: 67.57.Lm, 76.60.Es

The spin dynamics of superfluid ^{3}He is determined by the Leggett equations describing the motion of the magnetization $\mathbf{M}$ and order parameter:[1]

$$\dot{\mathbf{M}} = g\mathbf{M}\times\mathbf{H} + \mathbf{R}_D, \tag{1}$$

$$\dot{\mathbf{d}} = \mathbf{d}\times g(\mathbf{H} - \mathbf{M}/\chi), \tag{2}$$

where $\mathbf{d}=\mathbf{d}(\mathbf{k})$ is the order parameter in the vector representation, $\mathbf{k}$ is a unit vector in orbital space, χ is the susceptibility, g is the gyromagnetic ratio, $\mathbf{H}$ is the total external magnetic field, and $\mathbf{R}_D$ is the dipole moment. In the B phase of superfluid ^{3}He, which will be the subject of discussion below, $\mathbf{d}(\mathbf{k})=\hat{\mathbf{R}}\mathbf{k}$, where $\hat{\mathbf{R}}$ is the rotation matrix in spin space, and it can be parametrized by the Euler angles or the rotation angle $\boldsymbol{\Theta}$ around a certain axis $\mathbf{n}$. The dipole moment arises because of the energy $\mathbf{F}_D$, which is due to the dipole–dipole interaction of the ^{3}He-B nuclei and depending on the relative orientation of the spin and orbital spaces:

$$\mathbf{F}_D = \frac{2}{15}\chi\left(\frac{\Omega_B}{g}\right)^2\left(\mathrm{Tr}\,\hat{\mathbf{R}} - \frac{1}{2}\right)^2, \tag{3}$$

where Q_B is the longitudinal-NMR frequency, characterizing the strength of the dipole–dipole interaction. The dipole energy determines the stable spin–orbit configurations and, coupling the motion of $\mathbf{M}$ and $\mathbf{d}$, leads to the existence of different NMR modes with different frequency and character of the motion of $\mathbf{M}$ and $\mathbf{d}$. The method of minimizing the dipole energy can be used to search for possible dynamic spin states. For precessing states, the angles determining the matrix $\hat{\mathbf{R}}$ are time-dependent and, generally speaking, $\mathbf{F}_D$ is also time-dependent. However, for $\Omega_B \ll gH$ this energy can be averaged over the

periods of the fast motions,[2] for which it is convenient to choose the frequency (ω_M) of the magnetization motion, close to the Larmor frequency ($\omega_L = gH$), and the precession frequency (ω_d) of **d** around the instantaneous direction of **M**, which, according to Eq. (2), is equal to gM/χ. The results of averaging depend strongly on the ratio of these frequencies, and the lowest energy is reached in the ''resonance'' case $\omega_M = \omega_d$ and, correspondingly, $M \simeq \chi H$. Soon after the superfluidity of ^{3}He was discovered, a number of NMR modes were also observed experimentally and studied — longitudinal oscillations, the Brinkman–Smith mode, the wall-pinned mode, and NMR on the spatial distribution of the order parameter. These modes all correspond to the ''resonance'' case or small oscillations near such distinguished spin–orbit configurations.

It was recently shown in Ref. 3 that other special cases for which the dipole energy is minimum and which likewise are called ''resonances'' can exist. In these cases the magnetization is $M_0/2$ or $2M_0$ (here $M_0 = \chi H$) and, correspondingly, the order parameter moves half as fast or twice as fast as **M**. Subsequent minimization of the average dipole energy $\overline{F_D}$ showed that there are two degenerate minima corresponding to the following precessing spin–orbit configurations:

$$s_z \simeq 0.307, \quad l_z \simeq 0.746; \tag{4a}$$

$$s_z \simeq 0.746, \quad l_z \simeq 0.307, \tag{4b}$$

where **s** is a unit vector in the spin direction, $\mathbf{l} = \hat{\mathbf{R}}\mathbf{s}$ is the unit orbital angular moment vector, indicating the direction of anisotropy of the B-phase gap in a magnetic field. If magnetic relaxation is neglected, then once it occupies one such state the system should remain in it, i.e., precession with nonequilibrium values of M can be stable. In the presence of an ac radio-frequency (rf) field with frequency $\omega_{\rm rf}$ (which compensates the magnetic relaxation and fixes the precession frequency of **M**), the sum of $\overline{F_D}$, the interaction energy of the magnetization with the rf field ($F_{\rm rf}$), and the ''spectroscopic'' energy (F_ω), arising because $\omega_{\rm rf}$ is different from ω_L (Ref. 4) must be minimized in a rotating coordinate system.

Precession states with **M** equal to half the equilibrium value (half-magnetization, HM states) were recently observed in continuous-wave NMR experiments.[5] In this work four NMR modes, corresponding to precession with magnetization close to half the equilibrium value and differing by the magnitude and shape of the NMR signal, were observed depending on the conditions. One other unusual precession state (zero-magnetization, ZM state) was also observed. This state, which corresponds to precession with a small magnetization ($0-0.3M_0$), still has no analytical description. Later, another mode was discovered. This mode probably also belongs to the family of HM states.[6]

As we have said, in the absence of an rf field the vector order parameter in the HM states precesses around the instantaneous direction of **M** with frequency $\omega_d = gM/\chi = \frac{1}{2}\omega_L$. This leads to oscillations of $\mathbf{R}_D$ with this frequency and, correspondingly, a component oscillating with frequency $\frac{1}{2}\omega_L$ should appear in the motion of **M**. It can be shown that its amplitude is of the order of $(\Omega_B/\omega_L)^2 M_0$. Such small magnetization oscillations in the HM states were studied theoretically in Ref. 7, where it was found that harmonics at the frequencies $\frac{1}{2}\omega_M, \frac{3}{2}\omega_M, \frac{5}{2}\omega_M$ and $\omega_M, 2\omega_M, 3\omega_M$ arise in the motion of all three components of **M**. The experimental observation of fractional NMR harmonics was the aim of the present work.

The measurements were performed in a cylindrical cell (3.5 mm in diameter and 4 mm high). The axis of the cell was oriented parallel to the constant magnetic field $\mathbf{H}_0$ and the filling channel of the cell was 0.7 mm in diameter and 4 mm long. The inner surface of the cell was covered with a smooth polymer (Lavsan) film to increase the surface relaxation time (in the normal phase at temperature close to $T_c = 0.93$ mK this time was ≈ 1.1 s). The experiments were performed at 0 bar pressure in 404 and 524 Oe magnetic fields (the NMR frequencies were 1308 and 1699 kHz). The standard continuous-wave NMR arrangement with two-section superconducting receiving and exciting coils oriented perpendicular to $\mathbf{H}_0$ was used to produce the HM states. The rf frequency was fixed and H_0 (and, correspondingly, ω_L) was varied. The transverse NMR signal at the rf frequency (we recall that $\omega_{\rm rf} = \omega_M$) was detected with a phase-sensitive amplifier. This made it possible to follow the change in the two orthogonal projections of the transverse magnetization — the variance and the absorption. In addition, a high-Q low-temperature circuit with a longitudinal superconducting coil, whose resonance frequency was 1/2 or 3/2 times the rf frequency, was used to detect the M_z oscillations. To improve the uniformity of the magnetic field the superconducting NMR coils were first transferred into the normal state in a field corresponding to the chosen frequency. The uniformity of the field H_0 over the cell was $(2-5)\times 10^{-5}$ in different experiments.

States with a nonequilibrium value of $\mathbf{M}$ arose with continuous passage of the NMR line with large amplitudes of the rf field (0.01–0.03 Oe) at the time the sample was heated from a temperature $\approx 0.95T_c$ up to the transition to the A phase ($0.986T_c$ for a 524 Oe field[8]). The states mentioned above were formed only in this narrow temperature range, since this requires that $\mathbf{M}$ be tipped by an angle $\beta \sim 180°$ away from the direction of $\mathbf{H}_0$ (Ref. 5), which is impossible at lower temperatures because of the large shift of the continuous-wave NMR signal for $\beta > 104°$. Once formed, however, the HM states can be cooled to much lower temperatures ($\sim 0.6T/T_c$ (Ref. 6)). We observed a wide spectrum of states with nonequilibrium magnetization (Fig. 1) for various temperatures and different shifts of the frequency from the Larmor value and for different directions of variation of the field. Aside from the states ZM, HM1, HM3, HM4, and HM5 observed in Refs. 5 and 6, in the region $\omega_L - \omega_{\rm rf} > 0$ one other HM state (HM6), which at large frequency shifts goes over to the HM4 state, was also observed. The state HM6 was identified as an HM state by measurements of the longitudinal and transverse components of $\mathbf{M}$. For this, as in Ref. 5, we measured the initial amplitude of the free-induction signal after the 90° rf pulses, which were applied with different phases at the moments when the continuous-wave rf field maintaining this state was switched off, and also the amplitude of the induction signal after the rf field was switched off in the absence of the tipping pulse. Computer simulations of NMR were also used to identify the states. The complete system of Leggett equations (in the variables $\mathbf{M}, \mathbf{n}$, and $\boldsymbol{\Theta}$ (Ref. 9)) for the spatially uniform case, taking account of the Leggett–Takagi relaxation terms, was solved. The results of the simulations agreed qualitatively with experiments for all states obtained with nonequilibrium magnetization, and not only the shape of the NMR signals (see Fig. 2) but also the sequence in which these states appeared with increasing temperature were reproduced. The small quantitative difference could be due to the uncertainty of $\tau_{\rm eff}$ (in the notation of Ref. 9) and also the fact that spatial inhomogeneities were neglected in these simulations. However, because of the high uniformity of the magnetic field and the strong rf field the motion of $\mathbf{M}$ in the experiment should be close to being spatially uniform.

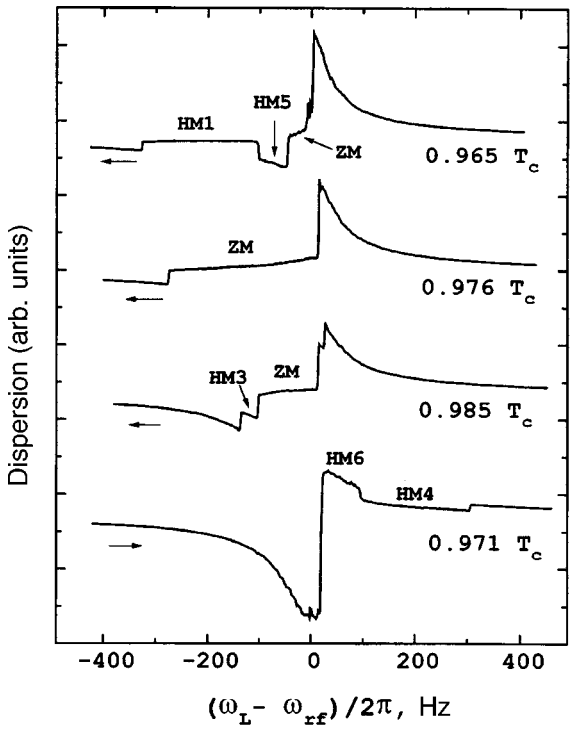

FIG. 1. Dispersion signals from states (marked by symbols) with nonequilibrium magnetization. The absorption is much smaller than the dispersion and is not shown. $\omega_{\rm rf}/2\pi = 1699$ kHz. The arrows show the direction of scanning of the field. The temperatures were estimated assuming the heating of the sample to be linear in time.

Comparing the experimental results and the simulations shows that the spin–orbit configurations in the states HM4 and HM6 are close to (4a) and (4b), respectively. The results of minimizing the sum $\overline{F}_D + F_\omega + F_{\rm rf}$ likewise describe well the dependence of the NMR signal in the states HM4 and HM6 on the frequency shift, and they make it possible to understand the nature of the transition between them. As the frequency shift $\omega_L - \omega_{\rm rf}$ increases, the minimum (4a) becomes deeper, while the minimum (4b) is smoothed out and, depending on the amplitude of the rf field and the temperature, either vanishes for some frequency shift without approaching the configuration (4a) or goes over smoothly to a configuration close to (4a). However, the energy minimization method mentioned above does not describe all of the states obtained in the experiment. The states observed in the region $\omega_L - \omega_{\rm rf} < 0$ (HM1, HM3, HM5) cannot be obtained in this manner, though they do arise in the numerical simulation. The simulations also showed that the orbital angular momentum vector $\mathbf{l}$ in the HM states precesses around $\mathbf{H}_0$ with frequency ~ 10 Hz, and $\mathbf{l} \perp \mathbf{H}_0$ in the states HM1 and HM5. In reality, $\mathbf{l}$ may not precess because of the orienting influence of the walls. However, the numerical simulation results remain virtually unchanged if terms fixing the direction of the projection of $\mathbf{l}$ on a plane perpendicular to $\mathbf{H}_0$ are added to the spin-dynamics equations.

Oscillations of the longitudinal component of the magnetization with frequency $\frac{1}{2}\omega_{\rm rf}$ or $\frac{3}{2}\omega_{\rm rf}$ were detected simultaneously with the signal at the main frequency. In the HM6

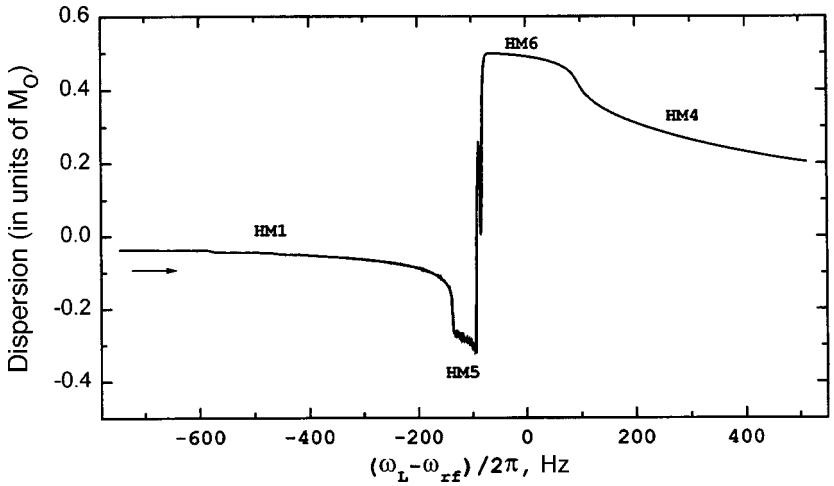

FIG. 2. Example of a dispersion signal (in units of M_0) for different HM states which was obtained as a result of computer simulations. The state HM1, whose formation process is not shown, was obtained first. Next, the passage of a line with increasing field (the arrow indicates the direction of passage) was simulated from this state. $\omega_{rf}/2\pi=1300$ kHz; rf field — 0.045 Oe; $T=0.956T_c$; $\tau_{eff}=4$ μs.

state such oscillations are clearly seen at both frequencies (Fig. 3). Their amplitude was a linear function of temperature. This is explained by the fact that $\Omega_B^2 \propto (1-T/T_c)$ at temperatures close to T_c. At temperature $0.98T_c$ the amplitude of the signal oscillations at half frequency, recalculated with the parameters of our spectrometer taken into account, was $\approx 10^{-5}$ times the maximum transverse NMR signal amplitude, in agreement with the simulation values and theoretical estimates.

In the HM3 state the amplitudes of the oscillations at frequency $\frac{1}{2}\omega_{rf}$ were appreciably smaller and the oscillations could be observed only after averaging eight successively recorded signals from the longitudinal coil. Fractional harmonics were not observed in the other HM states. We attempted to observe such signals also at frequencies shifted by several hundred hertz from $\frac{1}{2}\omega_{rf}$. The absence of fractional harmonics in the HM1 and HM5 states could possibly be explained by the fact that, according to the numerical simulations, in these states the order parameter moves with a frequency appreciably different (by ~ 0.2–2 kHz) from $\frac{1}{2}\omega_{rf}$, the difference depending on the frequency shift. On account of the residual nonuniformity of the external magnetic field, these oscillations in different parts of the experimental cell must dephase rapidly after the states are formed. Why there are no fractional harmonics in the HM4 state remains unclear. According to the numerical simulations, in this state (just as in the state HM6) the frequencies of the fractional harmonics are virtually independent of the frequency shift and they differ from $\frac{1}{2}\omega_{rf}$ and $\frac{3}{2}\omega_{rf}$ by not more than 1 Hz.

In closing, we note that the observation of NMR harmonics with frequencies $\frac{1}{2}\omega_{rf}$ and $\frac{3}{2}\omega_{rf}$ confirms the correctness of the identification of the HM states which we obtained. These harmonics are a manifestation of the motions of the order parameter of superfluid ^{3}He-B in NMR experiments and they indicate the existence of precession in the HM states at two different frequencies: magnetization precession at the main frequency and order-parameter precession at half the frequency.

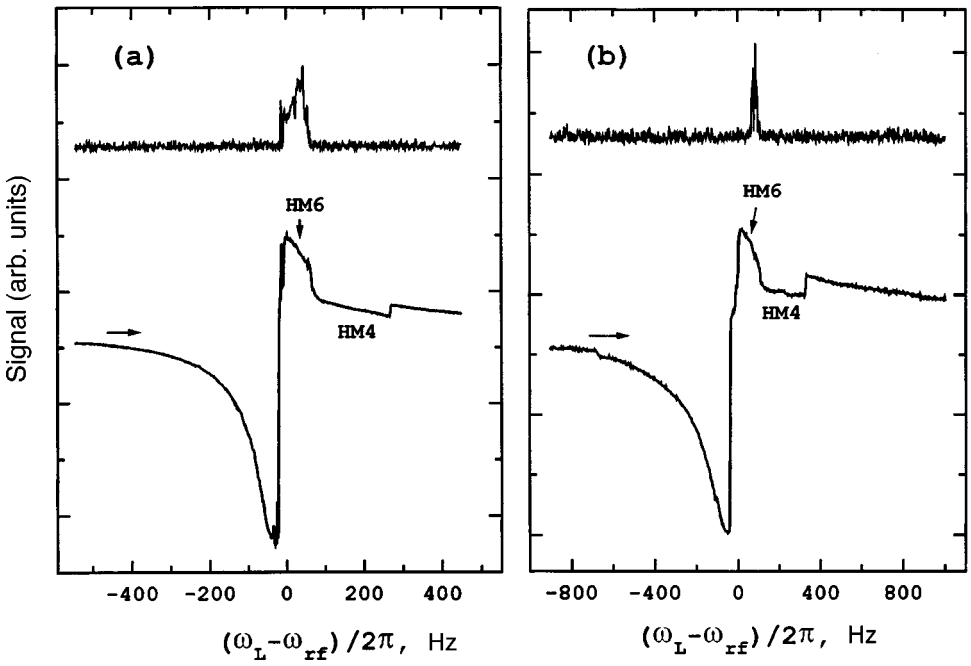

FIG. 3. Dispersion signal at the frequency $\omega_{\rm rf}$ (bottom) and amplitude of the signal at the fractional ($\frac{1}{2}\omega_{\rm rf}$ and $\frac{3}{2}\omega_{\rm rf}$) frequency (top). The arrow indicates the direction of scanning of the field. a — Signal at the frequency $\frac{1}{2}\omega_{\rm rf}$, $\omega_{\rm rf}/2\pi = 1699$ kHz, cold circuit $Q = 7000$, $T \approx 0.98T_c$. b — Signal at the frequency $\frac{3}{2}\omega_{\rm rf}$, $\omega_{\rm rf}/2\pi = 1308$ kHz, $Q = 3600$.

We thank I. A. Fomin and G. A. Kharadze for helpful discussions. This work was supported by the Russian Fund for Fundamental Research, the Ministry of Science of the Russian Federation, and Grants CRDF (RP1-249) and INTAS (96-0610). I. V. K. and D. V. P. are also grateful for a Landau Scholarship (Forschungzentrum, Jülich) for financial support.

[1] A. J. Leggett, Rev. Mod. Phys. **47**, 331 (1975).
[2] I. A. Fomin, Low Temp. Phys. **31**, 509 (1978).
[3] G. Kharadze and G. Vachnadze, JETP Lett. **56**, 458 (1992).
[4] G. E. Volovik, J. Phys.: Condens. Matter **5**, 1759 (1993).
[5] V. V. Dmitriev, I. V. Kosarev, M. Krusius *et al.*, Phys. Rev. Lett. **78**, 86 (1997).
[6] V. B. Eltsov, V. V. Dmitriev, M. Krusius *et al.*, Low Temp. Phys. **113**, 645 (1998).
[7] G. A. Kharadze, N. G. Suramlishvili, and G. E. Vachnadze, Fiz. Nizk. Temp. **23**, 803 (1997) [Low Temp. Phys. **23**, 602 (1997)].
[8] J. M. Kyynäräinen, J. P. Pekola, K. Torizuka *et al.*, Low Temp. Phys. **82**, 325 (1991).
[9] W. F. Brinkman and M. C. Cross, in *Progress in Low Temperature Physics*, edited by D. F. Brewer, North Holland Publ. Co., 1978, Vol. VIIA, p. 105.

Translated by M. E. Alferieff

Magnetic susceptibility and characteristic features of the electronic structure of quasicrystalline alloys

A. F. Prekul,* N. Yu. Kuz'min, and N. I. Shchegolikhina
Institute of Metal Physics, Urals Branch of the Russian Academy of Sciences, 620219 Ekaterinburg, Russia

(Submitted 4 November 1998; resubmitted 30 December 1998)
Pis'ma Zh. Éksp. Teor. Fiz. **69**, No. 3, 206–210 (10 February 1999)

Experiments are performed to determine the magnetic susceptibility of the icosahedral phase itself in the alloy $Al_{62}Cu_{25.5}Fe_{12.5}$ in the temperature range 3.9–1100 K. A new regularity is observed — the curves of the temperature dependences of the susceptibility and electrical conductivity are congruent. © *1999 American Institute of Physics.* [S0021-3640(99)01003-8]

PACS numbers: 75.30.Cr, 75.50.Bb, 71.23.Ft

1. Quasicrystals, as a state of solids with noncrystallographic lattice symmetry, have been attracting a great deal of attention since their discovery. Interest in quasicrystals from the standpoint of electronic physics has increased sharply in recent years in connection with the discovery of several so-called stable icosahedral (*i*) phases in the systems Al–Cu–Fe, Al–Cu–Ru, Al–Pd–Re, and Al–Pd–Mn. The reasons for this are easy to understand, since all the components of the enumerated systems are good metals and metastable quasicrystal-forming alloys, obtained by quenching from the liquid state, and their physical properties differ very little from those of the conventional high-resistance crystalline solid solutions and metallic glasses. Differences arise upon heat treatment of the quenched alloy, which produces a virtually homogeneous, very perfect *i* phase. In addition, the indications of dielectric behavior of the electrical and optical properties become sharply stronger.[1–3] Thus, the dc conductivity $\sigma_{4.2}$ decreases to 10–100 S/cm. A giant negative temperature coefficient of the resistance is observed in the entire temperature range of the existence of the *i* phase 0–1200 K, on account of which the conductivity in this interval varies by several factors of 10.

It seemed obvious that the semiconductor behavior of the electrical conductivity is due to the mechanism of thermal activation of the carriers. However, considerable difficulties have arisen in attempts[4] to use the conventional semiconductor-physics technique of linearizing the experimental $\sigma(T)$ curves in the coordinates $\ln\sigma$ versus $1/T$. This could be due either to the inapplicability of the classical relations of semiconductor physics to quasicrystals or to circumstances which complicate their applicability. It is not difficult to point out some such circumstances.

In the first place there is the residual conductivity, as a result of which the semiconductor behavior of the curves necessarily breaks down at low temperatures. In addition, the electrical conductivity depends not only on the charge-carrier density N_e but also on

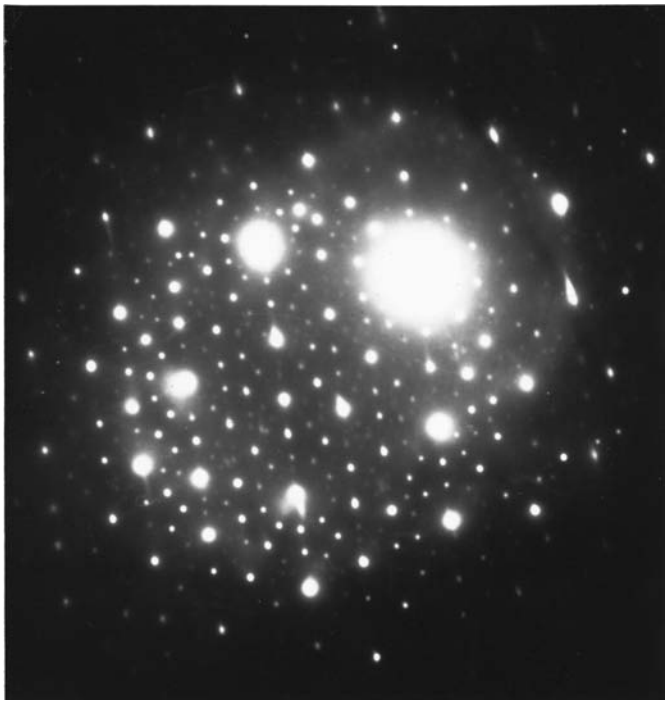

FIG. 1. Electron diffraction pattern of the crystalline phase. The fivefold symmetry axis is parallel to the electron beam.

the carrier mobility μ_e. If the temperature dependence of the latter does not follow the $T^{-3/2}$ law, then rectilinearizing coordinates of the general form $\ln(\sigma/T^{\alpha})-1/T$ must be used. It is obvious that the pre-exponential factor T^{α} becomes increasingly important as the activation parameter Δ decreases. For this reason there is hope of elucidating the situation with regard to the mechanism of thermal activation by studying the temperature behavior not of the kinetic but rather the thermodynamic coefficients, which obviously do not depend on the carrier mobility or, more precisely, on the carrier relaxation time. We studied the magnetic susceptibility of the *i* phase of the alloy $Al_{62}Cu_{25.5}Fe_{12.5}$ and we report here the main results of this investigation.

2. An alloy with the nominal composition $Al_{62}Cu_{25.5}Fe_{12.5}$ was prepared from highly pure components in an arc furnace, quenched on the water-cooled hearth by the ''hammer and anvil'' method and annealed in an ''especially pure'' helium atmosphere at 730 °C for 8 h. X-ray diffraction analysis shows that the main phase in the alloy after quenching is a β-solid solution with a CsCl lattice. An imperfect *i* phase and possibly an amorphous phase are present in small quantities. The main phase after annealing is a very perfect *i* phase (see Fig. 1). In addition, there are weak indications of a cubic phase, as is typical for real, massive samples with this composition.[5] Magnetic measurements were performed on two magnetometric setups. An MPMS-XL5 Quantum Design magnetometer was used in the temperature interval 3.9–400 K and a Domenicali balance was used in the interval 300–1100 K. Overlapping of the measurement ranges was used to match the low- and high-temperature results.

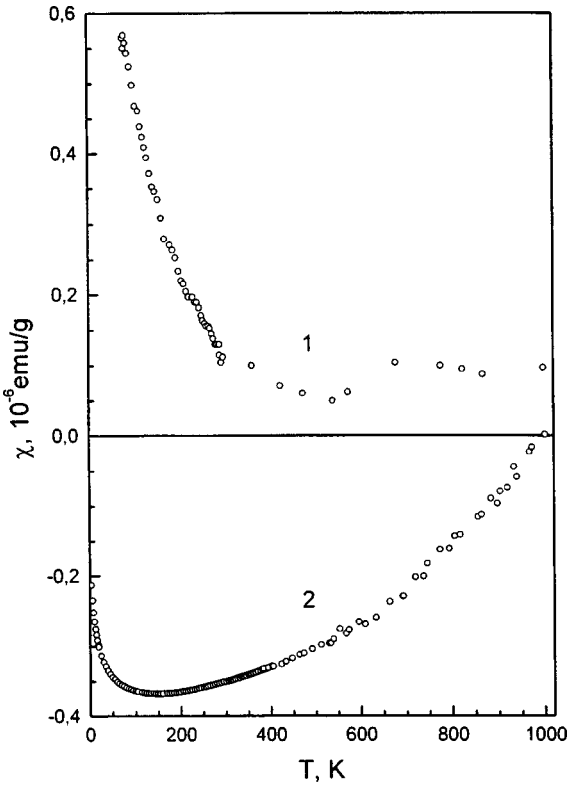

FIG. 2. Effect of the history of the alloy on its magnetic state: *1* — Quenched state; the main phase is a β-solid solution with the CsCl structure; *2* — annealed state; the main phase is icosahedral.

3. We show in Fig. 2 the results of a direct experiment for two states of the sample — before annealing (top curve) and after annealing (bottom curve) — for two purposes. First, it is evident that the magnetic properties of the alloy depend on the structure no less dramatically than do the electrical properties described above. These changes are of a pronounced dielectric character. The curve $\chi(T)$ for the quenched state of the sample lies entirely in the paramagnetic region, and the states after annealing lie in the diamagnetic region. In the second place, it is evident that a transition to the perfect *i* phase is accompanied by a decrease of the Curie-type paramagnetic component. In agreement with the conclusions of other investigators,[6,7] this attests to the fact that the minimum on the curve $\chi(T)$ for the annealed sample is not an intrinsic property of the *i* phase. It is due to a paramagnetic contribution associated either with the residues of the cubic phase and the magnetic moment on the Fe atoms in this phase or with uncontrolled magnetic impurities.

We employed the standard procedure for excluding such contributions by relating the Curie–Weiss curve to the experimental curve in the temperature range 3.9–40 K. The final result of this procedure is shown in Fig. 3 (curve *1*). We interpret this result as the temperature dependence of the magnetic susceptibility (χ_i) of the icosahedral phase itself in the entire temperature region in which this phase exists.

It is difficult to assess the obtained result apart from the other properties. For this

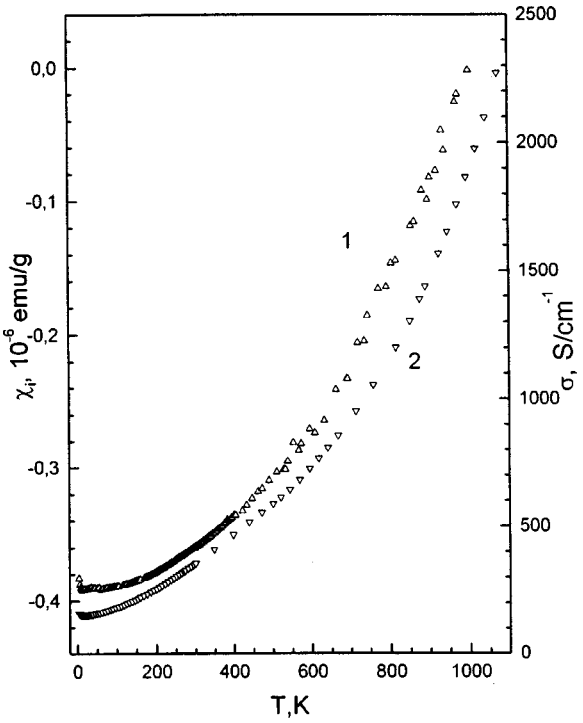

FIG. 3. Magnetic susceptibility and electric conductivity of the icosahedral phase itself.

reason, we present in Fig. 3 the curve $\sigma(T)$ which we obtained earlier for the same material. As one can see, the scale of variation of the magnetic susceptibility as a function of temperature is comparable to the scale of the variation of the electrical conductivity. When superposed, the curves virtually coincide. The small discrepancy at high temperatures does not count, since on the basis of the formal theories of conductivity and magnetism the temperature dependences $\sigma(T)$ and $\chi(T)$ differ neither more nor less than by a factor in the form of the characteristic carrier relaxation time. Therefore we can talk safely about the congruence of the curves $\chi_i(T)$ and $\sigma(T)$. The existence of this law is a very strong argument for the fact that *the change in the charge carrier density is the main temperature effect determining the behavior of the transport and thermodynamic coefficients.*

If this is so, it becomes interesting that the paramagnetism of the system becomes stronger as χ_i changes with increasing temperature. This is easy to understood assuming that the thermally activated carriers are a degenerate electron gas. Then, as is well known,[8] the temperature-dependent component of the magnetic susceptibility has the form

$$\chi_T \equiv (\chi_i - \chi_0) = AT^{1/2}\exp(-\Delta/T), \quad A = 2m_e^{3/2}k_B^{1/2}(2\pi\hbar^2)^{-3/2}\mu_B^2$$

(all the notation here is standard).

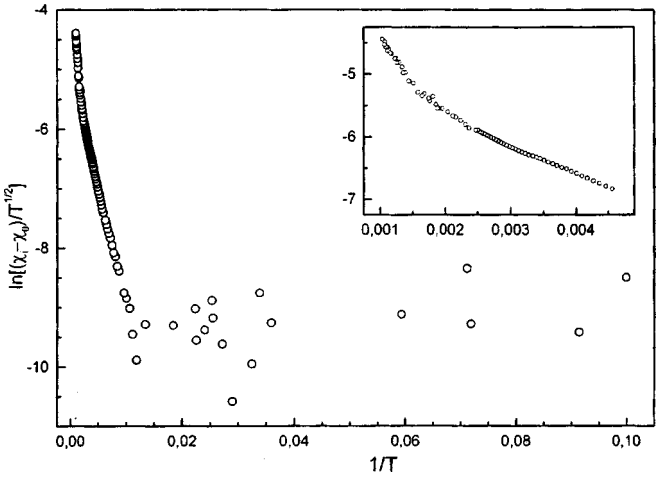

FIG. 4. Magnetic susceptibility of the i phase in the coordinates $\ln[(\chi_i-\chi_0)/\sqrt{T}]$ versus $1/T$.

In Fig. 4 the temperature dependence $\chi_i(T)$ is presented in the coordinates $\ln[(\chi_i-\chi_0)/\sqrt{T}]$ versus $1/T$. The inset shows on an enlarged scale the high-temperature part of the curve. It is easy to conclude from the form of the curve obtained that the *energy parameter of carrier activation is a very strong function of temperature.* At temperatures $T<100$ K the curve is essentially undefined. It is affected by the imperfection of the experimental samples and the uncertainty of the parasitic paramagnetic contribution. For this reason, the scale of variation of the parameter Δ can be roughly estimated as follows: from <0.01 eV at low temperatures to ~ 0.15 eV at high temperatures. This variation of the carrier activation parameter was neglected in previous work and led to the conclusion that the thermal activation mechanism is not realized in quasicrystalline materials.

4. It is now considered an established fact that the Fermi level of stable quasicrystalline phases lies inside a pseudogap of width 0.5–1 eV. The existence of such a feature of the electronic structure explains the stability of these phases, but it contributes little to the understanding of their physical properties, which derive from the electronic states in a ~ 0.1 eV layer near the Fermi energy. Practically nothing is known about the characteristics of this energy layer. In this context we wish to call attention not only to the inconstancy of the carrier activation parameter but also to the circumstance that broken-line segments are clearly seen on the part of the curve shown in the inset in Fig. 4. This could mean that the carrier activation parameter takes on a series of discrete values in the interval 0.01 eV $\leqslant\Delta\leqslant$0.15 eV. These are probably the first experimental indications of fine structure with a characteristic scale of several tens of meV inside the pseudogap.

We thank S. Z. Nazarov, S. M. Podgornykh, and A. V. Korolev for assistance in performing the experiment, and Yu. V. Kopaev, V. F. Gantmakher, and É. A. Neĭfel'd for a discussion of the results and a number of helpful suggestions.

This work was supported by the Russian Fund for Fundamental Research (Project 96-02-19586).

*e-mail: prekul@imp.uran.ru

[1] R. Haberkern, C. Roth, R. Knofler *et al.*, *Proceedings of the Sixth International Conference on Quasicrystals*, Tokyo, Japan, 1997, preprint.
[2] S. E. Burkov, T. Timusk, and N. W. Ascroft, J. Phys.: Condens. Matter **4**, 9447 (1992).
[3] A. F. Prekul, V. A. Kazantsev, E. V. Shalaeva *et al.*, JETP Lett. **67**, 203 (1998).
[4] D. Mayou, C. Berger, F. Cyrot-Lackmann *et al.*, Phys. Rev. Lett. **70**, 3915 (1993).
[5] T. Klein, A. Gozlan, C. Berger *et al.*, Europhys. Lett. **13**, 129 (1990).
[6] F. Cyrot-Lackman, C. Berger, A. Gozlan *et al.*, *International Symposium on the Physics and Chemistry of Finite Systems: From Clusters to Crystals*, Richmond, USA, 1991, preprint.
[7] S. Matsuo, T. Ishimasa, H. Nakano *et al.*, J. Phys. F: Met. Phys. **18**, L175 (1988).
[8] S. V. Vonsovskiĭ, *Magnetism* [in Russian], FB, Nauka, Moscow, 1971.

Translated by M. E. Alferieff

Raman scattering in germanium at high pressure: isotope effects

Yu. A. Timofeev, B. V. Vinogradov, and S. M. Stishov
Institute of High-Pressure Physics, Russian Academy of Sciences, 142092 Troitsk, Moscow Region, Russia

(Submitted 30 December 1998)
Pis'ma Zh. Éksp. Teor. Fiz. **69**, No. 3, 211–214 (10 February 1999)

The first-order Raman scattering in isotopically enriched samples of germanium ^{70}Ge, ^{72}Ge, and ^{74}Ge and germanium with the natural isotopic composition is investigated at high pressures. It is found that the isotopic dependence of the frequency of the $LTO(\Gamma)$ mode in isotopically pure germanium samples can be described in the harmonic approximation ($\nu \propto m^{-1/2}$). At the same time, the frequency of the $LTO(\Gamma)$ mode of germanium of natural isotopic composition apparently contains a contribution due to isotopic disorder effects. © *1999 American Institute of Physics.* [S0021-3640(99)01103-2]

PACS numbers: 78.30.Am, 62.50.+p

Interest in isotope effects in germanium has been stimulated to a large degree by the availability of highly-perfect isotopically-pure single-crystal samples. In one of the first works in this field the parameters of the unit cell of ^{74}Ge and germanium with the natural isotopic composition were measured with a three-crystal spectrometer at room and liquid-nitrogen temperatures.[1] The relative volume difference was found to be of the order of 10^{-5}, which corresponds to theoretical expectations for quantum effects of this kind in germanium. Indeed, it is easy to show that the relative volume difference between two isotopes at $T=0$ can be written in the form (see, for example, Ref. 2)

$$\Delta V/V \cong \Delta \Theta_D / E_c, \tag{1}$$

where $\Delta\Theta_D$ is the difference of the Debye temperatures and E_c is the binding energy. Setting $\Theta_D = 374$ K (Ref. 3) for germanium with the natural isotopic composition and taking account of the fact that $\Theta_D \propto m^{1/2}$, we obtain $\Theta_D = 370$ K for ^{74}Ge. Next, substituting into Eq. (1) $E_c = 3.87$ eV/atom,[3] we obtain $\Delta V/V \simeq 9\times 10^{-5}$, which is in good agreement with the experimental values. Similar estimates for the relative volume between natural germanium and ^{74}Ge give $\Delta V/V \simeq 2\times 10^{-4}$ at $T=0$ K. The corresponding experimental value[4] for $T=54$ K is 7.5×10^{-5}. More-accurate estimates of quantum effects in germanium were recently obtained by numerical modeling over a wide temperature range.[5] In any event, quantum effects in germanium are small and they are much more difficult to observe than in diamond. The corresponding estimates based on the quasiharmonic approximation show that the quantum contributions to the phonon fre-

TABLE I. Isotopic composition of germanium samples.

Isotope	70	72	73	74	76	
Mass, carbon units	69.924	71.922	72.923	73.921	75.921	
Sample	Isotope content, %					Average atomic mass
70	96.88	1.21	0.32	1.33	0.26	70.03±0.1
72	0.51	97.34	0.56	1.33	0.26	71.95±0.1
74	0.23	0.32	0.14	99.19	0.12	73.91±0.1
Natural	21.42	26.78	8.05	35.7	8.05	72.61±0.2

quencies of isotopically pure samples are too small to be observed. At the same time, isotope effects of a specific nature, namely, isotopic disorder, are apparently expressed just as strongly in germanium[6] as in diamond.[7]

In the present letter we report the results of investigations of first-order Raman scattering in germanium with different isotopic compositions at pressures up to 9 GPa and room temperature. The data obtained attest to a positive shift of the frequency of the $LTO(\Gamma)$ mode in isotopically disordered natural germanium relative to the corresponding frequency of the virtual crystal.

The Raman spectra were measured with a DFS-24 spectrometer, equipped with a system of holographic notch filters, and a CCD detector for recording the spectra. The Raman spectra were excited by the $\lambda = 479.886$ nm emission line of an argon laser. The detector was calibrated according to the emission spectra of a neon lamp. Pressure was produced using diamond anvils. Compressed helium served as the pressure medium. Four isotopically different samples of germanium and two pieces of ruby, each 25–30 μm in size, were placed simultaneously into the diamond cell. The single-crystal germanium samples were chipped from ingots with the corresponding isotopic composition. The luminescence line of ruby was used to measure the pressure. The temperature of the diamond cell was maintained at 20 °C to within ± 0.02 °C. The spectral position of the $LTO(\Gamma)$ Raman-scattering line was determined with an accuracy of the order of 0.1 cm^{-1}. The random error of the pressure measurements did not exceed 0.01 GPa. The isotopic composition of the samples is presented in Table I. Examples of the measured spectra are displayed in Fig. 1.

Figure 2 demonstrates the pressure dependence of the frequency of the $LTO(\Gamma)$ mode of isotopically different germanium samples. Calculations using the equation of state obtained in Ref. 8 for germanium show that the Grüneisen constant, characterizing the volume dependence of the frequency of the $LTO(\Gamma)$ mode, $\gamma \simeq 1$ ($\gamma = -(\partial \ln \nu / \partial \ln V)_T$) and is independent of the isotopic composition and pressure to within the accuracy of the experiments (see also Refs. 9 and 10 concerning this). Figure 3 displays the pressure dependence of the reduced frequencies $\nu^* = \nu m^{1/2}$ of the $LTO(\Gamma)$ mode of isotopically different samples of germanium. As one can see from the figure, the dependence $\nu^*(P)$ for isotopically ''pure'' germanium samples (see Table I) can be described by a single curve. At the same time $\nu(P)$ for a natural germanium sample,

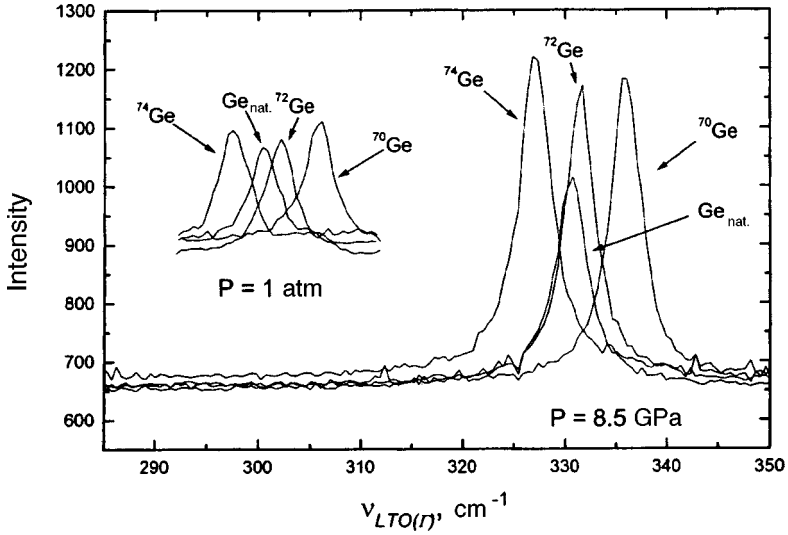

FIG. 1. Examples of first-order Raman spectra in isotopically different germanium samples.

which is an example of a system with isotopic disorder, cannot be brought by a similar transformation to the functional form characterizing a pure isotope. Therefore in the case of natural germanium the energy of $LTO(\Gamma)$ phonons is apparently renormalized as a result of isotopic disorder.[7,8,11] It follows from Fig. 3 that the corresponding ''renormalization'' contribution varies from 0.3 to 0.6 cm^{-1} depending on the pressure. In a recent work,[12] the ''renormalization'' energy shift of the $LTO(\Gamma)$ phonon in germanium with the natural isotopic composition is estimated to be 0.34 cm^{-1} at normal pressure and $T \simeq 10$ K, which, generally speaking, agrees with the present results.

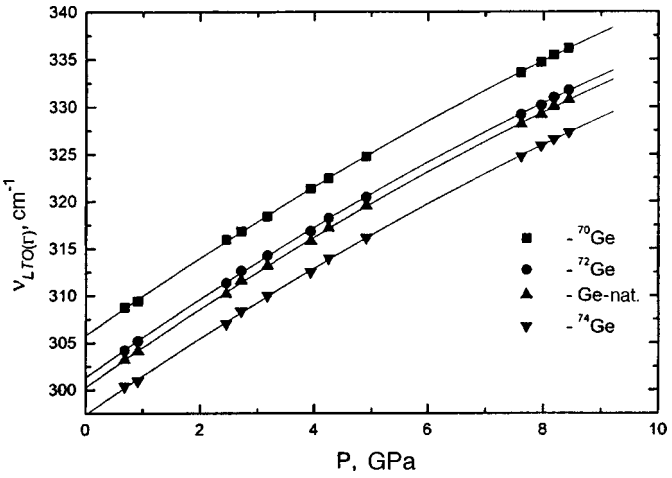

FIG. 2. Frequency of the $LTO(\Gamma)$ mode in isotopically different germanium samples versus pressure.

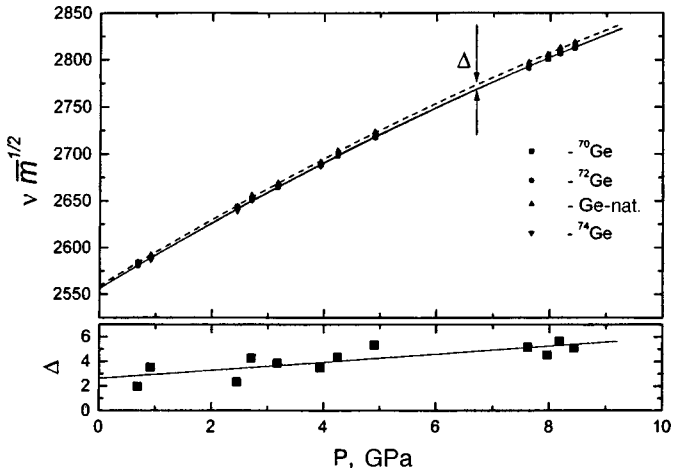

FIG. 3. Reduced frequency $\nu m^{1/2}$ of the $LTO(\Gamma)$ mode in isotopically different germanium samples versus pressure.

In conclusion, we call attention to the fact that Fig. 3 demonstrates convincingly the quasiharmonic character of $LTO(\Gamma)$ oscillations in isotopically pure germanium. It is obvious that in this case a simple harmonic expression can be used for the vibrational frequency $\nu=(k/m^*)^{1/2}$, bearing in mind the fact that the force constant k depends on the density. Since there is no reason to believe that the force constant depends on the isotopic disorder, the problem of calculating the corresponding frequency in an isotopically disordered crystal reduces to the ''correct'' calculation of the reduced mass m^*. Then the results presented in Fig. 3 possibly show that the reduced mass depends on the density. However, the accuracy of the present experimental data is too low to make more definite assertions.

[1] R. C. Buschert, A. F. Merlini, S. Face *et al.*, Phys. Rev. B **38**, 5219 (1988).
[2] M. Muinov, H. Kanda, and S. M. Stishov, Phys. Rev. B **50**, 13860 (1994).
[3] C. Kittel, *Introduction to Solid State Physics*, 4th ed., Wiley, New York, 1971.
[4] A. Kazimirov, J. Zegenhagen, and M. Cardona, Science **282**, 930 (1998).
[5] J. C. Noya, C. P. Herrero, and R. Ramirez, Phys. Rev. B **56**, 237 (1997).
[6] H. D. Fuchs, C. H. Grein, C. Thomsen *et al.*, Phys. Rev. B **43**, 4835 (1991).
[7] K. C. Hass, M. A. Tamor, T. R. Anthony, and W. F. Banholzer, Phys. Rev. B **45**, 7171 (1992).
[8] V. A. Goncharova, E. V. Chernyshova, and F. F. Voronov, Fiz. Tverd. Tela (Leningrad) **25**, 3680 (1983) [Sov. Phys. Solid State **25**, 2118 (1983)].
[9] D. Olego and M. Cardona, Phys. Rev. B **25**, 1151 (1982).
[10] I. V. Aleksandrov, A. F. Goncharov, A. N. Zisman, and S. M. Stishov, Zh. Éksp. Teor. Fiz. **93**, 680 (1987) [Sov. Phys. JETP **66**, 384 (1987)].
[11] D. T. Wang, A. Göbel, J. Zegenhagen, and M. Cardona, Phys. Rev. B **56**, 13167 (1997).
[12] J. M. Zhang, M. Giehler, A. Göbel *et al.*, Phys. Rev. B **57**, 1348 (1998).

Translated by M. E. Alferieff

On the role of umklapp processes in the scattering of delocalized positronium by acoustic phonons in ionic crystals

I. V. Bondarev*
Scientific-Research Institute of Nuclear Problems, Belarus State University, 220050 Minsk, Belarus

(Submitted 5 January 1999)
Pis'ma Zh. Éksp. Teor. Fiz. **69**, No. 3, 215–219 (10 February 1999)

The effect of umklapp processes in the scattering of delocalized positronium atoms by acoustic phonons in ionic crystals is analyzed. It is shown that at temperatures above which this effect becomes large, umklapp scattering renormalizes the constant of the deformation potential of positronium. This renormalization has recently been observed in experiments measuring the momentum distribution of delocalized positronium in a MgF_2 crystal. © *1999 American Institute of Physics.* [S0021-3640(99)01203-7]

PACS numbers: 71.60.+z, 63.20.−e, 36.10.Dr

The formation of positronium (Ps) — a bound system of an electron and a positron — in most crystalline dielectrics is now a well-established experimental fact.[1] In well-purified alkali-halide crystals (AHCs) and in crystalline quartz (α-SiO_2) at low temperatures (below several tens of K) a Ps atom is delocalized and is in a Bloch-type state. The formation of Bloch positronium is confirmed by the experimental observation of narrow peaks (a central peak and satellites separated by a distance which is inversely proportional to the lattice period) in the momentum distribution of the 2γ-decay photons when the crystals are irradiated with low-energy positrons. As the temperature increases, it is observed in the momentum distribution of the decay photons that the satellite peaks vanish and the central peak is sharply broadened, attesting to localization of Ps.[2] This thermally activated self-localization of positronium has been observed in almost all AHCs and has been analyzed theoretically in Refs. 3 and 4. Recent experiments have shown that only MgF_2 and α-SiO_2 crystals are exceptions.[5] In these crystals the Ps atom remains delocalized all the way up to temperatures $T\sim 700$ K (a theoretical explanation of this fact was given in Ref. 4). In MgF_2 a sharp broadening of the central and satellite positronium peaks is observed at temperatures above 200 K, and it cannot be explained by the normal scattering of Ps by longitudinal acoustic phonons. The effect looks as if an additional scattering mechanism, which renormalizes the deformation potential constant of positronium in a manner so as to increase it by more than a factor of 2 in a narrow temperature range from 200 to 355 K, is activated at temperatures above 200 K. A similar effect has not been observed in α-SiO_2, where the temperature broadening of the central and satellite positronium peaks in the temperature range 80–700 K is explained well by the normal scattering of positronium by acoustic phonons.

In the present letter we examine the role of umklapp processes in the scattering of Bloch Ps by acoustic phonons in ionic crystals. It is shown that at temperatures above which umklapp scattering becomes important it renormalizes the deformation potential constant of positronium. The manifestation of this effect for Ps in MgF_2 and α-SiO_2 crystals is analyzed.

Interaction of positronium with acoustic phonons with umklapp processes taken into account. We shall examine the interaction of Bloch Ps with acoustic phonons on the basis of the Bardeen–Shockley deformation potential theory.[6] Since the Ps atom is electrically neutral, we shall neglect the interaction of Ps with polar optical phonons in AHCs.[7] Then the total Hamiltonian (including umklapp processes) describing the interaction of Ps with longitudinal acoustic phonons has the form[8]

$$H_{\rm int}=\sum_{\mathbf{k},\mathbf{q},\mathbf{g}} V_a(\mathbf{q})\, a^{+}_{\mathbf{k}+\mathbf{q}+\mathbf{g}} a_{\mathbf{k}} (b_{\mathbf{q}}-b^{+}_{-\mathbf{q}})\,. \tag{1}$$

Here $a^{+}_{\mathbf{k}}(a_{\mathbf{k}})$ are creation (annihilation) operators for a Ps atom with quasimomentum $\mathbf{k}$, $b^{+}_{\mathbf{q}}(b_{\mathbf{q}})$ are creation (annihilation) operators for a longitudinal acoustic phonon with wave vector $\mathbf{q}$ and frequency $\omega(\mathbf{q})$, $\mathbf{g}$ is a reciprocal lattice vector of the crystal satisfying the relation

$$\mathbf{k}+\mathbf{q}+\mathbf{g}=\mathbf{k}', \tag{2}$$

where $\mathbf{k}$ and $\mathbf{k}'$ are quasimomentum vectors of positronium before and after scattering by a phonon with wave vector $\mathbf{q}$, respectively. The interaction matrix element $V_a(\mathbf{q})$ has the form[4]

$$V_a(\mathbf{q})=2F_a(\mathbf{q})\,\langle 1S_{1/2}|\cos\!\left(\frac{\mathbf{q}\cdot\mathbf{r}}{2}\right)|1S_{1/2}\rangle=\frac{2F_a(\mathbf{q})}{(1+(q\,a_B/4)^2)^2}, \tag{3}$$

where the averaging extends over the $|1S_{1/2}\rangle$ ground state of the relative motion of the particles in the Ps atom, $\mathbf{r}$ is the radius vector of the relative motion, and a_B is the Bohr radius of positronium,

$$F_a(\mathbf{q})=-iE_d\,\sqrt{\frac{\hbar}{2NM\omega(\mathbf{q})}}\,|\mathbf{q}|\,, \tag{4}$$

where E_d is the deformation potential constant, N is the number of unit cells in the crystal, and M is the total mass of the atoms in a unit cell.

The interaction (1) consists of two parts. The term with $g=0$ corresponds to normal scattering by longitudinal acoustic phonons with the dispersion relation ordinarily approximated by a linear function $\omega(\mathbf{q})=uq$, where u is the average velocity of longitudinal acoustic waves in the crystal (see, for example, Ref. 8). The term with $\mathbf{g}\neq 0$ describes umklapp processes. Since the quasimomenta $\mathbf{k}$ and $\mathbf{k}'$ belong to the first Brillouin zone of the crystal, the condition (2) limits the number of nonzero vectors $\mathbf{g}$ over which summation is performed. Actually, nonzero vectors $\mathbf{g}$ are vectors connecting the center of the first Brillouin zone with the centers of the closest surrounding zones in reciprocal space. The characteristic quasimomentum of thermalized positronium can be estimated as $k/(g/2)\sim 10^{-2}\sqrt{T}$, i.e., the quasimomentum is small compared with its maximum value $g/2$ all the way up to temperatures of the order of several thousands of

kelvins. This means that umklapp processes should be primarily due to scattering of a Ps atom by phonons with large ($\sim g/2$) wave vectors. Then the sum $\mathbf{k}+\mathbf{q}$ in Eq. (2) exceeds the limiting value, and a nonzero reciprocal lattice vector $\mathbf{g}$ must be added to it in order that the quasimomentum $\mathbf{k}'$ after scattering once again be in the first Brillouin zone. This means that umklapp scattering, physically corresponding to scattering by large angles ($\sim \pi$), has occurred.

Evidently, the wave numbers of the umklapp phonons can be approximated, to a first approximation, by the constant $\overline{q}\sim g/2$. Their frequencies can be estimated (in the approximation of a simple cubic lattice with period a) from the dispersion relation for long-wavelength phonons:[8]

$$\omega(\mathbf{q})=\frac{2u}{a}\left|\sin\left(\frac{\mathbf{q}\cdot\mathbf{a}}{2}\right)\right|, \tag{5}$$

which for $\overline{q}=g/2=\pi/a$ gives the constant $\omega_1=2u/a$, corresponding to the characteristic temperature

$$T_1=\hbar\omega_1/k_B<T_D \tag{6}$$

(here k_B is Boltzmann's constant and T_D is the Debye temperature of the crystal), above which the umklapp scattering contribution to the total scattering of positronium by acoustic phonons becomes substantial. Then the matrix element $V_a^{(u)}(\mathbf{q})$ of the part of the interaction (1) that corresponds to umklapp processes can be assumed to be approximately constant and equal to $V_a^{(u)}(\overline{q})$. Then, with allowance for Eqs. (1)–(5), the corresponding Hamiltonian $H_{\rm int}^{(u)}$ describing umklapp processes assumes the form

$$H_{\rm int}^{(u)}\simeq V_a^{(u)}\sum_{\mathbf{k},\mathbf{q}} a^+_{\mathbf{k}+\mathbf{q}+\mathbf{g}}a_{\mathbf{k}}(b_{\mathbf{q}}-b^+_{-\mathbf{q}}), \tag{7}$$

where $V_a^{(u)}=-2iE_d^{(1)}\sqrt{\hbar/2MN\omega_1}$, $E_d^{(1)}=E_d\overline{q}\,\nu$ is the analog of the deformation potential constant for an umklapp process, ν is the number of nearest neighbors in the reciprocal space, and the small contribution from the relative motion of the constituent particles of the Ps atom is neglected (see Eq. (3)).

Renormalization of the deformation potential constant. In complete analogy with the Hamiltonian (1), the mass operator Ps interacting with the longitudinal acoustic phonons likewise consists of two parts:

$$\Sigma_{\mathbf{k}}(\omega)=\Sigma_{\mathbf{k}}^{(n)}(\omega)+\Sigma_{\mathbf{k}}^{(u)}(\omega), \tag{8}$$

corresponding to normal ($\Sigma_{\mathbf{k}}^{(n)}$) and umklapp ($\Sigma_{\mathbf{k}}^{(u)}$) processes. The umklapp contribution in second-order perturbation theory in the interaction (7) has the form

$$\begin{aligned}\Sigma_{\mathbf{k}}^{(u)}(\omega)&=\Delta_{\mathbf{k}}^{(u)}(\omega)-i\,\Gamma_{\mathbf{k}}^{(u)}(\omega)\\&=|V_a^{(u)}|^2\sum_{\mathbf{q}}\left\{\frac{n(\omega_1)+1}{\omega-E_{\mathbf{k}-\mathbf{q}+\mathbf{g}}-\hbar\omega_1+i\delta}+\frac{n(\omega_1)}{\omega-E_{\mathbf{k}+\mathbf{q}+\mathbf{g}}+\hbar\omega_1+i\delta}\right\},\end{aligned} \tag{9}$$

where $E_{\mathbf{k}+\mathbf{q}+\mathbf{g}}=E_{\mathbf{k}+\mathbf{q}}=\hbar^2(\mathbf{k}+\mathbf{q})^2/2M^*$ is the band energy of Ps, M^* is its band mass, and $n(\omega_1)=\{\exp(\hbar\omega_1/k_BT)-1\}^{-1}$ is the Bose–Einstein distribution function of umklapp

phonons. For the imaginary part of expression (9), which determines the damping of the quasiparticle positronium state as a result of umklapp scattering, we have

$$\Gamma_{\mathbf{k}}^{(u)}(\omega)=\pi|V_a^{(u)}|^2\sum_{\mathbf{q}}\{(n(\omega_1)+1)\,\delta(\omega-E_{\mathbf{k}-\mathbf{q}}-\hbar\omega_1)+n(\omega_1)\,\delta(\omega-E_{\mathbf{k}+\mathbf{q}}+\hbar\omega_1)\}. \tag{10}$$

From Eq. (10) with $\omega>\hbar\omega_1\gg\hbar^2k^2/2M^*$ we obtain

$$\Gamma_{\mathbf{k}}^{(u)}(\omega)\simeq\frac{E_d^{(1)\,2}(2M^*)^{3/2}n(\omega_1)}{\pi\hbar^2\rho\,\omega_1}\sqrt{\omega}\,, \tag{11}$$

where ρ is the density of the crystal. Then the imaginary part of the total mass operator (8) is

$$\Gamma_{\mathbf{k}}(\omega)=\Gamma_{\mathbf{k}}^{(n)}(\omega)+\Gamma_{\mathbf{k}}^{(u)}(\omega)=\frac{(2M^*)^{3/2}k_BT}{\pi\hbar^3\rho\,u^2}\left\{E_d^2+\frac{\hbar\,u^2E_d^{(1)\,2}n(\omega_1)}{\omega_1\,k_BT}\right\}\sqrt{\omega}\,, \tag{12}$$

where

$$\Gamma_{\mathbf{k}}^{(n)}(\omega)=\frac{E_d^2(2M^*)^{3/2}k_BT}{\pi\hbar^3\rho\,u^2}\sqrt{\omega} \tag{13}$$

is the imaginary part of the mass operator $\Sigma_{\mathbf{k}}^{(n)}(\omega)$ (see Eq. (8)), describing normal scattering processes (see, for example, Ref. 5, where the substitution $E_d\to 2E_d$ must be made in accordance with our definition of the interaction matrix element (3) and (4)). Expression (11) can be rewritten in the form

$$\Gamma_{\mathbf{k}}^{(n)}(\omega)=\frac{\tilde{E}_d^{\,2}(2M^*)^{3/2}k_BT}{\pi\hbar^3\rho\,u^2}\sqrt{\omega}\,, \tag{14}$$

where

$$\tilde{E}_d=\sqrt{E_d^2+\frac{\hbar\,u^2E_d^{(1)\,2}n(\omega_1)}{\omega_1k_BT}}\simeq\begin{cases}E_d, & \text{if } T<T_1\\ \sqrt{E_d^2+(uE_d^{(1)}/\omega_1)^2}, & \text{if } T>T_1\end{cases}, \tag{15}$$

whence it follows that umklapp processes at temperatures above which they become important renormalize the deformation potential constant E_d of positronium.

As we have said, the renormalization of the deformation potential constant E_d of delocalized Ps has been observed experimentally in a MgF_2 crystal at temperatures 200–355 K and has not been observed in α-SiO_2.[5] A gradual increase of E_d from 7.6/2 eV at $T<200$ K to 16/2 eV at $T>355$ K has been detected in a MgF_2 crystal (the values presented are a factor of two lower than in Ref. 5 in accordance with the notations adopted in the present letter; see also the explanations for Eq. (13)). The experimental results for MgF_2 can be easily explained from the standpoint of the model proposed above. Indeed, in MgF_2 the temperature T_1 estimated from Eq. (6) is $\sim$230 K (to obtain an estimate the value of the largest lattice constant of tetragonal MgF_2 ($c=3.06$ Å, $a=4.64$ Å)[9] was substituted for a in Eq. (6)). The experimental data of Ref. 10 averaged over the crystallographic directions were used for the speed of sound (so that $u\approx 7.1\times10^5$ cm/s). This means that an umklapp process is activated at temperatures

$T \gtrsim 200$ K. According to Eq. (15), the effective deformation potential constant of positronium increases gradually from E_d to $\sqrt{E_d^2+(uE_d^{(1)}/\omega_1)^2}$. The value of the ratio $E_d^{(1)}/\omega_1$ can be estimated by comparing with experimental data for temperatures above 355 K. This gives $E_d^{(1)}/\omega_1 \approx 1\times 10^{-5}$ eV·s/cm. Further, if ω_1 is estimated in accordance with Eq. (5) as $\omega_1 \approx 3\times 10^{13}$ s^{-1}, then we obtain for $E_d^{(1)}$ the reasonable value $E_d^{(1)} \approx 3 \times 10^8$ eV/cm. Estimates with a similar order of magnitude are obtained, for example, for the coupling constants characterizing intervalley electron scattering by phonons in semiconductors (see, for example, Ref. 11).

The fact that renormalization of the deformation potential constant has not been observed for positronium in α-SiO_2 is probably due to the uncertainty in its value in this crystal. In quartz the temperature T_1, according to Eq. (6), is ~ 170 K (data from Ref. 12 were used for this estimate). The value of the largest trigonal lattice constant of α-SiO_2 was substituted for a in Eq. (6), i.e., Umpklapp scattering should ''renormalize'' the constant E_d of positronium, starting at even lower temperatures than in MgF_2. However, the uncertainty in the value of E_d in quartz is, according to Ref. 5, 1.4 eV ($E_d = 3.6 \pm 0.7$ eV in the notations of Ref. 5), which is an order of magnitude worse than in MgF_2. Therefore an increase of E_d by a factor of 1.5–2 (as happens in MgF_2) as a result of Umpklapp processes could have been easily masked by the uncertainty in the value of E_d determined from the experimental data. In this connection, it would be extremely interesting to repeat the experiments on α-SiO_2 with a higher accuracy.

I thank L. I. Komarov, S. A. Kuten, and T. Hyodo for helpful discussions. This work was supported by the Ministry of Education and Science of the Republic of Belarus (Grant No. 19971274) and the Fund for Fundamental Research of the Belorussian National Academy of Sciences (Grant No. M97-054).

*e-mail: bond@inp.minsk.by

[1] T. Hyodo, in *Positron Annihilation*, edited by P. C. Jain, R. M. Singru, and K. P. Gopinathan, World Scientific, Singapore, 1985, p. 643.
[2] J. Kasai, T. Hyodo, and K. Fujiwara, J. Phys. Soc. Jpn. **57**, 329 (1988).
[3] I. V. Bondarev and T. Hyodo, Phys. Rev. B **57**, 11341 (1998).
[4] I. V. Bondarev, Phys. Rev. B **58**, 12011 (1998); Fiz. Tverd. Tela (St. Petersburg) **38**, 2038 (1996) [Phys. Solid State **38**, 1125 (1996)].
[5] Y. Nagai, M. Kakimoto, H. Ikari, and T. Hyodo, Mater. Sci. Forum **255-257**, 596 (1997).
[6] J. Bardeen and W. Shockley, Phys. Rev. **80**, 72 (1950).
[7] O. V. Boev and K. P. Aref'ev, Izv. Vyssh. Uchebn. Zaved. Fiz. **25**, 118 (1982).
[8] A. S. Davydov, *The Theory of Solids* [in Russian], Nauka, Moscow, 1976.
[9] B. P. Nikol'skiĭ (Ed.), *Handbook of Chemistry* [in Russian], Khimiya, Leningrad, 1971.
[10] K. S. Aleksandrov, L. A. Shabanova, and V. I. Zinenko, Phys. Solid State **33**, K1 (1969).
[11] B. K. Ridley, *Quantum Processes in Semiconductors*, Clarendon Press, Oxford, 1982; Mir, Moscow, 1986.
[12] M. P. Shaskol'skaya (Ed.), *Acoustic Crystals* [in Russian], Nauka, Moscow, 1982.

Translated by M. E. Alferieff

Flexoelectric polarization in nematic liquid crystals measured by a field on–off pyroelectric technique

L. M. Blinov

Institute of Crystallography, Russian Academy of Sciences, 117333 Moscow, Russia; Department of Electronic Engineering, Faculty of Engineering, Osaka University, 565-0871 Osaka, Japan

M. Ozaki and K. Yoshino

Department of Electronic Engineering, Faculty of Engineering, Osaka University, 565-0871 Osaka, Japan

(Submitted 5 January 1999)
Pis'ma Zh. Éksp. Teor. Fiz. **69**, No. 3, 220–225 (10 February 1999)

A novel technique based on the pyroelectric effect is developed for making direct measurements of the flexoelectric polarization $\mathbf{P}_f$ in hybrid aligned nematic cells. The pyroelectric response is measured first in the field-off regime and then with the bias field applied. The latter allows a direct comparison of $\mathbf{P}_f$ with the field-induced polarization over the whole range of the nematic phase of the standard compound 5CB. The sum of the flexoelectric coefficients (e_1+e_3) is shown to be negative, and its dependence on the nematic order parameter does not follow a simple law (linear or quadratic), as has been predicted theoretically. The dynamics of $\mathbf{P}_f$ is discussed in terms of the order parameter fluctuations. © *1999 American Institute of Physics.*
[S0021-3640(99)01303-1]

PACS numbers: 61.30.Gd, 77.70.+a, 77.84.Nh

Nematic liquid crystals are uniaxial media with a preferred direction of the molecular axes, called the director **n**. The states of the director **n** and $-\mathbf{n}$ are indistinguishable (no polar axis) and the nematic phase does not show spontaneous polarization. However, a macroscopic polarization may be induced by deformation, namely, by a bend or splay distortion of the director field[1,2]

$$\mathbf{P}_f = e_1 \mathbf{n}\,\mathrm{div}\,\mathbf{n} - e_3(\mathbf{n}\times\mathrm{curl}\,\mathbf{n}) \tag{1}$$

which consists of two terms with flexoelectric coefficients e_1 and e_3, related to the splay and bend distortions, respectively.

Despite the fact that flexoelectric effects often manifest themselves in electrooptical phenomena, defect formation, structural instabilities, etc.,[3] accurate measurements of $\mathbf{P}_f$ are still a challenge to researchers because the polarization is, as a rule, screened by free charge carriers and there is no simple way to switch it and observe polarization-reversal currents as is routinely done in the case of ferroelectric liquid crystals. What is usually measured is the converse effect: when an electric field is applied, the alignment of a

liquid crystal becomes distorted. Since the pioneering work of Ref. 4, different techniques have been suggested for measuring the flexoelectric coefficients,[5–8] but, in fact, the accuracy of those measurements is influenced by a number of parameters involved (dielectric anisotropy ϵ_a, birefringence, elastic moduli, field inhomogeneity, etc.), and additional problems arise in regard to determination of the sign of the effect (as to the collection of data, see Ref. 10).

The aim of the present paper is to show how the temperature dependence of the flexoelectric polarization may be measured directly to high accuracy in hybrid aligned nematic (HAN) sandwich cells, which are often used in electrooptical experiments. An experiment was carried out by a modified pyroelectric technique on the standard compound 4-pentyl-4'-cyanobiphenyl (5CB) for which, at present, no reliable experimental data are available.[10] For 5CB $\epsilon_a \gg 0$, and the sum (e_1+e_3) is especially difficult to be found from a converse flexoelectric effect due to the competing action of a strong dielectric torque. In addition, our technique allows the measurements of $\mathbf{P}_f$ dynamics on both sides of the nematic–isotropic-liquid phase transition.

In a HAN cell the director is oriented homeotropically (along the layer normal z) at one of two opposite limiting plates and homogeneously (along the x axis) at the other. Therefore, $\mathbf{n}=(\sin\vartheta,\ 0,\ \cos\vartheta)$ with $\vartheta_0=0$ at $z=0$ and $\vartheta_d=\pi/2$ at $z=d$, where $\vartheta(z)$ is the angle formed by the director with the normal (z) to the plates, and d is the layer thickness. In this case, from Eq. (1) we have:

$$P_x=(-e_1\sin^2\vartheta+e_3\cos^2\vartheta)\frac{d\vartheta}{dz}, \tag{2}$$

$$P_z=-\frac{1}{2}(e_1+e_3)\sin 2\vartheta\frac{d\vartheta}{dz}. \tag{3}$$

The P_z value averaged over cell thickness

$$\langle P_f^z\rangle=\frac{1}{d}\int_0^d P_f^z dz=\frac{e_1+e_3}{4d}(\cos 2\vartheta_d-\cos 2\vartheta_0)=-\frac{e_1+e_3}{2d} \tag{4}$$

might be measured by a pyroelectric technique if the opposite plates are made of conductive glasses. Indeed, by definition, the pyroelectric coefficient is $\gamma=dP_s/dT$, where P_s is the spontaneous polarization and T is the temperature. For a HAN cell P_f takes the place of P_s and, since the flexoelectric polarization vanishes in the isotropic (I) phase (just as P_s of a ferroelectric vanishes in a paraelectric phase), its temperature dependence in the nematic (N) phase may be found by integrating the pyroelectric coefficient starting from a certain temperature T_i well above the N–I transition:

$$P_f(T)=\int_{T_i}^{T}\gamma(T)dT. \tag{5}$$

In order to measure $\gamma(T)$ we have to change the temperature by a small amount ΔT and record a pyroelectric response, e.g., in the form of the voltage U_p across a load resistor R shunted by the input capacitance C. The most convenient, dynamic regime of measurements is based on heating a sample of area A by absorbed light from a pulsed

laser.[11–13] For a very fast (in comparison with RC) jump in temperature, by the end of the laser pulse t_p the pyroelectric voltage reaches a value $A\Delta T\gamma/C$ and then decays with the RC time constant:

$$U_p = -\frac{A\Delta T\gamma}{C}\exp\left(-\frac{t}{RC}\right). \tag{6}$$

On a longer time scale, U_p changes sign and, being much smaller, decays slowly with a thermal time constant.

For $\gamma(T)$ measurements, the main difficulty comes from uncertainty in determination of ΔT, which depends on the absorbed light intensity and the heat capacity of the liquid crystal layer. The latter problem is especially serious when one works in the vicinity of the first-order N–I phase transition (our case). In order to solve it we have developed a novel procedure based on comparison of the pyroelectric response originating from P_f with that resulting from the field-induced polarization, the latter serves as an internal label for calibration. Indeed, when an external dc field is applied to a sample, the field-induced polarization $P_i = \epsilon_0\chi E$ is added to the flexoelectric polarization. The induced polarization is temperature-dependent due to temperature dependence of the susceptibility $\chi(T)$ and contributes to a total, field-dependent pyroelectric coefficient:

$$\gamma(T,E) = \frac{d(P_f + P_i)}{dT} = \gamma + \gamma_i = \gamma + \epsilon_0 E\frac{d\chi}{dT}. \tag{7}$$

In our case, even for small fields (e.g., 1 V/μm) $\gamma_i \gg \gamma$, and the measurements of the field-induced response are very easy. The derivative $d\chi/dT = d\epsilon/dT$ is obtained from the independently measured dielectric permittivity. It is important that $\epsilon(T)$ has to be measured on the same cell with the same voltage as was applied during the pyroelectric measurements.

In our experiments, we used 10.2 μm and 20.5 μm thick HAN cells, prepared from ITO covered quartz plates. The opposite electrodes were covered with polyimide (unidirectionally rubbed) and silane layers for the homogeneous and homeotropic orientation, respectively. The cells were placed in a thermal jacket and irradiated by pulses of a Nd-YAG laser (Spectron Laser System) operating in the continuous wave regime (wavelength 1.064 μm, pulse duration $t_p = 100$ μs, frequency 5 Hz, average incident power 40 mW, spot of 5 mm diameter completely covering the 3×3.5 mm cell area). Much shorter pulses (Q-switched regime, $t_p = 20$ ns) were used to observe the kinetics of the response. The light was partially absorbed (about 38%) by both ITO electrodes, providing a temperature increment in the bulk about 0.05 K. The pyroelectric response was measured with zero and -9 V bias voltage by a digital oscilloscope ($R = 800$ kΩ). Dielectric measurements were made in the same jacket with the same bias voltage using an impedance analyser (Yokogawa-HP, model 4192A).

The zero-bias pyroelectric response of a 20.5 μm HAN cell to a heating laser pulse has a shape predicted by Eq. (6). The inset to Fig. 1 shows the temperature dependence of the pulse amplitude (squares). On cooling, at the I–N phase transition, the response increases from some background value, shows a sharp maximum, and then decreases. The signal is independent of the direction of irradiation (either from the front or rear electrode) and is positive when a homogeneously orienting electrode is grounded. This means that positive free charges compensating for a light-induced decrease in the flexo-

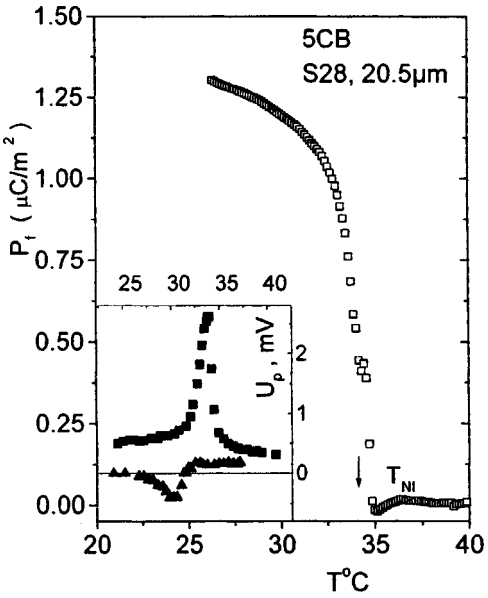

FIG. 1. Inset: Temperature dependence of the zero-bias pyroelectric response of a 20.5 μm HAN cell (filled squares) and a 20 μm homeotropic cell (filled triangles). Main plot: Flexoelectric polarization of the same HAN cell.

electric polarization are flowing through the load from the homogeneous to the homeotropic electrode. Therefore P_f is directed from the homeotropic to the homogeneous electrode, and the sum (e_1+e_3) is negative, opposite to the results of Ref. 9. The response of a reference cell with two homeotropically orienting electrodes is considerably weaker (also shown in the same inset, by triangles) and changes sign from negative to positive (in the nematic phase) when the direction of light beam is reversed. Evidently, there is a certain contribution to the response from the so-called surface polarization, which is also responsible for the background response in the isotropic phase. The existence of a surface polarization has been discussed for many years,[6,14] and the pyroelectric technique proves to be a powerful tool for its investigation.

After subtracting the background and integrating the pyroelectric response over temperature, we obtain the flexoelectric polarization, shown in the main plot of Fig. 1. The sharp increase is consistent with a first-order phase transition. The absolute value of P_f was found with the help of Fig. 2, which shows the pyroelectric response of the same cell with a bias voltage of -9 V applied. Now the amplitude of the signal is approximately 20 times higher. The signal comes from the temperature-dependent field-induced polarization due to $d\epsilon/dT$; see Eq. (7). The temperature dependence of the dielectric constant is shown in the inset to Fig. 2. The properly scaled derivative $d\epsilon/dT$ is shown in Fig. 2 by the dotted line. The latter is close to the pyroelectric response, and the ratio of the two gives a calibration curve that takes into account all of the unknown temperature-dependent factors mentioned above. With this calibration curve the $P_f(T)$ dependence shown in Fig. 1 has been found. The maximum value of P_f is 1.27 μC/m^2. For another cell of thickness 10.2 μm, the value of P_f found by the same procedure is 2.2 μC/m^2.

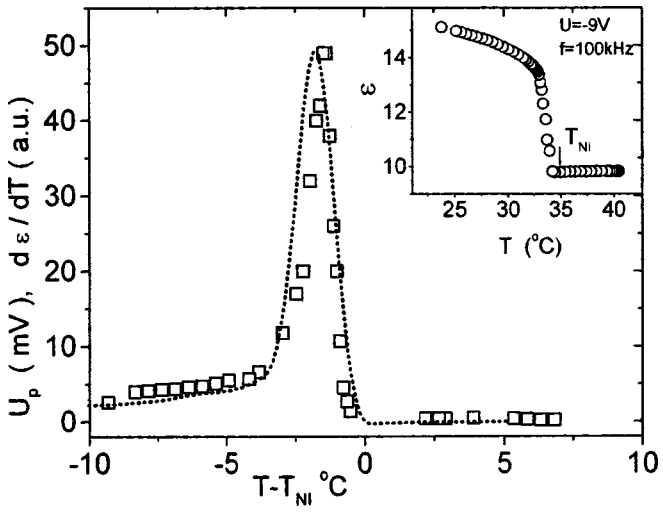

FIG. 2. Inset: Temperature dependence of dielectric constant at frequency 100 kHz for the same 20.5 μm HAN cell with a bias voltage of -9 V applied. Main plot: Pyroelectric response with a bias voltage of -9 V (open squares) and derivative $d\epsilon/dT$ scaled to compare it with the pyroelectric data (dotted line).

The corresponding flexo-coefficients (e_1+e_3) at 25 °C for the two cells are -53 pC/m $(1.6\times10^{-3}$ StatV) and -45.6 pC/m $(1.4\times10^{-3}$ StatV), respectively. For the second (thinner) cell, the decrease in (e_1+e_3) may be accounted for by a certain decrease in the difference of the two director angles at the boundaries, $\vartheta_d-\vartheta_0<\pi/2$, due to a finite anchoring energy. Generally speaking, the accuracy of P_f and (e_1+e_3) measurements (about 20%) is mainly determined by the proper allowance for the surface polarization background.

The sign of (e_1+e_3) corresponds to that found earlier,[13] but the present absolute value is almost an order of magnitude higher. The reason seems to be in the different calibration procedures. The earlier calibration was based on a comparison with a ferroelectric liquid crystal, which might exhibit a polarization screening effect under an applied bias voltage, and also had a different optical texture, resulting in additional light scattering and quite different thermal properties (the new calibration is free of those disadvantages). Now we can also recalculate the flexoelectric coefficients for another standard nematic, MBBA, from earlier pyroelectric measurements:[13] $(e_1+e_3)=-24$ pC/m. The negative sign and the magnitude are in agreement with the best data on MBBA in the literature.[10]

To shed more light on the mechanism of flexoelectricity, we have plotted the flexoelectric coefficients as a function of the orientational order parameter *S*. The linear and quadratic dependences were predicted for the quadrupolar[2] and dipolar[15] mechanisms. We have taken the data on the order parameter from Ref. 16 and plotted in Fig. 3 the (e_1+e_3) values for our 20.5 μm cell (from Fig. 1) as a function of *S*. The linear dependence may be seen only well below the N–I transition. Closer to the transition the slope increases dramatically. Such a complicated behavior is not surprising[17] if we remember that 5CB molecules have flexible tails and forms dimers due to the cyano-group

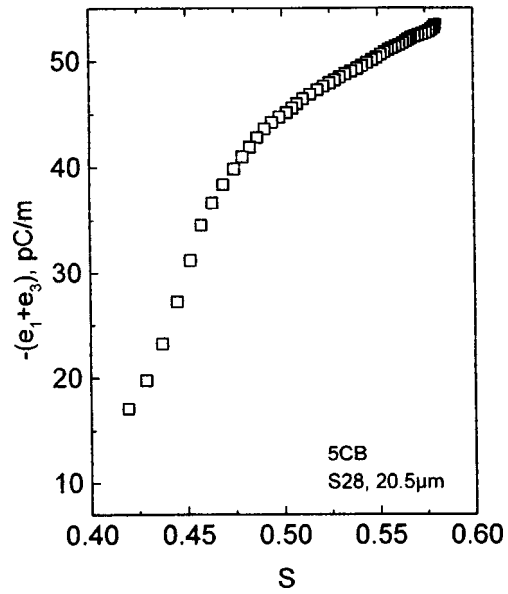

FIG. 3. Sum of the flexoelectric coefficients (e_1+e_3) as a function of the orientational order parameter.

interaction. Qualitatively same results were obtained with data on S taken from Refs. 18 and 19.

Figure 4 shows the rise time τ of the pyroelectric response to a 20 ns laser pulse. In full analogy with a discussion of the soft-mode relaxation times for ferroelectric liquid crystals,[20] τ may be referred to as an intrinsic dynamic time of the substance. On the assumption that angles ϑ_0 and ϑ_d are independent of temperature (0 and $\pi/2$), the

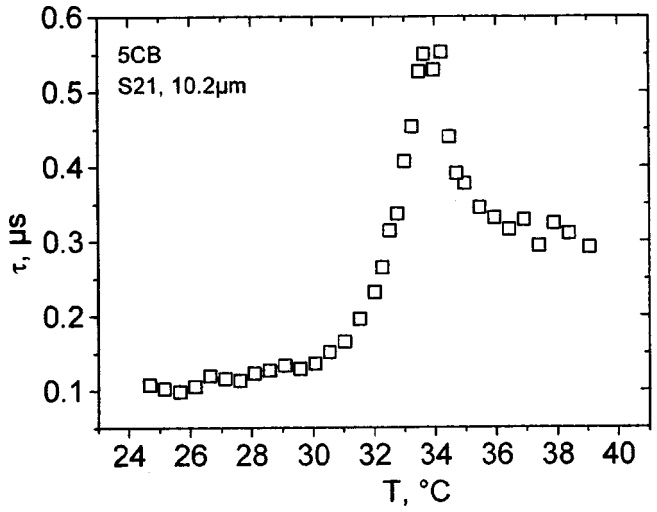

FIG. 4. Temperature dependences of the rise time of the pyroelectric response to a 20 ns laser pulse.

response time should correspond to dynamics of the flexoelectric coefficient dependent solely on the nematic order parameter. Indeed, the Kerr-effect measurements in the isotropic phase of 5CB near the I–N transition[21] show almost the same pretransitional behavior. In our case the dynamics of the order parameter is easily measured on the nematic side of the transition, which is difficult to do with other techniques. The inverse time τ^{-1} exhibits a Curie-type behavior with a slope -1.6×10^{6} $(\mathrm{sK})^{-1}$ in the range $T_c - T = 2$ K.

To conclude, we have developed a novel technique based on the pyroelectric effect for making direct measurements of the flexoelectric polarization in HAN cells. Importantly, calculations of the polarization and flexoelectric coefficients involve only two easily measurable physical parameters: the pyroelectric response, and the dielectric permittivity of the substance. An accurate determination of the sign and the absolute value of the polarization has been performed on a standard nematic liquid crystal 5CB; the sum of the flexoelectric coefficients $(e_1 + e_3)$ was shown to be negative (-53 pC/m at 25 °C) with a sharp temperature dependence. The kinetics of the response reveals the dynamics of the order parameter fluctuations on both sides of the N–I transition.

We thank Prof. A. G. Petrov and Dr. F. Tournilhac for helpful discussions and acknowledge the financial support of the Russian Fund for Fundamental Research (Grant 98-02-17071) and the Ministry of Education, Science, Sports and Culture, Japan (Grant-in-Aid for Scientific Research). L. B. thanks the Japanese Society for Promotion of Science for a fellowship at Osaka University.

[1] R. B. Meyer, Phys. Rev. Lett. **22**, 918 (1969).
[2] J. Prost and J. P. Marcerou, J. Phys. (Paris) **38**, 315 (1977).
[3] L. M. Blinov and V. G. Chigrinov, *Electrooptic Effects in Liquid Crystal Materials*, Springer-Verlag, New York, 1993.
[4] D. Schmidt, M. Schadt, and W. Helfrich, Z. Naturforsch. Teil A **27**, 277 (1972).
[5] J. P. Marcerou and J. Prost, Mol. Cryst. Liq. Cryst. **58**, 259 (1980).
[6] A. Derzhanski, A. Petrov and M. Mitov, J. Phys. (Paris) **39**, 273 (1978).
[7] I. Dozov, I. Penchev, Ph. Martinot-Lagarde and G. Durand, Ferroelectr. Lett. Sect. **2**, 135 (1984).
[8] P. R. Maheswara Murthy, V. A. Raghunatan, and N. V. Madhusudana, Liq. Cryst. **14**, 483 (1993).
[9] S. R. Warrier and N. V. Madhusudana, J. Phys. II **7**, 1789 (1997).
[10] A. Petrov, in *Physical Properties of Liquid Crystals*, edited by D. Dunmur, A. Fukuda and G. Luckhurst, EMIS Datareviews Series, 1999.
[11] J. Cooper, Rev. Sci. Instrum. **33**, 92 (1962).
[12] M. Simphony and S. Shaulov, J. Appl. Phys. **42**, 3741 (1971).
[13] L. A. Beresnev, L. M. Blinov, S. A. Davidyan *et al.*, JETP Lett. **45**, 755 (1987).
[14] P. Guyot-Sionnest, H. Hsiung, and Y. R. Shen, Phys. Rev. Lett. **57**, 2963 (1986).
[15] J. P. Straley, Phys. Rev. A **14**, 1835 (1976).
[16] E. M. Aver'yanov, V. A. Zhuikov, V. Ya. Zyryanov, and V. F. Shabanov, Zh. Éksp. Teor. Fiz. **86**, 2111 (1984) [Sov. Phys. JETP **59**, 1227 (1984)].
[17] M. A. Osipov, Sov. Phys. JETP **58**, 1167 (1984).
[18] J. W. Emsley, G. R. Luckhurst, and C. P. Stockley, Mol. Phys. **44**, 565 (1981).
[19] A. Buka and W. H. de Jeu, J. Phys. (Paris) **43**, 361 (1982).
[20] L. M. Blinov, S. Okazaki, M. Ozaki, and K. Yoshino, Mol. Mater. **9**, 163 (1998).
[21] V. N. Tsvetkov and E. I. Ryumtsev, Mol. Cryst. Liq. Cryst. **133**, 125 (1986).

Published in English in the original Russian journal. Edited by Steve Torstveit.

Short-pitch helicoidal modes in antiferroelectric liquid crystals and scattering of resonant x rays

M. V. Gorkunov and S. A. Pikin*
Institute of Crystallography, Russian Academy of Sciences, 117333 Moscow, Russia

W. Haase
Technical University of Darmstadt, Institute of Physical Chemistry, 64287 Darmstadt, Germany

(Submitted 10 January 1999)
Pis'ma Zh. Éksp. Teor. Fiz. **69**, No. 3, 226–231 (10 February 1999)

The structure of antiferro- and ferroelectric phases in chiral smectic liquid crystals is studied on the basis of the theory of modes with a short pitch. The existence of ferroelectric phases is explained both by the characteristic incommensurability of short-pitch modes with respect to the thickness of the smectic layer and by distortions of the short-pitch antiferroelectric structure of a long-wavelength mode. It is pointed out that the details of the short-pitch order can be observed in resonant x-ray scattering. The fundamental features of the pattern of such scattering in the phases considered are predicted. © *1999 American Institute of Physics.* [S0021-3640(99)01403-6]

PACS numbers: 77.84.Nh, 77.80.Bh, 61.30.Eb

1. There exist several different theoretical approaches for explaining the observed large number of ferro-, antiferro-, and ferrielectric phases in type-C chiral smectic liquid crystals.[1–9] For example, modifications of the Ising model[1–4] invoke relatively large intermolecular interaction radii, the interactions changing sign as a function of the distance between the molecules. This can be explained physically by the large smectic correlation lengths ξ, which are much greater than the length l of the molecules, and by the competition between dipole–dipole and steric interactions. These models give a qualitative understanding of the role of large-scale correlations, but they strongly limit the freedom of possible orientations of the C director in the smectic plane. The ''two-layer'' model[5–7] assumes a repeating unit cell consisting of two smectic layers. The so-called clock model[8] assumes that the C director rotates by the same angle on passing from one layer to another. In the proposed model with short-pitch modes (SPMs)[9] the antiferro- and ferrielectric phases are described as structures with definite sets of helicoidal modulations. The wave number of such modes is close to a rational number of smectic layers, and the number of possible modes is limited by the aforementioned smectic correlations. The prediction of the structure of large families of observed phases[9] raised the question of the real molecular ordering in the new class of substances, and clarity started to appear in this question only as a result of recent experiments.[10]

According to the SPM model in neglect of weak chiral effects, in a region with

characteristic size ξ along the z axis of the crystal the dipoles can be oriented along certain directions in the smectic plane with equal probability. This means that the energies of the corresponding states are equal and determine the leading term in the free energy. Depending on the stacking of the molecules, these states can be described by the distribution function $\exp(i\pi kz)$ with wave numbers $k=m/nl$, where $m=1,2,\ldots$ and $n=\pm m,\pm(m+1),\ldots$. The spatial periods of these structures $2nl/m$, where $2n/m$ is an integer, are greater than or equal to twice the thickness of the layers, but they must be less than the correlation length ξ, i.e., $k>1/\xi$ or $n/m<\xi/l$. Then we shall represent the leading term in the energy as $\sin^2(m\pi/ql)$. It vanishes at $q=k$ and increases sharply for $q\neq k$. For fixed m a SPM with $n<m\xi/2l$ can indeed exist. However, if $n/m>\xi/l$, then modulations with small q (similar to the standard optical helicoid in the C* phase), for which the leading term in the energy is proportional to q^2, must also be considered. The corresponding calculations[9] show that the thermodynamically favorable wave numbers of SPMs should differ somewhat from the corresponding k. This incommensurability is small and equals

$$\delta q_n^m \cong -\frac{1}{l}\left(\frac{nl^2\nu}{m\xi^2}+(-1)^n\frac{m\alpha}{n^2\pi}\right), \tag{1}$$

where ν is the squared ratio of the correlation lengths along and perpendicular to the crystal axis, while α is a small chirality parameter.

The wave vector of a long-wavelength mode (LWM) is given by

$$q_L \cong l\alpha\nu/m\pi\lambda^2, \tag{2}$$

where λ is the longitudinal correlation length appearing in the chiral part of the free energy and is close in magnitude to ξ. It is obvious that the simultaneous existence of the SPM and LWM should distort the ideal screw structure of the pure SPM. This will be examined below.

Scattering of resonant x-ray waves makes it possible to observe directly the details of the short-pitch order in liquid-crystal antiferro- and ferrielectrics. The results of the latest experiments[10] confirm the existence of short-pitch structures in these phases, showing, specifically, that the period of the short-step structure is close to $2l$ in the antiferroelectric phase AF and to $3l$ and $4l$ in the ferrielectric phases FI1 and FI2, respectively. Analysis of the heights of the resonance scattering peaks, performed using Dmitrienko's approach,[11] showed that the results obtained cannot be attributed to the structures proposed by the Ising model. At the same time, it was correctly concluded in Ref. 10 that the so-called clock structures, which are essentially pure SPMs, can produce the observed scattering pattern.

The steric interactions between molecules occupying neighboring layers strongly depend on the relative orientation of these layers.[1] For this reason, a strong change in the relative azimuthal orientation along the z axis should lead to the appearance of a superlayer periodicity in the density wave. The absence of nonresonance peaks corresponding to such a periodicity in experiments shows that, in a certain sense, all layers are subject to virtually identical conditions. This provides another argument against the ''Ising'' structures, indicating at the same time that in the phases studied the distortion of the SPMs by a long-pitch helicoid is small.

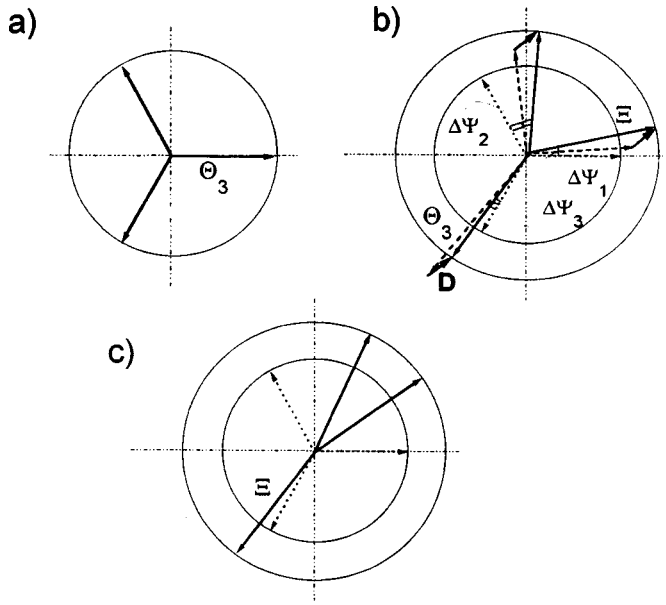

FIG. 1. Three-layer unit cell of a triple SPM. The arrows show the projections of the director on the *xy* plane in three successive layers: a) pure SPM, b) SPM in the presence of a weak LWM (the broken arrows correspond to unequal projections of the director in an antiferroelectric SPM), c) triple SPM in the case of a strong LWM (a structure close to an ''Ising'' structure).

2. Thus the unit cell of a smectic with short-pitch order consists of N layers. The azimuthal component of the C director in the sth layer of a cell makes an angle Ψ_s with the azimuthal component in the first layer. In a pure SPM undistorted by a LWM, because the average dipole moments **p** of molecules in a layer make a fixed angle with the C director of the layer, the polarization in the unit cell is completely compensated and

$$\Psi_s=(s-1)2\pi/N. \tag{3}$$

In studying the structural details of a SPM distorted by a relatively weak LWM the latter can be reduced to a displacement **D** imposed on the initial structure (3). This displacement, specifically, gives rise to an uncompensated polarization in the unit cell, i.e., to ferrielectricity. Then, under the condition that the thickness of the smectic layers remains the same, the angles Ψ_s experience small changes. The corrections to them which are linear in **D** can be expressed as

$$\Delta\Psi_s=-\frac{2D}{\Xi}\sin(\Psi_s-\varphi_D), \tag{4}$$

where Ξ is the tilt angle of the molecules and φ_D is the azimuthal angle of the director **D**.

As an example, let us consider the distortion of an SPM with $N=3$. In the absence of a LWM, the projections of the director of the layers in a unit cell on the *xy* plane form a three-ray star with different angles Θ_3, as shown in Fig. 1a. When the displacements **D** are superposed, the director in the layers rotates (see Fig. 1b) in such a way that the rays

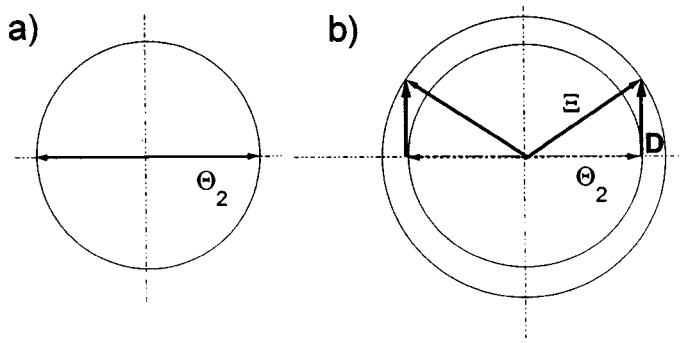

FIG. 2. Two-layer unit cell in a double SPM: a— pure two-layer SPM, b— same in the presence of a LWM.

of the SPM (dotted line) are unequal but the observed total projections of the director (solid arrows) are equal, which indicates that the tilt angle of the molecules in the layers is the same and therefore the layer thicknesses are the same. Figure 1c demonstrates the hypothetical situation of a strong LWM, where strong deformation of the unit cell occurs and the structure of the cell becomes similar to an ''Ising'' cell.

An undistorted SPM with $N=2$ is shown in Fig. 2a. If the displacement **D** is perpendicular to the initial direction of the rays, then a cell can deform in such a way that the thickness of the layers remains the same (Fig. 2b). It is obvious that it is not possible to ensure the same thickness for all layers for other orientations of the cell relative to the displacement **D**. This is unfavorable from the standpoint of the high elastic energy. For this reason, a two-ray star should rotate along the z axis so as to remain approximately perpendicular to the vector **D**.

3. To determine the possibilities of resonant x-ray scattering for investigations of the details of the short-pitch order, let us consider a layered medium whose unit cell is described above. The incommensurability of the structure can be taken into account by assuming that the t th cell is rotated by an angle $t\delta$ around the z axis relative to a certain zeroth cell and $\delta=Nl\delta q$. Then the x-ray susceptibility assumes the form

$$\hat{\chi}(z)=\sum_{t=-\infty}^{\infty}\hat{R}_{t\delta}\hat{\chi}^{uc}(z+tNl)\hat{R}_{-t\delta}, \tag{5}$$

where $\hat{R}_{\varphi}$ is a matrix representing rotation by the angle φ around the z axis, $\hat{\chi}^{uc}(z)$ is the susceptibility of the unit cell

$$\hat{\chi}^{uc}(z)=\sum_{s=1}^{N}\hat{R}_{\Psi_s}\hat{\chi}^{(0)}(z+sl)\hat{R}_{-\Psi_s}, \tag{6}$$

and $\hat{\chi}^{(0)}$ is the susceptibility of a single smectic layer.

The Fourier transform of the function (5)

$$\hat{\chi}(q)=\sum_{t=-\infty}^{\infty}\sum_{s=1}^{N}\exp[iql(tN+s)]\hat{R}_{\Psi_s+t\delta}\hat{\chi}^{(0)}(q)\hat{R}_{-\Psi_s-t\delta} \tag{7}$$

after transformations of the matrix product decomposes into terms corresponding to the isotropic part of the susceptibility (which contributes to the nonresonant scattering), and terms determined by the anisotropy of $\hat{\chi}^{(0)}$, which is large only near the resonant frequencies and contributes to resonant scattering. Following the notations adopted in Ref. 11, it is convenient to classify the latter according to the dependence of the scattering intensity on the polarization of the incident wave. Thus, type-I scattering does not depend on the polarization, while type-II scattering does depend on the polarization.

The resonant scattering peaks are found to lie at

$$Q=t/N-M(\delta/2\pi N), \tag{8}$$

where $Q=ql/2\pi$, and $M=\pm 1,\pm 2$. The peaks with $M\pm 1$ have type–I properties, while the peaks with $M\pm 2$ have type-II properties. The dependence of the heights of the peaks on the structure of the unit cell is given by the coefficients

$$S_M^t=\left|\sum_{s=1}^{N}\exp\left[i\frac{2\pi t}{N}s-iM\Psi_s\right]\right|^2. \tag{9}$$

The incommensurability δ is small and is omitted in Eq. (9). Much more important is the fact that it determines the fine structure of the peaks, which in the general case are split into four peaks.

Analyzing expression (9), it is easy to see that the existing experimental data, which do not give any information about the fine structure and polarization properties of the peaks, are inadequate to determine the structure of the unit cell, specifically, the set of angles Ψ_s. It is important only to eliminate certain types of cells, as happens with ''Ising'' structures with $N=4$, for which expression (9) gives either no peaks $Q=K+1/2$ (K is an arbitrary integer) or equal intensities of all resonant scattering peaks. Both contradict the experimental data obtained in Ref. 10.

It is clear that the study of the fine structure of the peaks together with polarization observations will give much additional information. As an example, we can consider the double splitting, observed in the experiment of Ref. 10, of the half peak in an AF phase with $N=2$. Since

$$S_{\pm 1}^{2K+1}=4\sin^2(\Psi_2/2),\quad S_{\pm 2}^{2K+1}=4\sin^2\Psi_2, \tag{10}$$

the presence of a doublet gives unambiguously $\Psi_s=\pi$. It is also possible to predict that the doublet belongs to type-I scattering.

Relation (3) holds for a pure SPM. Then the quantities (9) are different from zero only for $t=KN+M$, which gives the position of the peaks as

$$Q=K+\frac{M}{N}-M\frac{\delta}{2\pi N}. \tag{11}$$

For phases with $N=3$ this means double splitting of the peaks $Q=1/3,4/3,\ldots$ into type-I peaks with $M=1$ and type-II peaks with $M=-2$, while the peaks Q

$=2/3,5/3,\ldots$ decompose into doublets with $M=-1$ and $M=2$. If $N=4$, then there is not enough time for the peaks $Q=K\pm 1/4$ to split, while the peaks $Q=K+1/2$ decompose into doublets with $M=\pm 2$.

The interaction of a SPM with a long-pitch helicoid distorts the screw symmetry of the pure SPM. Comparing expressions (1) and (2), it is easy to see that $q_L \ll \delta q$. Therefore the rotation of the displacement vector **D** can be neglected in view of the incommensurability. To estimate the corresponding changes in the scattering pattern, we can consider the case of a weak displacement, in which case the relation (4) holds. On account of incommensurability, the unit cells are turned by different angles relative to the displacement, so that $\varphi_D=-t\delta$, if the first layer in the zeroth cell is oriented along **D**.

The corresponding changes in Ψ_s give rise to corrections to the susceptibility. A theoretical analysis shows that this correction leads to scattering peaks at the points (8), but this time with $M=\pm 1,\pm 2$, and ± 3. Moreover, here the peaks with $M=\pm 2$ are of type I, while the peaks with $M=\pm 1,\pm 3$ are of type II. The intensities of these peaks are low, since they are proportional to $(D/\Xi)^2$. Ultimately, a small distortion of an SPM results in slight changes in the polarization behavior of the scattering peaks. It is important that in structures with $N\geqslant 4$ such a distortion should lead to the appearance of new small type-II peaks, corresponding to $M=\pm 3$. Therefore measurements of the fine structure and polarization dependence of resonant x-ray scattering peaks should give new information about the details of short-pitch azimuthal order. Similar experiments in an external electric field would also by very useful.

The proposed semiphenomenological model explains the presence of diverse families of ferro-, antiferro-, and ferrielectric phases in new liquid-crystal materials. It differs from other models in several respects. Specifically, the conventional expansions of the inhomogeneous part of the free energy in powers of small wave numbers are unsuitable here because of the presence of SPMs in such liquid crystals, but expansions in the small incommensurability of the superlattices under discussion are physically justified. The main physical parameters controlling the families named are the chirality α and the smectic correlation length ξ. The existence of ferrielectric states could be due to both the above-mentioned incommensurability of the SPMs and the actual coexistence of SPMs and LWMs. Chirality, which determines the incommensurability of the SPMs, gives rise to splitting of the x-ray scattering peaks, the splitting being greater than that produced only by the twist structure of LWMs. Strong LWMs should give rise to strong orientational deformation of the unit cell, so that the cell could approximate an ''Ising'' cell, giving additional features in the distribution of the molecular density.

The observed[10] ''family'' (2, 3, 4) is one possible family in the model considered and corresponds to the choice $m=2$; $n=-2,3,-4$. The splitting of the x-ray peaks is $(\alpha/n)^2$ in order of magnitude and is maximum for the SPM with $n=-2$, i.e., for the mode with the shortest pitch. For large n the model predicts a smaller splitting and larger broadening of the peaks, the latter being due to the higher probability of observing SPMs with wave numbers of both signs.

We thank the Russian Fund for Fundamental Research for supporting this work (Grant No. 98-02-16802). We thank R. Pindak and V. Dmitrienko for a fruitful discussion of the experimental data and the theoretical aspects of the problem.

*e-mail: pikin@theory.incr.msk.ru

[1] A. Fukuda, Y. Takanishi, T. Isozaki *et al.*, J. Mater. Chem. **4**, 997 (1994).
[2] Y. Takanishi, K. Hiraoka, V. Agrawal *et al.*, Jpn. J. Appl. Phys., Part 1 **30**, 2023 (1991).
[3] T. Isozaki, T. Fujikawa, H. Takezoe *et al.*, Jpn. J. Appl. Phys., Part 1 **31**, 1435 (1992).
[4] K. Hiraoka, Y. Takanishi, K. Sharp *et al.*, Jpn. J. Appl. Phys., Part 1 **30**, L1819 (1991).
[5] H. Orihari and Y. Ishibashi, Jpn. J. Appl. Phys., Part 2 **29**, L115 (1990).
[6] B. Zeks and M. Cepic, Liq. Cryst. **14**, 445 (1993).
[7] V. L. Lorman, A. A. Bulbitch, and P. Toledano, Phys. Rev. E **49**, 1367 (1994).
[8] M. Cepic and B. Zeks, Mol. Cryst. Liq. Cryst. Sci. Technol., Sect. A **263**, 61 (1995).
[9] S. A. Pikin, S. Hiller, and W. Haase, Mol. Cryst. Liq. Cryst. Sci. Technol., Sect. A **262**, 425 (1995).
[10] P. Mach, R. Pindak, A.-M. Levelut *et al.*, Phys. Rev. Lett. **81**, 1015 (1998).
[11] V. E. Dmitrienko, Acta Crystallogr., Sect. A: Found. Crystallogr. **39**, 29 (1983).

Translated by M. E. Alferieff

Resonance energy transfer from a semiconductor quantum dot to an organic matrix

V. M. Agranovich*
Institute of Spectroscopy, Russian Academy of Sciences, 142092 Troitsk, Moscow Region, Russia

D. M. Basko
Institute of Spectroscopy, Russian Academy of Sciences, 142092 Troitsk, Moscow Region, Russia;
Scuola Normale Superiore, I-56126 Pisa, Italy

(Submitted 11 January 1999)
Pis'ma Zh. Éksp. Teor. Fiz. **69**, No. 3, 232–235 (10 February 1999)

A study is made of the Förster energy transfer from an excited semiconductor quantum dot to an organic material surrounding the dot. A quantum-mechanical microscopic description of a Wannier–Mott exciton in a quantum dot is employed together with a macroscopic description of the organic medium. The calculations show that for II–VI semiconductors such transfer can occur in a time of the order of tens of picoseconds, which is much shorter than the lifetime of an excitation in a quantum dot in the absence of transfer. Therefore, just as for quantum wells, the energy transfer mechanism considered can be a quite efficient means for pumping organic sources of radiation. © *1999 American Institute of Physics.* [S0021-3640(99)01503-0]

PACS numbers: 73.20.Dx, 61.46.+w

1. Hybrid nanostructures based on semiconductor and organic materials with close exciton energies[1] have been studied in various configurations, and it has been predicted that they should possess a number of advantages over the conventional, purely organic or purely inorganic, nanostructures.[1–6] These configurations can be divided into two groups. In the first case (strong coupling) the characteristic dipole–dipole resonance interaction energies of Wannier–Mott excitons (in a semiconductor) and Frenkel excitons (in an organic material) are greater than the widths of the corresponding levels. This leads to the appearance of elementary excitations of a new type, which are a coherent superposition of two types of excitons.[1–3,6] It has been shown that nonlinear optical effects should be greatly intensified in such systems.

In the second case (weak coupling) the level widths are much greater than the resonance interaction energy. This is characteristic for many organic materials. In this situation dephasing processes destroy the coherent superposition of excitonic states and incoherent energy transfer occurs from the subsystem where dissipative processes are slow (donor) to the subsystem where dissipation is rapid (acceptor). This corresponds to the Förster picture.[7] The case where the donor is the semiconductor part of the structure

and the acceptor is the organic part is currently of greatest interest. If the transfer time is shorter than or of the order of the lifetime of a Wannier–Mott exciton, then a large part of the energy can be transferred from the semiconductor to the organic material. This will make it possible to combine the comparatively good transport characteristics of semiconductors (pumping them, for example, electrically) with the high light-emission capability characteristic of organic materials. Calculations performed for a planar geometry (semiconductor quantum well coated with a layer of an organic acceptor)[4,5] have shown that such energy transfer can indeed be quite efficient.

One type of semiconductor nanostructures which have been actively studied in the last few years are quantum dots (see Ref. 8 and the literature cited therein). In the present letter we shall analyze Förster energy transfer from a quantum dot to organic material surrounding the dot. For simplicity, we consider a spherical quantum dot and we employ the effective-mass approximation to describe the Wannier–Mott exciton. For the organic subsystem a macroscopic description where a permittivity is introduced is completely satisfactory, since in an organic material the characteristic distances over which fields vary are much larger than the intermolecular distances.

2. The subsequent analysis was performed for a nanostructure where a spherical quantum dot with radius R_1 and permittivity ε is surrounded by a concentric semiconductor barrier with outer radius R_2 and the same permittivity, while the material outside the barrier is surrounded by organic material with permittivity $\tilde{\varepsilon}$. The permittivity ε includes only the contribution from higher resonances with respect to the excitonic resonance under study, and we assume that ε is real. The permittivity $\tilde{\varepsilon}$, however, is the total permittivity of the organic material and is substantially complex.

The general scheme for calculating the rate of Förster energy transfer in a hybrid nanostructure is described in detail in Refs. 4 and 5. In our case this transfer rate can be found by calculating the Joule losses of the electric field that is produced by the excitonic polarization of a quantum dot in an organic medium.

Let an exciton with energy $\hbar\omega$ be described by the envelope of the wave function $\psi(\mathbf{r}_e, \mathbf{r}_h)$, and let $\mathbf{d}^{vc}$ be the matrix element of the electric dipole moment between Bloch functions of the valence band and the conduction band. The matrix element of excitonic polarization in the quantum dot is

$$\mathbf{P}(\mathbf{r}) = \mathbf{d}^{vc}\,\psi(\mathbf{r},\mathbf{r}). \tag{1}$$

The electric field $\mathcal{E}(\mathbf{r})$ corresponding to this polarization can be found from the Poisson equation for the potential $\phi(\mathbf{r})$:

$$\varepsilon(r)\,\nabla^2\phi(\mathbf{r}) = 4\pi\,\boldsymbol{\nabla}\cdot\mathbf{P}(\mathbf{r}), \tag{2}$$

where $\varepsilon(r)=\varepsilon$ for $r<R_2$ and $\varepsilon(r)=\tilde{\varepsilon}$ for $r>R_2$, with appropriate boundary conditions at $r=R_2$. Knowing the electric field, we can calculate the power dissipated in the organic material (Joule losses):[9]

$$W = \frac{\omega\,\mathrm{Im}\,\tilde{\varepsilon}(\omega)}{2\pi}\int_{r>R_2} |\mathcal{E}(\mathbf{r})|^2\,d^3\mathbf{r}. \tag{3}$$

Hence we find that the rate of energy transfer (the reciprocal of the transfer time) is given by the expression

$$\frac{1}{\tau}=\frac{W}{\hbar\omega}=\frac{\operatorname{Im}\tilde{\varepsilon}(\omega)}{2\pi\hbar}\int_{r>R_2}|\mathcal{E}(\mathbf{r})|^2\,d^3\mathbf{r}. \tag{4}$$

3. In our spherical geometry the states of an electron–hole pair can be classified according to the values of the total angular momentum of the electron and hole. We shall assume that the electron–hole pair occupies the lowest excited state. In this state the total angular momentum is zero, and therefore the function $\psi(\mathbf{r},\mathbf{r})$ is spherically symmetric and $\mathbf{P}(\mathbf{r})=\mathbf{P}(r)$. Orienting the z axis parallel to the vector $\mathbf{d}^{vc}$, we obtain for the charge density

$$\rho(\mathbf{r})=-\boldsymbol{\nabla}\cdot\mathbf{P}(r)=-\frac{\partial P(r)}{\partial z}=\rho^{(r)}(r)\,Y_{10}(\theta). \tag{5}$$

Here $Y_{10}(\theta)\propto\cos\theta$ is the spherical harmonic with $l=1$ and $m=0$ that is obtained when a spherically symmetric function is differentiated with respect to z. Expanding the potential $\phi(\mathbf{r})$ in the organic material, where there are no charges, in terms of multipoles,[10] we see that only the dipole term, which is proportional to $Y_{10}(\theta)$, will be different from zero. Therefore the potential $\phi(\mathbf{r})$ in the organic medium is formally identical to the potential of an effective point dipole with dipole moment $\mathbf{p}^{\text{eff}}$:

$$\phi(\mathbf{r})=(\mathbf{p}^{\text{eff}}\cdot\mathbf{r})/\tilde{\varepsilon}\,r^3. \tag{6}$$

Calculations similar to those in, for example, Ref. 7 (Chapter 1) show that

$$p^{\text{eff}}=\frac{3\tilde{\varepsilon}}{\varepsilon+2\tilde{\varepsilon}}\int_0^{R_2}P(r)\,4\pi r^2\,dr. \tag{7}$$

Substituting the field of the dipole into Eq. (4) we obtain

$$\frac{1}{\tau}=\frac{\operatorname{Im}\tilde{\varepsilon}}{2\pi\hbar}\int_{r>R_2}|\mathcal{E}(\mathbf{r})|^2\,d^3\mathbf{r}=\frac{1}{\hbar}\,\frac{4\operatorname{Im}\tilde{\varepsilon}}{3\tilde{\varepsilon}^2R_2^3}|p^{\text{eff}}|^2. \tag{8}$$

4. The wave function $\psi(\mathbf{r}_e,\mathbf{r}_h)$ of an exciton is determined by two interactions: (i) the electron and hole confinement potential, which we shall assume to be infinite for $r>R_1$ and zero for $r<R_1$ and (ii) the electron–hole Coulomb attraction. These interactions correspond to the following characteristic lengths: R_1 — the radius of the quantum dot and a_B — the Bohr radius of an exciton in a macroscopic three-dimensional semiconductor. The problem of solving the two-particle Schrödinger equation for an arbitrary ratio of R_1 and a_B is quite difficult (see, for example, Ref. 11), but the situation simplifies substantially in two limiting cases.

If $R_1\gg a_B$ (weak confinement), the splitting between the levels in a spherical well is much smaller than the binding energy of a three-dimensional Wannier–Mott exciton. In this case the latter can be assumed to be a rigid particle moving in a spherical well. The variables corresponding to the relative motion of an electron and a hole and the motion of the center of the mass effectively separate, and the wave function factorizes. Then

$$\psi(\mathbf{r},\mathbf{r})=\frac{1}{\sqrt{\pi a_B^3}}\chi_0(\mathbf{r}),\quad \chi_0(\mathbf{r})\equiv\frac{1}{\sqrt{2\pi R_1}}\,\frac{\sin(\pi r/R_1)}{r}. \tag{9}$$

The corresponding dipole moment is

$$p^{\text{eff}}=\frac{1}{\pi}\left(\frac{2R_1}{a_B}\right)^{3/2}\frac{3\tilde{\varepsilon}\,d^{vc}}{\varepsilon+2\tilde{\varepsilon}}. \tag{10}$$

If, however, $R_1 \ll a_B$ (strong confinement), then the Coulomb interaction can be completely neglected, and the wave function of the exciton will be simply the product of two (identical) single-particle electron and hole functions:

$$\psi(\mathbf{r}_e,\mathbf{r}_h)=\chi_0(\mathbf{r}_e)\,\chi_0(\mathbf{r}_h), \tag{11}$$

and the corresponding dipole moment will be

$$p^{\text{eff}}=3\tilde{\varepsilon}\,d^{vc}/(\varepsilon+2\tilde{\varepsilon}). \tag{12}$$

The energy transfer rates in the limiting cases indicated above are

$$\frac{1}{\tau_1}=\frac{96\,\mathrm{Im}\,\tilde{\varepsilon}}{\pi^2|\varepsilon+2\tilde{\varepsilon}|^2}\frac{1}{\hbar}\frac{|d^{vc}|^2}{a_B^3}\left(\frac{R_1}{R_2}\right)^3 (R_1 \gg a_B), \quad \frac{1}{\tau_2}=\frac{12\,\mathrm{Im}\,\tilde{\varepsilon}}{|\varepsilon+2\tilde{\varepsilon}|^2}\frac{1}{\hbar}\frac{|d^{vc}|^2}{R_2^3}\ (R_1 \ll a_B). \tag{13}$$

To obtain a numerical estimate we shall employ the typical parameter values for the elements of II–VI compounds (for example, ZnSe)[12] and organic substances used in similar experiments:[13] $a_B \simeq 50$ Å, $d^{vc} \simeq 12$ D, $\varepsilon \simeq 6$, and $\tilde{\varepsilon} \simeq 4+3i$. For $R_2=1.5R_1$ these parameters give a transfer time $\tau_1 \simeq 20$ ps, and the time τ_2 is even shorter. This estimate shows that the energy transfer time is much shorter than the exciton lifetime (hundreds of picoseconds in II–VI semiconductors) determined by all the other processes in a quantum dot.

In summary, the energy transfer mechanism considered above, just as in the case of quantum wells,[4,5] is quite rapid and makes possible the transfer of a substantial part of the energy from a semiconductor quantum dot to the organic molecules surrounding the dot, with possible subsequent deexcitation of the dot. The possibility of using electrical pumping of quantum dots (see, for example, Ref. 14 and the literature cited therein) makes this energy transfer mechanism interesting for applications as well.

This work was supported by Grant No. 97-1074 of the Ministry of Science of the Russian Federation Program ''Physics of Solid-State Nanostructures.''

*e-mail: agran@isan.troitsk.ru

[1] V. M. Agranovich, R. Atanasov, and F. Bassani, Solid State Commun. **92**, 295 (1994).
[2] V. I. Yudson, P. Reineker, and V. M. Agranovich, Phys. Rev. B **52**, R5543 (1995).
[3] A. Engelmann, V. I. Yudson, and P. Reineker, Phys. Rev. B **57**, 1784 (1998).
[4] V. M. Agranovich, G. C. La Rocca, and F. Bassani, JETP Lett. **66**, 748 (1997).
[5] D. M. Basko, G. C. La Rocca, F. Bassani, and V. M. Agranovich, Eur. Phys. J. B (1999), in press.
[6] V. M. Agranovich, D. M. Basko, G. C. La Rocca, and F. Bassani, J. Phys.: Condens. Matter **10**, 9369 (1998).
[7] V. M. Agranovich, and M. D. Galanin, *Electronic Excitation Energy Transfer in Condensed Matter*, North-Holland, Amsterdam, 1982.
[8] U. Woggon and S. V. Gaponenko, Phys. Status Solidi B **189**, 285 (1995).
[9] L. D. Landau and E. M. Lifshitz, *Electrodynamics of Continuous Media*, 2nd ed., rev. and enl., by E. M. Lifshitz and L. P. Pitaevskii, Pergamon Press, Oxford, 1984 [Russian original, Nauka, Moscow, 1982].
[10] L. D. Landau and E. M. Lifshitz, *The Classical Theory of Fields*, Pergamon Press, New York [Russian original, Nauka, Moscow, 1988].
[11] Y. Z. Hu, M. Lindberg, and S. W. Koch, Phys. Rev. B **42**, 1713 (1990).

[12] R. Cingolani, in *Semiconductors and Semimetals,* Academic Press, 1997, Vol. 44, p. 163.
[13] S. R. Forrest, Chem. Rev. **97**, 1793 (1997).
[14] L. V. Asryan and R. A. Suris, IEEE J. Quantum Electron. **34**, 841 (1998).

Translated by M. E. Alferieff

Suppression of the equilibrium tunneling current between slightly disordered two-dimensional electron systems with different electron concentrations in a high magnetic field

Yu. V. Dubrovskii, E. E. Vdovin, Yu. N. Khanin, and V. G. Popov
Institute of Microelectronics Technology, Russian Academy of Sciences, 142432 Chernogolovka, Moscow Region, Russia

D. K. Maude and J.-C. Portal
Grenoble High Magnetic Field Laboratory, MPI-CNRS, 38042 Grenoble, France

J. K. Maan
High Field Magnet Laboratory, University of Nijmegen, 6525 ED Nijmegen, The Netherlands

T. G. Andersson and S. Wang
Chalmers University of Technology and Göteborg University, Department of Physics, S-412 96 Göteborg, Sweden

(Submitted 8 December 1998; resubmitted 14 January 1999)
Pis'ma Zh. Éksp. Teor. Fiz. **69**, No. 3, 236–241 (10 February 1999)

Tunneling between parallel two-dimensional electron gases (2DEG) in accumulation layers formed on both sides of the single doped AlGaAs barrier are examined in both zero and high magnetic field. Accumulation layers are separated from highly *n*-doped contact regions which freely supply electrons to the 2DEGs via 80 nm thick lightly *n*-doped spacer layers. Strongly oscillating current with magnetic field along the 2DEGs is absent in this arrangement. Without magnetic field resonant tunneling between 2DEGs with different as grown electron concentration could be settle by application of external voltage bias. High magnetic fields ($\nu<1$) shift resonant tunneling to zero external bias and suppresses tunneling current, creating wide gap in the tunneling density of states at the Fermi level arisen from the in-plane Coulomb interaction in the 2DEGs. © *1999 American Institute of Physics.* [S0021-3640(99)01603-5]

PACS numbers: 71.10.Ca, 73.50.Jt

It has been found during the last decade[1–7] that both resonant and many-body effects play essential roles in tunneling between parallel two-dimensional electron gases (2DEGs). The resonant tunneling between different two-dimensional (2D) subbands as well as inter- and intra-Landau-level tunneling in a magnetic field normal to the 2D plane have been thoroughly investigated in an earlier work.[1] It has been shown[2] that an in-plane magnetic field also strongly influences the resonant tunneling between two 2DEGs, as it

requires the conservation of both energy and in-plane momentum. The so-called Coulomb gap induced in the tunneling density of states by a magnetic field has been observed for equilibrium tunneling between 2D electron systems[3–6] as the suppression of the tunneling current by a magnetic field and has given rise to intensive theoretical discussions.[8–10] There is general agreement that the observed suppression is related to the in-plane Coulomb correlation between 2D electrons in a high magnetic field. Another manifestation of the Coulomb correlation has been found in double-barrier resonant tunneling devices[7] as a shift of the resonance current peak to higher bias voltage in a magnetic field. In spite of the large number of works there are still some contradictions even between the experimental findings of the different groups, and it seems that the current understanding of the phenomena is far from clear.

In this letter we present results of tunneling current measurements on single doped barrier GaAs/AlGaAs/GaAs heterostructures at liquid helium temperatures and in magnetic fields up to 23 T. In this kind of structures two-dimensional electron accumulation layers are formed on both sides of the barrier due to its donor doping and are separated from highly *n*-doped contact regions by lightly *n*-doped or undoped spacer layers.[1,11] At first glance our sample resembles a system in which two sequential 2D electrons planes are inserted between three-dimensional contact layers with a generally unknown potential distribution along the current flow under external bias. To avoid this problem it is necessary to design the structure in such a way that the external voltage will drop mainly across the (AlGa)As barrier. It gives one a sample where 2D and 3D systems are in thermodynamic equilibrium on each side of the barrier, with a free supply of electrons to the 2DEG accumulation layer from the parallel planar contact layer under arbitrary external bias. By thorough capacitance–voltage measurements on samples prepared from a number of wafers with different growth parameters, we selected a structure which satisfied the condition of thermodynamics equilibrium between the 2D accumulation layer and the highly doped contact region. The main criterion for this selection was that the capacitance be independent of the applied bias and be approximately equal to the geometrical capacitance of the barrier. In this letter we present only results obtained on the selected samples and actually related with tunneling between 2D electron systems. The arrangement of the structure used essentially distinguishes our measurements from previous papers[1,3–6] in which strongly oscillating currents along the 2DEGs in the magnetic field were not excluded from the experimental arrangement. Without a magnetic field the resonant tunneling between 2DEGs with different as-grown concentrations could be settled by application of an external bias voltage. We have found that high magnetic fields ($\nu<1$) shifts the resonant tunneling to zero external bias due to the pinning of the last Landau level in each 2DEG by the contact-layer chemical potential. This prompts us to study the magnetic-field suppression of the equilibrium tunneling between 2DEGs in a purely vertical arrangement (no current along 2DEGs) and compare our results with recent experimental observations of the magnetic-field-induced Coulomb gap in the tunneling density of states.[4,5,7] We have found a linear dependence of the gap parameters on magnetic field, in agreement with findings of Ref. 5, which are in contradiction to the results of Refs. 4 and 7, where a significantly weaker dependence of the gap width on magnetic field was found.

The samples were grown by molecular beam epitaxy (MBE) on a (100)-oriented Si-doped n^+-type GaAs wafer ($N_d=2\times10^{18}$ cm^{-3}). The structure consists (in order of

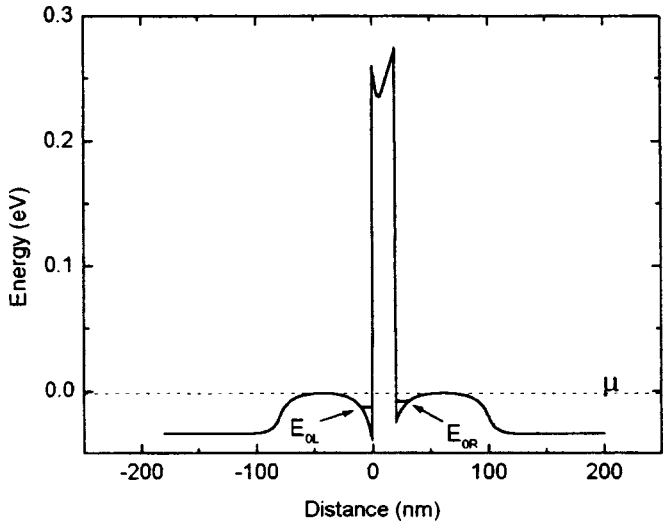

FIG. 1. Schematic band diagram of the structure under zero bias. E_{0L} and E_{0R} define the ground states of the 2D accumulation layers, and μ is the chemical potential along the structure under equilibrium conditions.

growth) of a Si-doped, 50-nm-thick GaAs layer ($N_d=5\times10^{17}$ cm^{-3}); a 70-nm-thick lightly doped GaAs layer ($N_d=2\times10^{15}$ cm^{-3}); a 10-nm-thick layer of undoped GaAs; a 5-nm-thick $Al_{0.3}Ga_{0.7}As$ undoped barrier layer; a 10-nm-thick Si-doped $Al_{0.3}Ga_{0.7}As$ barrier layer ($N_d=6\times10^{17}$ cm^{-3}); a 5-nm-thick $Al_{0.3}Ga_{0.7}As$ undoped barrier layer; a 10-nm thick undoped GaAs layer; a 70-nm-thick lightly doped GaAs layer ($N_d=2\times10^{15}$ cm^{-3}); a 50-nm-thick GaAs layer ($N_d=5\times10^{17}$ cm^{-3}); a Si-doped, 50-nm-thick GaAs layer ($N_d=5\times10^{17}$ cm^{-3}); and a GaAs cap layer ($N_d=1.5\times10^{18}$ cm^{-3}), which was 300 nm thick. To fabricate Ohmic contacts an AuGe/Ni/Au metallic film was evaporated on the n^+-type GaAs cap layer. Mesa structures (100 μm in diameter) were defined by wet etching (2 μm depth) using a metal mask. A second Ohmic contact was prepared on the back side of the wafer by In soldering. A standard annealing process (400 °C, 2 min in a N_2 atmosphere) produced good Ohmic contacts (10^{-6}–$10^{-5}\Omega\cdot$cm^{-2}). A schematic band diagram of the structure under zero bias is shown in Fig. 1.

The current–voltage (I–V) characteristic of this structure demonstrates negative differential conductance (NDC) (indicated by arrow ''a'' on Fig. 2) at negative bias without a magnetic field and some features at positive bias (arrow ''b'' on the same figure) at 4.5 K. We argue that, as in Ref. 1, the current peak followed by a NDC region is due to resonance between the ground states of the 2DEGs (0–0 transition) and that the rapid increase in the current at around 12 mV of positive applied bias is due to resonance between the ground state of one 2DEG and the first excited state of the other one (0–1 transition). The accumulation layers have different as-grown electron concentrations.

We estimated the 2D electron concentrations and the electron mobility in the layers from the measured I–V curves and the Shubnikov–de Haas-like oscillations of the tunnel current with magnetic field. For this estimation we used the procedure described in Ref. 6 and found the 2D electron concentrations $N_{2D-1}\approx3\times10^{11}$ cm^{-2} and $N_{2D-2}\approx1.8\times10^{11}$ cm^{-2}, and the estimated mobility is about 40 000 cm^{2}V^{-1}s^{-1}.

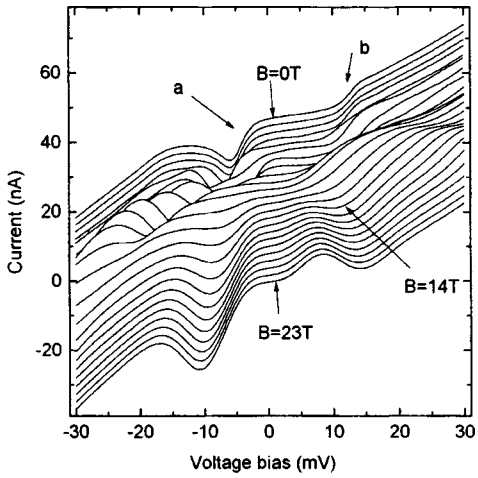

FIG. 2. Current–voltage characteristics in the absence of magnetic field and and in different magnetic fields up to 23 T. The magnetic field step between the curves is 1 T. All the curves except the 23 T curve are shifted vertically for clarity. Arrows ''a'' and ''b'' indicate features on the I–V curve in the absence of magnetic field (see text for details).

Figure 2 shows how the I–V curves are transformed in a magnetic field parallel to the current. For fields smaller than 12 T the curves have quite complicated forms which can be described in principle with an interplay of the resonance tunneling between different Landau levels, taking into account also the existence of two-dimensional subbands with higher indices and the self-consistent redistribution of the electrons between accumulation layers as the density of states is modulated by the magnetic field.

In this letter we concentrate on a discussion of the behavior of the I–V curves in magnetic fields greater than 14 T, leaving the discussion of the lower magnetic field range to a future publication.

In a magnetic field parallel to the current greater than 14 T ($\nu<1$) the I–V characteristics are drastically changed (Fig. 2). Now the NDC appears at both voltage polarities. We assign this behavior to the magnetic-field-induced resonance at zero voltage. Indeed, when only one Landau level is occupied in both electron layers the Fermi level in the contact regions pin the Landau levels, and both 2DEGs, in spite of the different electron concentrations, are brought into tunneling resonance. We note that no spin splitting has been observed in our structures. The I–V characteristics in a magnetic field with the current suppressed around zero bias are similar to those which were observed in Refs. 3 and 5 but are asymmetrical. The suppression is more obvious from Fig. 3a, which shows the I–V curves for 4.2 K and 10 K in a magnetic field $B=20$ T. For comparison, Fig. 3b shows part of the same curves in the absence of magnetic field; this clearly demonstrates that the influence of temperature on the simple resonant tunneling between 2DEGs is very small. Previously[3] the current suppression around zero bias and the wide current peaks at higher biases were interpreted as a manifestation of a gap in the tunneling density of states, with broadened final states around the gap.

To characterize the gap in our experiments we chose the positions of current peaks and differential conductance maxima on the voltage scale as the gap parameters. Figure

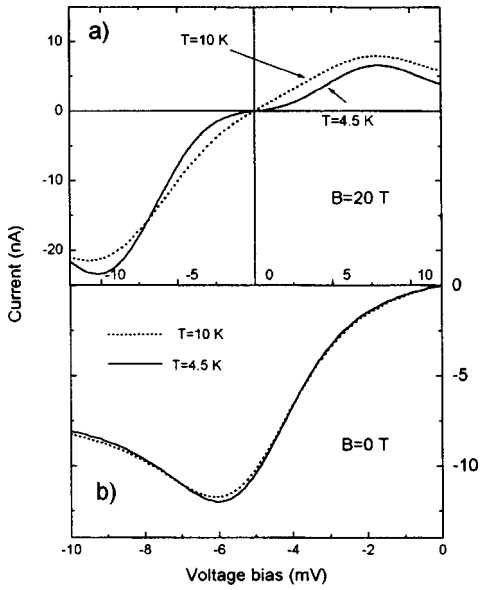

FIG. 3. a: Current–voltage characteristics in a magnetic field of 20 T for different temperatures: 4.2 K – solid line, 10 K – dotted line; b: the same in the absence of magnetic field.

4 shows that all of these parameters have linear dependence on magnetic field, and from these dependences the dependence of the gap on magnetic field could be described as $\Delta/2 \approx (0.14 \pm 0.02)\hbar\omega_c$, where $\hbar\omega_c = \hbar eB/m^*$ is the cyclotron energy. We also used

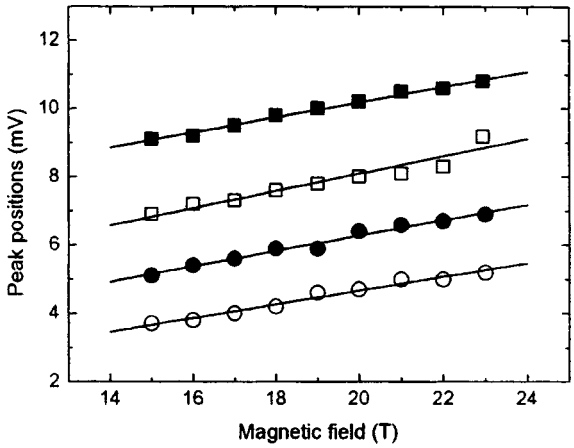

FIG. 4. Position on the voltage scale of the current peaks and differential conductance maxima as a function of magnetic field. Squares represent the positions of the current peaks, and circles are used for the positions of the differential conductance maxima. The filled squares and circles are for negative bias, the unfilled for positive bias. The averaged dependence of all the data on magnetic field is $\sim(0.14 \pm 0.2)\hbar\omega_c$. The straigt lines are shown only as a guide for the eye.

10% onsets of the current to estimate the gap width. It is a few mV for both positive and negative bias and is the same order of magnitude as the Coulomb interaction energy in the 2D layers.

Before comparing our results with the findings of the previous studies[3–7] it is worthwhile to make some prefatory remarks. The cause of the appearance of the gap in the tunneling density of states (DOS) is as follows. In a strong magnetic field normal to the 2D plane, when the Landau level filling factor $\nu = hn/eB$ is less than unity, it is assumed that an electron traverses the tunnel barrier between the 2DEGs in a much shorter time scale than that for the rearrangement of the charges around the injected electron (or around the hole left behind in the emitter layer). The energies of the injection and extraction processes create a gap in the tunneling DOS. Many-body theories predict[8] that for a fixed filling factor $\nu < 1$ the width of the energy gap is approximately $0.4e^2/4\pi\varepsilon l_B$ (where $l_B = \sqrt{\hbar/eB}$ is the magnetic length), or, if the electron liquid forms a regular lattice,[9] the gap energy in the classical limit is $e^2/4\pi\varepsilon a$ (where $a = \sqrt{n\pi}$ is the interelectron spacing within the layer). At a fixed filling factor both predicted forms for the gap have the same $\sqrt{B}$ dependence on the magnetic field.

Eisenstein and co-workers[4] argued from tunneling measurements on samples with different barrier widths that the high-field gap energy is mainly determined by the in-plane Coulomb interaction, modified by an interlayer excitonic binding energy. The form of the gap used to fit their data was $\Delta_E = f(\nu)\ e^2/4\pi\varepsilon a - 0.4e^2/4\pi\varepsilon d$, where $f(\nu)$ is some universal function of the filling factor, and d is the quantum well center-to-center separation.

Contrary to the findings of Eisenstein *et al.*[3,4] and the predictions of existing theories,[8,9] Brown *et al.*[5] found a linear magnetic-field dependence of the gap, $\Delta \approx 0.44\hbar\omega_c$, which was observed both at fixed filling factors and at constant carrier density. They measured gaps of comparable energy in samples with a lower mobility but otherwise similar to those used by Eisenstein *et al.* — GaAs/AlGaAs double-layer structures with additional gates to permit independent control of the electron concentration in the layers. In addition, at a fixed magnetic field of 16 T they did not observe noticeable changes in the measured I–V curves when the electron concentrations in the layers were varied from 1 to 3×10^{11} cm^{-2} (see Fig. 3 in Ref. 5).

Lok *et al.*,[7] by measurements on different (AlGa)As double-barrier resonant tunneling devices, found that at $T = 0$ the additional energy Δ_L required for resonant tunneling in high magnetic fields increases with increasing electron concentration n in the 2DEG of the emitter from 0.7 to 3.0×10^{11} cm^{-2} and can be described by a dependence $\Delta_L = \beta e^2/a \sim n^{1/2}$ ($\beta \approx 0.6$–0.8). An additional magnetic-field dependence of the energy Δ_L for a single device exhibited saturation for $\nu < 1$. The results at least qualitatively agree with those obtained by Eisenstein *et al.*[4] but contradict the findings of Brown *et al.*[5]

Our samples have a serious restriction since we were not able to change the electron concentration in the accumulation layers. Nevertheless, Brown *et al.* mentioned in their paper[5] that the same results as for equal concentration were obtained in measurements of the magnetic-field-induced suppression for different electron concentrations in the layers. This allows us to compare our results at least with the findings of Brown *et al.*

Our results imply a linear dependence of the gap on magnetic field, $\Delta \approx 0.28\hbar\omega_c$, which is similar to the result $\Delta \approx 0.44\hbar\omega_c$ given in the paper of Brown *et al.*[5] The

tunneling gap found by Eisenstein *et al.*,[4] on account of the prefactor $f(\nu)$, also depends on the magnetic field at a constant electron concentration. However, as can be seen from Fig. 1 of Ref. 3, this dependence is weak and does not exceed $\Delta \approx 0.03\hbar\omega_c$. The main difference between the Eisenstein and Brown samples is the difference in the quality of the 2DEGs. In the Eisenstein experiments the 2DEGs had $\mu \sim 3\times 10^6$ cm^2 V^{-1} s^{-1}, whereas in the Brown experiments the mobilities were only $\mu \sim 10^5$ cm^2 V^{-1} s^{-1}. In our samples the mobility in the layers was $\mu \sim 4\times 10^4$ cm^2 V^{-1} s^{-1}. It is difficult to judge about the 2DEG mobility in the resonant tunneling devices of Ref. 7, but it should be noted that tunneling gap induced by the magnetic field was investigated in that study under far from equilibrium conditions. The magnitude of the gap in all experiments is of the order of the Coulomb interaction energy in the layers.

From the above comparison it could be supposed that microscopic inhomogeneities and disorder not only determine the mobility in the 2DEG but also influence the magnetic-field-induced gap formation in the tunneling density of states, giving rise to a different dependence of the gap on magnetic field in comparison with the case of high-quality two-dimensional electron systems. As far as we know this influence has not yet been considered theoretically.

Thus we have for the first time investigated the equilibrium tunneling between 2DEGs in a high magnetic field in a structure with purely vertical transport. A high magnetic field induced resonant tunneling between 2DEGs with different electron concentration at zero external voltage bias via pinning of the last Landau levels by the Fermi levels in the contact regions. This gave us an opportunity to investigate and compare our data concerning suppression of the tunneling current by a high magnetic field near zero bias with the results of previous studies.

This work was supported in part by the National program ''Physics of Solid-State Nanostructures'' (Grant 97-1057), PICS-CNRS (Grant 628), INTAS-RFBR (95-849), RFBR (98-17462, 98-22008), and CRDF (RP1-220).

[1] W. Demmerle, J. Smoliner, G. Berthold *et al.*, Phys. Rev. B **44**, 3090 (1991).
[2] G. Rainer, J. Smoliner, E. Gornik *et al.*, Phys. Rev. B **51**, 17642 (1995).
[3] J. P. Eisenstein, L. N. Pfeiffer, and K. W. West, Phys. Rev. Lett. **69**, 3804 (1992).
[4] J. P. Eisenstein, L. N. Pfeiffer, and K. W. West, Phys. Rev. Lett. **74**, 1419 (1995).
[5] K. M. Brown, N. Turner, J. T. Nicholls *et al.*, Phys. Rev. B **50**, 15465 (1994).
[6] N. Turner, J. T. Nicholls, E. H. Linfield *et al.*, Phys. Rev. B **54**, 10614 (1996).
[7] J. G. S. Lok, A. K. Geim, J. C. Maan *et al.*, Phys. Rev. B **56**, 1053 (1997).
[8] S. He, P. M. Platzman, and B. I. Halperin, Phys. Rev. Lett. **71**, 777 (1993); S.-R. E. Yang and A. H. MacDonald, Phys. Rev. Lett. **70**, 4110 (1993); Y. Hatsugai, P.-A. Bares, and X. G. Wen, Phys. Rev. Lett. **71**, 424 (1993).
[9] P. Johanson and J. M. Kinaret, Phys. Rev. Lett. **71**, 1435 (1993).
[10] F. G. Pikus and A. L. Efros, Phys. Rev. Lett. **73**, 3014 (1994); C. M. Varma, A. I. Larkin, and E. Abrahams, Phys. Rev. B **49**, 13999 (1994); P. Johansson and J. M. Kinaret, Phys. Rev. B **50**, 4671 (1994); S. R. Renn and B. W. Roberts, Phys. Rev. B **50**, 7626 (1994); M. E. Raikh and T. V. Shahbazyan, Phys. Rev. B **51**, 9682 (1995); I. L. Aleiner, H. U. Baranger, and L. I. Glazman, Phys. Rev. Lett. **74**, 3435 (1995).
[11] V. G. Popov, Yu. V. Dubrovskii, Yu. N. Khanin *et al.*, Fiz. Tekh. Poluprovodn. **32**, 602 (1998).

Published in English in the original Russian journal. Edited by Steve Torstveit.

Surface electron scattering in *d*-wave superconductors

A. A. Golubov
Department of Applied Physics, University of Twente, 7500 AE Enschede, The Netherlands

M. Yu. Kupriyanov
Nuclear Physics Institute, Moscow State University, 119899 Moscow, Russia

(Submitted 14 January 1999)
Pis'ma Zh. Éksp. Teor. Fiz. **69**, No. 3, 242–246 (10 February 1999)

A theoretical model of a rough surface in a *d*-wave superconductor is studied for the general case of arbitrary strength of electron scattering by an impurity layer covering the surface. Boundary conditions for quasiclassical Eilenberger equations are derived at the interface between the impurity layer and the *d*-wave superconductor. The model is applied to the self-consistent calculation of the surface density of states and the critical current in *d*-wave Josephson junctions. © *1999 American Institute of Physics.* [S0021-3640(99)01703-X]

PACS numbers: 74.80.Dm, 73.25.+i

Understanding the transport properties of surfaces and interfaces in high-temperature superconductors (HTS) is important for correct interpretation of experimental data and for applications of these materials. Up to now surface peculiarities in *d*-wave superconductors were extensively discussed in the framework of theoretical models based on quasiparticle reflection from specular interfaces.[1–4] The influence of surface roughness in this approach was studied by the Ovchinnikov method,[5] namely, by introducing a thin impurity layer covering the surface.[3–6] The degree of roughness is then measured by the ratio of the layer thickness d to the quasiparticle mean free path ℓ in the layer. This approach was used to study the smearing of Andreev surface bound states by weak disorder ($d \ll \ell$).

The regime of strong surface roughness, $d \gg \ell$, was discussed in Ref. 7. In this case parameter-free boundary conditions were derived at the interface between the superconductor and the disordered layer. Similar conditions were also derived earlier in Ref. 8 at rough walls in superfluid ^{3}He-B. As was shown in Ref. 7, an isotropic order parameter is nucleated in the disordered layer even in the absence of the bulk subdominant pairing interaction in the *s*-wave channel. This leads to the formation of the gapless *s* state at the interface. This phenomenon was called an anomalous proximity effect between a *d*-wave superconductor and a disordered layer.

In the present paper we consider the anomalous proximity effect between a *d*-wave superconductor and a surface impurity layer of thickness $d \ll \min\{\sqrt{\xi_0 \ell},\ \xi_0\}$ in the general case of an arbitrary electronic mean free path ℓ.

We consider the interface oriented normally to the crystallographic *ab* plane and assume elastic Born scattering. The normal and anomalous quasiclassical propagators, g and f, depend on the coordinate x in the direction of the surface normal and on the angle θ between the surface normal and quasiparticle trajectory and obey the quasiclassical Eilenberger equations.[9] Using the substitutions[10]

$$f=\frac{2a}{1+ab}, \qquad f^{+}=\frac{2b}{1+ab}, \qquad g=\frac{1-ab}{1+ab}, \tag{1}$$

we rewrite these equations in terms of the scalar differential equations of the Ricatti type

$$v\cos\theta\frac{db(x)}{dx}-\left[2\omega_n+\frac{1}{\tau}\langle g\rangle+b(x)\left(\Delta(x)+\frac{1}{2\tau}\langle f^{+}\rangle\right)\right]b(x)=-\Delta(x)-\frac{1}{2\tau}\langle f^{+}\rangle, \tag{2}$$

$$v\cos\theta\frac{da(x)}{dx}+\left[2\omega_n+\frac{1}{\tau}\langle g\rangle+a(x)\left(\Delta(x)+\frac{1}{2\tau}\langle f\rangle\right)\right]a(x)=\Delta(x)+\frac{1}{2\tau}\langle f\rangle. \tag{3}$$

The pair potential Δ should be found from the self-consistency equation

$$\Delta\ln\frac{T}{T_c}+2\pi T\sum_{\omega>0}\left(\frac{\Delta}{\omega}-\langle\lambda(\theta,\theta')f\rangle\right)=0. \tag{4}$$

Here $\omega_n=\pi T(2n+1)$ are the Matsubara frequencies, v is the Fermi velocity, and $\tau=\ell/v$. Assuming a cylindrical Fermi surface, we define the angle averages as $\langle\ldots\rangle=(1/2\pi)\int_0^{2\pi}(\ldots)d\theta$.

We consider a pure d-wave interaction in the bulk, with the coupling constant[11]

$$\lambda(\theta,\theta')\equiv\lambda_d(\theta,\theta')=2\lambda\cos(2(\theta-\alpha))\cos(2(\theta'-\alpha)),$$

where α is the misorientation angle between the crystallographic a axis and the surface normal. In this case the bulk anomalous propagator has the d-wave symmetry

$$b(+\infty,\theta)=a(+\infty,\pi+\theta)=\frac{\sqrt{2}\Delta_\infty\cos(2(\theta-\alpha))}{\omega+\sqrt{\omega^2+2\Delta_\infty^2\cos^2(2(\theta-\alpha))}}. \tag{5}$$

As will be shown below, this symmetry is broken near the interface.

Equations (2)–(4) must be supplemented with the boundary conditions connecting functions $b(0,\theta)$ and $a(0,\theta)$, which describe respectively the electrons incident and reflected from the interface. This can be done by matching the solutions in the impurity layer $(-d<x<0)$ and in the clean d-wave region $(0<x)$.

Since the thickness of the impurity layer $d\ll\xi_{eff}=\min\{\sqrt{\xi_0\ell},\ \xi_0\}$, we can neglect the terms proportional to ω and Δ in (2) and (3) and consider $\langle f\rangle$ and $\langle g\rangle$ as spatially-independent constants, which must be determined self-consistently. Making use of the boundary condition[12] at the totally reflecting free specular interface $(x=-d)$

$$b(-d,-\theta)=a(-d,\theta), \tag{6}$$

we find the solution of the equations (2), (3) at $-d\leqslant x\leqslant 0$ in the form

$$\frac{Fb(x,-\theta)+G-1}{Fb(x,-\theta)+G+1}=\frac{Fb(0,-\theta)+G-1}{Fb(0,-\theta)+G+1}\exp\{kx\}, \tag{7}$$

$$\frac{Fa(x,\theta)+G-1}{Fa(x,\theta)+G+1}=\exp\{-k(d+x)\}\frac{Fb(-d,-\theta)+G-1}{Fb(-d,-\theta)+G+1}, \tag{8}$$

$$k=\frac{\sqrt{\langle g\rangle^2+\langle f\rangle^2}}{\ell\cos(\theta)}, \quad F=\frac{\langle f\rangle}{\sqrt{\langle g\rangle^2+\langle f\rangle^2}}, \quad G=\frac{\langle g\rangle}{\sqrt{\langle g\rangle^2+\langle f\rangle^2}}.$$

From (7), (8) after a simple algebra we arrive at the boundary condition at the interface between the clean *d*-wave superconductor and disordered layer

$$a(0,\theta)=b(0,-\theta)\frac{(1-G\tanh(kd))}{(Fb(0,-\theta)+G)\tanh(kd)+1}+F\frac{\tanh(kd)}{(Fb(0,-\theta)+G)\tanh(kd)+1}. \tag{9}$$

Equation (9) describes the fact that the amplitude of anomalous Green's function along outgoing trajectories, $a(0,\theta)$, consists of two parts. The first, specular part is proportional to $b(0,-\theta)$ and describes the correlation between with the incoming $-\theta$ and reflected θ trajectories. The second, diffusive part is proportional to F and describes an average contribution of all the incident trajectories to the outgoing one in the θ direction.

In the limit of weak disorder ($d\ll\ell$) the boundary condition (9) reduces to the specular one (6). At finite d there is a cone of angles $\arccos d/\ell\leqslant\theta\leqslant\pi/2$ in which the scattering from the interface is diffusive rather than specular. The larger the value of d, the smaller the correlation between the incoming and outgoing trajectories.

In the limit of strong disorder ($d\gg\ell$) the solutions (7), (8) transform to those of Usadel equations obtained in Ref. 7, and it follows from (9) that

$$a(0)=\frac{\langle f(0,\theta)\rangle}{1+\langle g(0,\theta)\rangle}. \tag{10}$$

This is exactly the condition used previously in Ref. 7 for the analysis of strongly disordered *d*-wave interfaces. According to this condition the incoming and outgoing trajectories at a rough interface with strong disorder are completely uncorrelated as a result of the scattering from the impurity layer.

It is straightforward to find self-consistent solutions of the set of equations (2)–(5), (9). First, we have numerically integrated the equation (2) for $b(x)$ with the initial condition (5) along the trajectory from $x=+\infty$ (bulk) to $x=0$ (interface). Then the equation (3) for $a(x)$ was integrated from $x=0$ to $x=+\infty$ with the initial condition (9). The angle averages $\langle f(0)\rangle$ and $\langle g(0)\rangle$ and the pair potential $\Delta(x)$ were calculated iteratively.

We have applied this model for calculation of the low-temperature conductance of an NID tunnel junction, which is expressed in terms of the surface density of states $N(0,\theta)$ as

$$R_N dI/dV=\frac{\int_{-\pi/2}^{\pi/2}N(0,\theta)D(\theta)\cos\theta d\theta}{\int_{-\pi/2}^{\pi/2}D(\theta)\cos\theta d\theta}, \tag{11}$$

where R_N is the normal state junction resistance and $D(\theta)$ is the barrier transmission coefficient. The angle-resolved surface density of states is given by $N(0,\theta;\varepsilon)=\mathrm{Re}(g(0,\theta;\omega=-i\varepsilon))$.

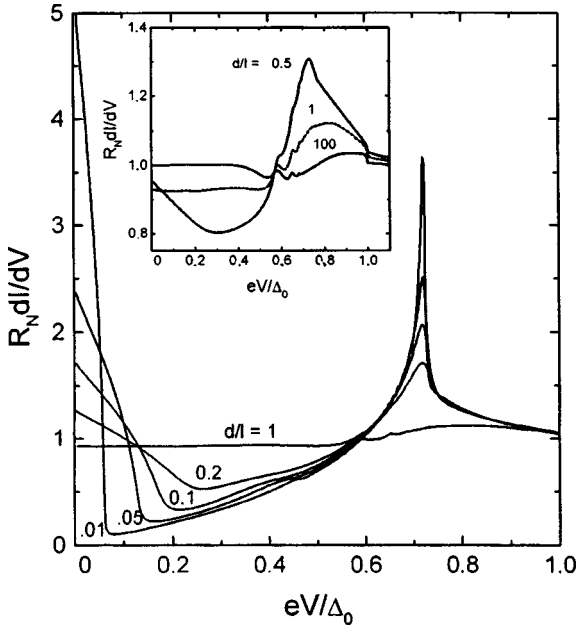

FIG. 1. Smearing of the ZBA in the low-temperature conductance of an NID junction. The inset shows the oscillations for large d/ℓ due to the finite-energy Andreev bound states.

Figure 1 shows the results of calculations for $\alpha = 20°$ and various values of the surface scattering parameter d/ℓ. We have chosen a δ-function potential barrier with an angular dependence of the transmission $D(\theta) = D(0)\cos^2\theta$. The zero-bias anomaly (ZBA), which is a manifestation of the sign reversal of the d-wave pair potential, is strongly broadened with increase of d/ℓ. In the limit of weak disorder $d/\ell \ll 1$ the results exactly correspond to those of Ref. 3.

As d/ℓ increases, the ZBA is smeared out completely, while the signatures of finite-energy Andreev bound states are still present. The latter are due to quasiparticles trapped in the surface region with the reduced pair potential $\Delta(x)$. As is seen from Fig. 1, the angle-averaged density of states in the disordered layer is gapless and has a number of peaks at energies below the bulk pair potential. Note that for large values of d/ℓ there are several (weak) peaks corresponding to more than one bound state, in contrast to the case of a specular interface, where only a single bound state exists at finite energy.[3] This is because the average trajectory length of trapped quasiparticles, which determines the number of resonances, is larger than ξ_0 in the diffusive case. Mathematically this fact is described by the boundary condition (9).

Next we apply the model to the study the influence of surface roughness on the Josephson supercurrent in a tunnel junction based on d-wave superconductors (DID junction). The critical current is given by the expression[12,13]

$$eR_N I_c = \frac{\pi T \Sigma_{\omega>0} \int_{-\pi/2}^{\pi/2} [f_{1s}(\theta) f_{2s}(\theta) - f_{1a}(\theta) f_{2a}(\theta)] D(\theta) \cos\theta \, d\theta}{\int_{-\pi/2}^{\pi/2} D(\theta) \cos\theta \, d\theta}. \tag{12}$$

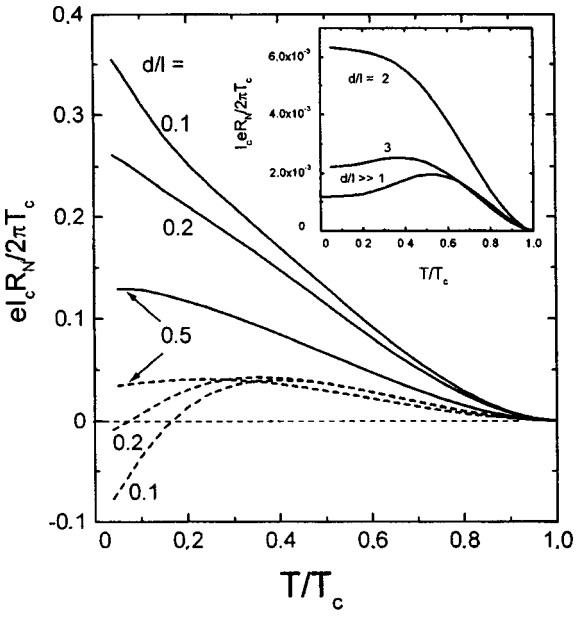

FIG. 2. Influence of surface roughness on the temperature dependence of the critical current in a DID tunnel junction. Dashed lines: symmetrical junction $\alpha_1=\alpha_2=20°$. Dotted lines: mirror junction $\alpha_1=-\alpha_2=20°$. Inset: nonmonotonic behavior of I_c for $d/\ell\gg 1$.

Here $f_{1,2s(a)}=(f_{1,2}\pm f_{1,2}^{+})/2$ and where $f_{1,2}$ are the surface Green's functions of the left (right) electrode.

The critical current was calculated numerically using the solutions for $f_{1,2}$ and assuming $D(\theta)=D(0)\cos^2\theta$. We consider two cases: 1) symmetric junction with the misorientation angles $\alpha_1=\alpha_2=20°$, 2) antisymmetric (mirror) junction with $\alpha_1=-\alpha_2=20°$. The results of calculations are shown in Fig. 2. In complete agreement with the results of Refs. 13–16, the mirror junction exhibits a nonmonotonic $I_c(T)$ dependence due to the anomaly $f_{1,2a}\sim 1/\omega_n$ at low frequencies, which is related to the midgap surface bound state. Like the ZBA in the conductance, this anomaly is smeared out with increasing surface scattering parameter d/ℓ.

In the strong scattering regime $d/\ell\gg 1$ the I_cR_N product of the DID junction becomes small and saturates at the level $eI_c^{SIS}R_N/2\pi T_c\sim 10^{-3}$ (the corresponding number for a conventional SIS junction is $eI_c^{SIS}R_N/2\pi T_c\simeq 0.44$). The anomalous contribution $f_{1a}f_{2a}$ vanishes in this case, and I_c for the symmetric and mirror junctions coincide. However, as shown in inset in Fig. 2, $I_c(T)$ becomes nonmonotonic as d/ℓ increases. The reason is the destructive interference within the impurity layer: the phases of Eilenberger functions on the incoming trajectories alternate due to the *d*-wave angular structure. As a result, the angle average $\langle f_{1,2}\rangle$ vanishes at $\omega_n\ll\pi T_c$, reaches a maximum at $\omega_n\sim\pi T_c$ and falls off as ω_n^{-2} at $\omega_n\gg\pi T_c$. It is the property $f_{1,2s}\to 0$ at small ω_n that is responsible for the decreasing $I_c(T)$ at low T. Variation of the misorientation angle α for $d/\ell\gg 1$ does not change the $I_c(T)$ behavior, while the product I_cR_N at $T=0$ scales as $\cos^2(2\alpha)$.

In conclusion, we have derived the boundary conditions for the Eilenberger functions at the rough surface of a *d*-wave superconductor and applied them to the study of the crossover from specular to diffusive surface scattering. The low-temperature conductance of an NID tunnel junction and the Josephson supercurrent in a DID tunnel junction have been calculated for arbitrary degree of surface roughness. We have shown that the width of the anomalies in the conductance and in the critical current is controlled by a single scattering parameter d/ℓ.

This work was supported in part by INTAS 93-790ext and by the Program for Russian–Dutch Research Cooperation (NWO).

[1] C.-R. Hu, Phys. Rev. Lett. **72**, 1526 (1994).
[2] Y. Tanaka and S. Kashiwaya, Phys. Rev. Lett. **74**, 3451 (1995); Phys. Rev. B **53**, 11957 (1996).
[3] Yu. S. Barash, A. A. Svidzinsky, and H. Burkhardt, Phys. Rev. B **55**, 15282 (1997).
[4] M. Fogelström, D. Rainer, and J. A. Sauls, Phys. Rev. Lett. **79**, 281 (1997).
[5] Yu. N. Ovchinnikov, Zh. Éksp. Teor. Fiz. **56**, 1590 (1969) [Sov. Phys. JETP **29**, 853 (1969)].
[6] F. J. Culetto, G. Kieselmann, and D. Rainer, in *Proceedings of the 17th International Conference on Low Temperature Physics*, edited by U. Eckern, A. Schmid, W. Weber, and H. Wühl, North Holland, Amsterdam, 1984, p. 1027.
[7] A. A. Golubov and M. Yu. Kupriyanov, JETP Lett. **67**, 501 (1998).
[8] N. B. Kopnin, P. I. Soininen, and M. M. Salomaa, Low Temp. Phys. **85**, 267 (1991).
[9] G. Eilenberger, Z. Phys. **214**, 195 (1968).
[10] N. Schopohl and K. Maki, Phys. Rev. B **52**, 490 (1995); N. Schopohl, http://xxx.lanl.gov/abs/cond-mat/9804064.
[11] E. Schachinger, J. P. Carbotte, F. Marsiglio, Phys. Rev. B m **56**, 2738 (1997).
[12] A. V. Zaitsev, Zh. Éksp. Teor. Fiz. **86**, 1742 (1984) [Sov. Phys. JETP **59**, 1015 (1984)].
[13] Yu. S. Barash, H. Burkhardt, and D. Rainer, Phys. Rev. Lett. **77**, 4070 (1996).
[14] Y. Tanaka and S. Kashiwaya, Phys. Rev. B **56**, 892 (1997).
[15] M. P. Samanta and S. Datta, Phys. Rev. B **55**, R8689 (1997).
[16] R. A. Riedel and P. F. Bagwell, Phys. Rev. B **57**, 6084 (1998).

Published in English in the original Russian journal. Edited by Steve Torstveit.

Strong and weak modes in polytypes of SiC

L. A. Fal'kovskiĭ
L. D. Landau Institute of Theoretical Physics, Russian Academy of Sciences, 117334 Moscow, Russia;
Groupe d'Etudes des Semiconducteurs, 34095 France

J. Camassel
Groupe d'Etudes des Semiconducteurs, 34095 France

(Submitted 14 January 1999)
Pis'ma Zh. Éksp. Teor. Fiz. **69**, No. 3, 247–250 (10 February 1999)

The concept of an extended Brillouin zone is used to analyze the intensity of phonon modes observed in optical and Raman investigations of different polytypes of silicon carbide. It is shown that the relative intensity of these modes agrees with the magnitude of the splitting of the doublets, which are degenerate in the extended zone. © *1999 American Institute of Physics.* [S0021-3640(99)01803-4]

PACS numbers: 78.30.Hv, 63.20.Dj

1. Different polytypes of silicon carbide differ by the sequence of layers in a direction perpendicular to the trigonal axis.[1] The most symmetric, cubic polytype $3C$-SiC possesses the zinc blende structure (space group $\mathbf{T}_d^2; F\bar{4}3m$) with two atoms per unit cell. The sequence of layers of atoms of one kind, for example Si, in it can be represented as ABCABC..., where the atoms in the A layer (see Fig. 1) form a close-packed triangular lattice, the B atoms lie in the next layer like billiard balls, and the third layer, C, is obtained from the B layer by a screw rotation by 60° around the trigonal axis passing through one of the A atoms. The atoms of the third layer in close packing can also be placed above the atoms of the A layer. In that case the $2H$ polytype with the layer sequence ABAB... (space group $\mathbf{C}_{6v}^4; C6mc$) will arise. In the existing hexagonal polytypes $4H$ and $6H$ the sequences of layers in one period can be represented as ABCB and ABCACB. Rhombohedral polytypes (space group $\mathbf{C}_{3v}; R3m$), for example, $15R, 21R$, and, with a very large period, $594R$, are also known.

The existence of polytypes with a very large period on the atomic scale presents a serious problem. It is difficult to explain why the layers, after disordered alternation within several hundred atomic layers, once again become strictly disordered in the next period of the crystal structure. It is obvious that the physical properties should differ very little between the various polytypes. From this standpoint, it is important that the immediate environment (two coordination spheres of any atom) is the same in all polytypes. In the present letter we shall take as an established fact that there is a small difference between various polytypes, and we shall see how some of their properties, determined by the dynamics of the crystal lattice, are related with this assumption.

2. Detailed information about the dynamic properties of the polytypes was obtained

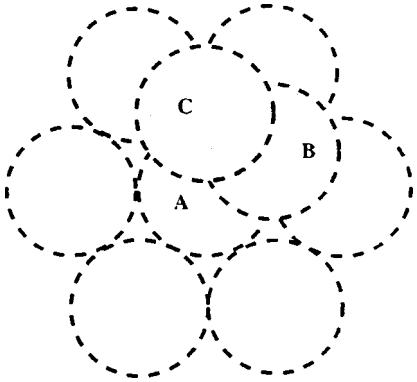

FIG. 1. Alternation of layers of atoms of one kind in the polytype 3*C*-SiC (face-centered cubic lattice) in the direction of the trigonal axis. The atoms of the layer A form a close-packed triangular lattice, above whose voids atoms of the next layer B lie. The atoms C are obtained from B by a screw rotation by 60° around an axis passing through A.

by studying the Raman scattering of light. The interpretation of these spectra can be simplified by using the concept of an extended Brillouin zone, which dates back to Patrick.[2] The first Brillouin zone for any polytype is obtained by folding the extended zone, which can be taken as the Brillouin zone of the cubic polytype, in a trigonal direction. Indeed, the elementary vectors $\mathbf{a}_1$ and $\mathbf{a}_2$ of the triangular lattice and the vector $\mathbf{a}_3$ in a trigonal direction for a polytype with n layers can be expressed in terms of an orthogonal basis: $\mathbf{a}_1=a_0(\bar{1}01)$, $\mathbf{a}_2=a_0(0\bar{1}1)$, and $\mathbf{a}_3=2an(111)/3$, where a_0 and a determine the interatomic distance $\sqrt{2}a_0$ in the layer and the distance $2a/\sqrt{3}$ between layers, respectively. The reciprocal-lattice vectors are $\mathbf{b}_1=2\pi(\bar{2}11)/3a_0$, $\mathbf{b}_2=2\pi(1\bar{2}1)/3a_0$, and $\mathbf{b}_3=\pi(111)/an$. For all polytypes a is very close to a_0, on account of which the interatomic distances are the same both within a layer and between layers. For the cubic polytype the lattice is face-centered with the vectors $\mathbf{a}_1^c=a_0(011)$, $\mathbf{a}_2^c=a_0(101)$, and $\mathbf{a}_3^c=a_0(110)$ in the direct lattice and, respectively, $\mathbf{b}_1^c=\pi(\bar{1}11)/a_0$, $\mathbf{b}_2^c=\pi(1\bar{1}1)/a_0$, and $\mathbf{b}_3^c=\pi(11\bar{1})/a_0$ in the reciprocal lattice. Since $\mathbf{b}_1^c+\mathbf{b}_2^c+\mathbf{b}_3^c=n\mathbf{b}_3$, the Brillouin zone of the cubic polytype, folded n times in a trigonal direction, gives the first zone of the corresponding hexagonal or rhombohedral polytype (in the latter case n is one-third the number multiplying R and denotes the number of layers in a rhombohedral cell).

Under such folding, shown schematically in Fig. 2 for 4*H*-SiC, the number of phonon modes increases by a factor of n (with a prescribed wave vector $\mathbf{q}$) in accordance with the fact that the number of atoms per unit cell increases, while the frequencies themselves remain almost unchanged. New frequencies appear, in particular, at the center of the Brillouin zone ($q=0$), and an additional term arises in the macroscopic response to a slowly varying perturbation. This means that, for example, new lines appear in the dielectric susceptibility or Raman scattering. These lines are weak (compared with the existing lines for the cubic polytype) in proportion to the potential $V(\mathbf{r})$ that leads to folding of the zone and the change in frequencies. It is of interest to calculate the change in the phonon frequencies and the intensity of weak modes.

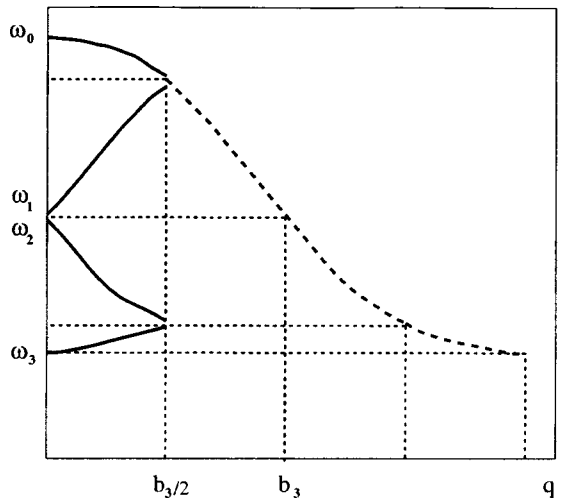

FIG. 2. Diagram of the folding of the extended zone into the Brillouin zone of the polytype 4*H*-SiC in the trigonal direction with elementary vector $\mathbf{b}_3$. The dashed line shows the initial phonon branch. The solid lines show the branches obtained by translations by $\mathbf{b}_3$ or $2\mathbf{b}_3$ and reflections $\mathbf{q}\rightarrow-\mathbf{q}$ into the Brillouin zone $(-\mathbf{b}_3/2,\mathbf{b}_3/2)$. Also shown is the splitting of the frequencies which are degenerate on the boundary of the new zone and at the center (ω_1 and ω_2).

3. Let us introduce the characteristic vibrations $|\alpha,\mathbf{q}\rangle$ of the dynamical equations of the lattice of the cubic polytype and the corresponding frequencies $\omega^\alpha(\mathbf{q})$, where the index α enumerates the modes with fixed $\mathbf{q}$. For example, two transverse and one longitudinal mode, corresponding to the representations E and A of the group $\mathbf{C}_{3v}$, are present in the trigonal direction. When the potential $V(\mathbf{r})$ is switched on, the vectors $\mathbf{q}$ and $\mathbf{q}+m\mathbf{b}_3$ become equivalent in the reciprocal lattice of the n polytype, where m assumes n integer values.

For simplicity, let us consider, for example, the polytype $4H$. The following modes of the cubic polytype correspond to the fixed vector $\mathbf{q}$: $u_0^\alpha=|\alpha,\mathbf{q}\rangle$, $u_{1,2}^\alpha=|\alpha,\mathbf{q}\mp\mathbf{b}_3\rangle$, and $u_3^\alpha=|\alpha,\mathbf{q}-2\mathbf{b}_3\rangle$ with the characteristic frequencies $\omega_0^\alpha=\omega^\alpha(\mathbf{q})$, $\omega_{1,2}^\alpha=\omega^\alpha(\mathbf{q}\mp\mathbf{b}_3)$, and $\omega_3^\alpha=\omega^\alpha(\mathbf{q}-2\mathbf{b}_3)$.

We want to calculate the response to a slowly varying field. For this reason, we are interested in the limit $\mathbf{q}\rightarrow0$. Then the modes $u_{1,2}^\alpha$ correspond to the same value of the frequency ($\omega_1^\alpha=\omega_2^\alpha$), since the quasimomenta differ only by the sign of the quasimomentum (in the zinc blende lattice there is no spatial inversion but there is time reversal, under which the quasimomentum changes sign).

We seek a solution in the form of the expansion

$$u(\mathbf{r})=\sum_{n,\alpha} C_n^\alpha u_n^\alpha .$$

If the frequency of the field (in the case of Raman scattering, the transferred frequency) is close to ω_1^α, then only the coefficients C_0^α and $C_{1,2}^\alpha$ need be retained in the equations

of motion. In the case of longitudinal oscillations the index α assumes only one value and can be dropped, assuming an interaction only with the nearest longitudinal vibrations. Then the equations of motion can be written in the form

$$\begin{aligned}
&(\omega_0^2+V_{00}-\omega^2)C_0+V_{01}C_1+V_{02}C_2=d,\\
&V_{10}C_0+(\omega_1^2+V_{11}-\omega^2)C_1+V_{12}C_2=0,\\
&V_{20}C_0+V_{21}C_1+(\omega_3^2+V_{11}-\omega^2)C_2=0,
\end{aligned} \tag{1}$$

where $V_{nm}=\langle u_n|V(\mathbf{r})|u_m\rangle$ are the matrix elements of the potential $V(\mathbf{r})$, and the right-hand side d is determined by the type of field to which a response is calculated. In the case of Raman scattering

$$d=\langle u_0|\,\gamma_{jk}e_j^{(i)}e_k^{(s)}\exp(i\mathbf{q}\cdot\mathbf{r})\rangle, \tag{2}$$

where $e_j^{(i)}$ and $e_k^{(s)}$ are, respectively, the polarizations of the incident and scattered light, and γ_{jk} is a tensor with the allowed symmetry. We underscore that the inhomogeneity d is present only in the first equation of the system (1), since the wave vectors of the incident and scattered light are small ($q\ll b_3$).

The intensity I of the scattered light is proportional to the imaginary part of the long-wavelength response, i.e., C_0. Finding C_0 from Eqs. (1) and expanding the solution in powers of the ratio of the potential $V(\mathbf{r})$ to the frequency dispersion in the zone $|\omega_1-\omega_0|$, we obtain

$$I\simeq\frac{|d|^2\omega}{1-\exp(-\hbar\omega/k_BT)}\,\mathrm{Im}\left(\frac{1}{\tilde{\omega}_0^2-i\omega\Gamma_0-\omega^2}+\frac{f_1}{\tilde{\omega}_1^2-i\omega\Gamma_1-\omega^2}+\frac{f_2}{\tilde{\omega}_2^2-i\omega\Gamma_1-\omega^2}\right), \tag{3}$$

where $\tilde{\omega}_m$ are the frequencies renormalized by the potential $V(\mathbf{r})$. The splitting of the degenerate frequency is most important here:

$$\tilde{\omega}_{1,2}^2=\omega_1^2+V_{11}\pm|V_{12}|. \tag{4}$$

The oscillator strengths $f_{1,2}$ are proportional to the squared potential

$$f_{1,2}=\frac{|V_{01}|^2}{(\omega_0^2-\omega_1^2)^2}\left(1\pm\mathrm{Re}\,\frac{V_{12}V_{01}^2}{|V_{12}V_{01}^2|}\right) \tag{5}$$

and determine the total intensities for each component of a doublet with respect to the corresponding intensity of the line ω_0 existing even before the zone is folded. The width Γ is taken into account in expression (3). It must be assumed to be independent of $V(\mathbf{r})$ to a first approximation. For this reason, the components of the doublet have the same width.

We note that there are only two terms in the intensity of the scattered light with excitation of the nondegenerate line ω_3^α (in Eq. (3) the substitution $f_{1,2}\to f_3$ must be made), and the second term is absent in the formula for the oscillator strength (5).

An expression for the electric susceptibility can be obtained similarly. It differs only by the form of the driving force (2).

4. As one can see from Eq. (5), the total, i.e., independent of the width Γ, intensity (3) of the weak lines, which end up at $q=0$ as a result of the folding of the extended zone is proportional to the ratio of the squared potential to the variation of the frequency in the zone $\delta\omega\sim|\omega_0-\omega_1|$, while the doublet splitting $\Delta=|\tilde{\omega}_1-\tilde{\omega}_2|$ is proportional to the first power of the potential (4). The doublet splitting was observed for some polytypes and is about $5\ \mathrm{cm}^{-1}$, and the dispersion of the optical modes is of the order of $100\ \mathrm{cm}^{-1}$. Therefore the relative strength of the potential is 5×10^{-2}, and this means that the relative total intensity of the weak lines should be of the order of 3×10^{-3}. In Ref. 2 (see also Ref. 3) it is asserted that the relative intensities of the weak modes are 10^{-3} in infrared absorption and 10^{-2} in Raman scattering. We note that although these values are close to our estimate presented above, they should be identical.

As one can see from Eq. (3), the differential intensity also depends on the width Γ, which should be the same for the components of a doublet. There is no experimental information about this. The only fact[4] known to us is that in the infrared absorption in the polytype $6H$ the widths of the lines in the doublet $883.3\ \mathrm{cm}^{-1}$ and $888.6\ \mathrm{cm}^{-1}$ are, respectively, $1.6\ \mathrm{cm}^{-1}$ and $1.85\ \mathrm{cm}^{-1}$, while the relative oscillator strength differs by a larger amount: 1.9×10^{-3} and 1.25×10^{-3}.

This work was supported in part by the Russian Fund for Fundamental Research, Grant 97-02-16044, and by a NATO grant.

[1] R. W. G. Wyckoff, *Crystal Structures*, Vol. 1, 2nd ed., Interscience, New York, 1963, pp. 108, 113.
[2] Lyle Patrick, Phys. Rev. **167**, 809 (1968); D. F. Feldman, James H. Parker Jr., W. J. Choyke, and Lyle Patrick, Phys. Rev. **170**, 698 (1968); Phys. Rev. **173**, 787 (1968).
[3] S. Nakashima, H. Katahama, Y. Nakakura, and A. Mitsuishi, Phys. Rev. B **33**, 5721 (1986).
[4] J. M. Bluet, K. Chourou, M. Anikin, and R. Madar, *SiC and Related Materials*, Intern. Conf. Montpellier, 1998.

Translated by M. E. Alferieff

Kinetics of muonium formation in liquid helium

E. L. Kosarev*
P. L. Kapitsa Institute of Physics Problems, Russian Academy of Sciences, 117334 Moscow, Russia

E. P. Krasnoperov**
Kurchatov Institute Russian Science Center, 123182 Moscow, Russia

(Submitted 16 December 1998; resubmitted 11 January 1999)
Pis'ma Zh. Éksp. Teor. Fiz. **69**, No. 3, 251–256 (10 February 1999)

The spatial distribution of electron–muon pairs in superfluid helium (He-II) is determined using a new algorithm for reconstructing the muonium (Mu) formation probability. It is shown that because a gap is present in the excitation spectrum of He-II the thermalization time of muons and secondary electrons increases with decreasing temperature. As a result, the average distance in the electron–muon pairs increases and, correspondingly, the muonium formation rate decreases. © *1999 American Institute of Physics.* [S0021-3640(99)01903-9]

PACS numbers: 36.10.Dr, 67.40.−w

1. It is known that a muonium atom $Mu=\mu^{+}+e^{-}$ forms in liquid helium when a muon and an electron of the track recombine.[1,2] A positively charged particle in helium forms a small ''chunk'' with an associated mass $M_{+}\simeq 50$ helium atoms, and the electron is localized in a cavity whose hydrodynamic mass is $M_{-}\simeq 200$ helium atoms (see the review Ref. 3 and also Ref. 4). On account of the large masses the time of approach of the charges and the formation of Mu in liquid helium are much longer than in other substances. In the simplest model[5,6] the interaction of a muon and a track electron is assumed to be the Coulomb interaction, and the viscous regime of approach, $dv/dt\simeq 0$, with the total relative mobility of the two charges $b=b_{+}+b_{-}$, is studied. In a constant electric field, viscous motion

$$dr/dt=-b\cdot\nabla\phi \tag{1}$$

(here ϕ is the interaction potential) is established in a time $\tau_v=Mb/e$, called the velocity relaxation time. For a Coulomb field the motion can be taken as viscous if the relative change in the field over the time τ_v, viz., $\Delta E/E=2v\tau_v/r=2b^2M/r^3$, is small . At low temperatures an electric field $E_c=50-100$ V/cm disrupts the formation of muonium.[7] This corresponds to distances $r>(e/E_c)^{1/2}$ and for 10% accuracy gives an upper limit on the mobility $b\simeq 5-15$ cm^2/V·s. Since the Mu formation time is several orders of magnitude longer than τ_v, Eq. (1) can be used to describe the approach of the charges at temperatures to 0.7–0.8 K. These approximate considerations are confirmed by comparing the results of a direct calculation of the closing time of the charges on the basis of both Eq. (1) and the complete equations of motion: The difference does not exceed several percent at 0.7 K, and it is even smaller as temperature increases.

For a Gaussian spatial distribution of the charge the polarization function is close to $\exp(-kt)$.[6] This often justifies describing the formation of muonium by a first-order equation characteristic for chemical reactions.[8] In superfluid helium the conventional approach is unsatisfactory for the following reason. If in the equation (1) of viscous approach of the charges toward each other the new independent variable $t^*=bt$ is introduced instead of the time t, then the mobility vanishes from the equation, and correspondingly the polarization function should be universal for all temperatures.

However, in the experiment of Ref. 1 it is shown that at least two exponentials, the ratio of whose amplitudes is temperature-dependent, is required in order to obtain the best fit of the muonium polarization function $P(t)$. Actually, the form of the function $P(t^*)$ depends on the temperature and therefore it is not universal.

Let $n(t)$ be the muonium formation probability as a function of time. Since half the polarization (in the S state) is not observed during the formation of muonium, in a zero magnetic field the muon polarization can be written as a sum of two integrals

$$P_{Mu}(t)=\frac{1}{2}\int_0^t n(t')dt'+\int_t^\infty n(t')dt', \tag{2}$$

which have a clear physical meaning. The first integral refers to muonium atoms in the triplet state ($\uparrow\uparrow$) which have formed by the time t, while the second integral corresponds to free muons which have not yet recombined into muonium atoms.

Let us now consider a weak transverse magnetic field, such that the rotation of the free muon spin over its lifetime can be neglected. For liquid nitrogen, typically, $H\leqslant 0.4$ Oe. The spins of the muonium atoms formed at the time t' start to precess with frequency Ω_{Mu} and with a phase delay $\Omega_{Mu}t'$, and the polarization function will have two terms

$$P(t)=\frac{1}{2}\int_0^t n(t')\cos\Omega_{Mu}(t-t')dt'+\int_t^\infty n(t')dt', \tag{3}$$

where the first term describes the precession of the Mu spins at the Larmor frequency Ω_{Mu} and with a delay t', while the second term describes free muons, for which the direction of the spins remains virtually unchanged because of the weakness of the magnetic field.

The main information about $P(t)$ is ordinarily extracted by approximating histograms of the positron counts by a model polarization function.[8] The true form of the function $P(t)$ and, correspondingly, $n(t)$ remain unknown. In the present letter we employ a new algorithm for determining the function $n(t)$ by solving the integral equation (3) using the RECOVERY software package to reconstruct the signals.[9] A detailed description of the effective possibilities of this package can found in Ref. 10.

2. In μSR experiments the directly measured quantity is the so-called histogram $N(t)$:

$$N(t)=N_0[1-A_0\cdot P(t)]e^{-t/t_\mu}+B, \tag{4}$$

which actually determines the number of positrons arising in time with the decay of a positive muon. In this formula $t_\mu=2.197\times 10^{-6}$ s is the muon lifetime, N_0 is proportional to the intensity of the muon beam, A_0 is the initial asymmetry factor, and B is the

random-coincidence background. The polarization function $P(t)$ in Eq. (4) can be determined from the histogram $N(t)$ only after the numerical values of the parameters N_0, B, and A_0 have been determined. At temperatures below 1.35 K the muonium formation time is much shorter than the duration of the histogram. This makes it possible to determine these parameters by a simple method. When the process leading to the formation of muonium atoms is completed, the equation for the histogram has the form

$$N_1(t)=[A+C\cos(\Omega_{Mu}t)+D\sin(\Omega_{Mu}t)]e^{-t/t_\mu}+B. \tag{5}$$

The parameters A, B, C, and D are determined by minimizing the quantity

$$\chi^2=\sum_{t_i>t_0}\frac{[N(t_i)-N_1(t_i)]^2}{N(t_i)}. \tag{6}$$

This formula takes into account that the experimental data on $N(t)$ have a Poisson distribution.

After the parameters A, B, C, and D are determined, N_0 and the asymmetry A_0 are calculated using the formulas

$$N_0=A\exp(t_0/t_\mu),\quad A_{Mu}=\sqrt{C^2+D^2},\quad \text{and}\quad A_0=\frac{A_{Mu}}{A}. \tag{7}$$

Now that all the constants in Eq. (4) are known, this formula can be inverted, and the normalized polarization

$$P(t)=\frac{\hat{P}(t)}{\hat{P}(0)}, \tag{8}$$

where the normalization constant $\hat{P}(0)$ is an estimate of the value of the function $\hat{P}(t)$ at time $t=0$, obtained from a small number of initial values using an optimal filtering program, can be calculated.[11] Figure 1 shows the initial histogram $N(t)$ at $T=0.7$ K and the function $P(t)$. As one can see from this figure, the polarization $P(t)$ gradually moves away from the initial value $P(0)\simeq 1$ into a regime of uniform precession between the extreme values of the amplitudes $+1/2$ and $-1/2$. This corresponds to the fact, noted at the beginning of this letter, that after muonium is formed only half the initial polarization is observed.[8]

It is clearly evident in Fig. 1 that the noise level of the function $P(t)$ increases with t. We shall determine the noise level, starting from the fact that the histogram $N(t)$ has a Poisson distribution for which $\mathrm{var}\,[N(t)]=N(t)$. Assuming approximately that $N(t)\approx N_0e^{-t/t_\mu}$, we obtain from Eq. (8)

$$\mathrm{var}[P(t)]\approx\frac{1}{A_0^2N(t)(\hat{P}(0))^2}\approx\frac{1}{4A_0^2N(t)}. \tag{9}$$

The equation (9) for estimating the noise level in the function $P(t)$ is used in the algorithm studied in the present letter.

We note that coefficients in expression (4) can also be found by the conventional method, adopted in μSR, using a parametric approximation of the function $P(t)$ (helium requires at least two exponentials). However, this method can be successfully used only

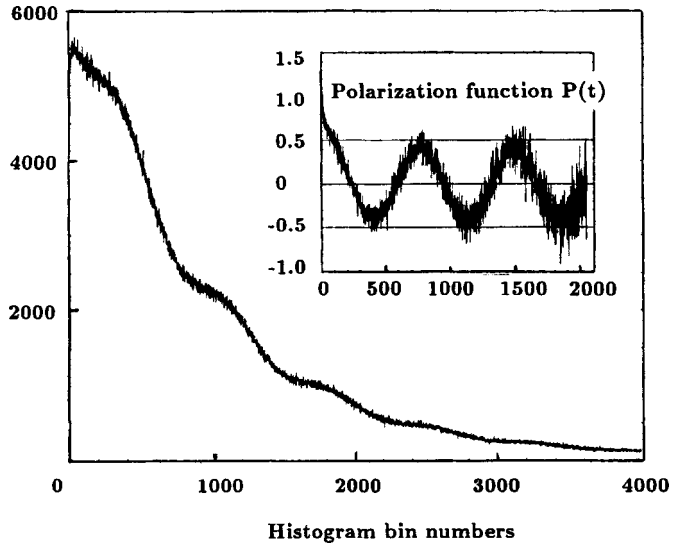

FIG. 1. Histogram $N(t)$ and precession function $P(t)$ of muonium in a magnetic field $H=0.4$ G and liquid helium temperature $T=0.7$ K. The channel width is 2.5 ns.

if reliable physical information about the form of the function $n(t)$ and, correspondingly, $P(t)$ is available. However, a nonparametric approach is better when the aim is to analyze these functions.

The equation (3) can be written in the equivalent form

$$P_1(t)=\int_0^t n(t')\left[\frac{\cos\Omega_{Mu}(t-t')}{2}-1\right]dt', \tag{10}$$

where $P_1(t)=P(t)-1$. The equation (10) is a convolution-type Volterra integral equation of the first kind for determining the nonnegative function $n(t)$ from the input data $P_1(t)$ with the kernel $K(t-t')$ determined by the expression in the brackets in Eq. (10).

Introducing the modified kernel $K_1(t-t')$

$$K_1(t-t')=\begin{cases} K(t-t'), & t'\leqslant t, \\ 0, & t'>t, \end{cases} \tag{11}$$

reduces Eq. (10) to a Fredholm integral equation with fixed integration limits. This equation can be solved using the DCONV2 program from the RECOVERY package.

The analysis of the errors and examples of the reconstruction of model functions which were performed in Ref. 12 showed that the method gives an average error of less than 2% in the function $n(t)$ with a total data sample $\sim 6\times 10^6$ events in the histogram.

3. The results of reconstructing the function $n(t)$ from histograms of the precession of muonium in a field $H=0.4$ Oe are presented in Fig. 2. As the temperature decreases, the recombination rate on the initial segment $t<0.3\,\mu$s increases, and at long times ($t>0.5\ \mu$s) the lower temperature, the lower the rate is. At $T=0.7$ K virtually the entire recombination process is completed in the initial interval. As the temperature decreases

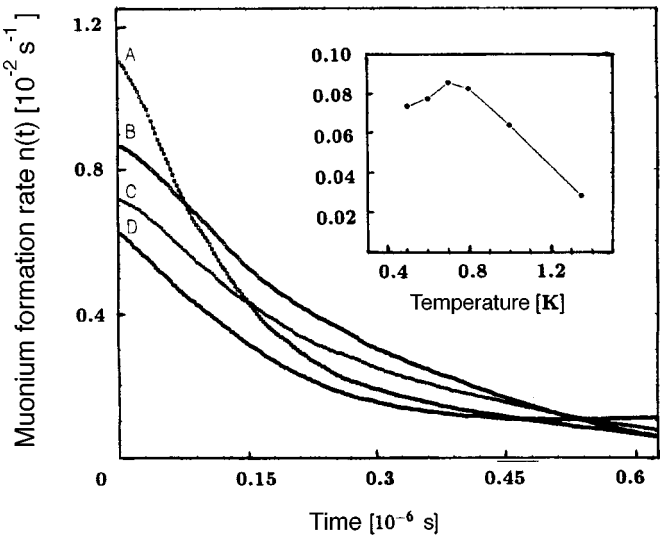

FIG. 2. Muonium formation rate $n(t)$ at various temperatures: *A:* $T=0.5$ K; *B:* $T=0.8$ K; *C*: $T=1$ K; *D*: $T=1.35$ K. Inset: Temperature dependence of the muonium precession amplitude A_{Mu} calculated from Eqs. (7).

further, a long-time component reappears, though $n(0)$ once again increases. Here a nonmonotonic temperature variation of the form of the function $n(t)$ is most clearly manifested. After constructing $n(t)$ in logarithmic coordinates, it can be verified that the recombination rate is not a simple exponential. The values of A_{Mu}, calculated using Eq. (7) and shown in the inset in Fig. 2, attest to the nonmonotonic character of the temperature dependence of $n(t)$. These values are virtually identical to the results obtained in Ref. 5.

Let us introduce the density function $W(r)$ for the initial spatial distribution of muon–electron pairs. In the problem of the viscous closing of the particles on one another, the initial radial distribution of the pairs corresponds to the condition that the process of thermalization of the ionized particles has been completed and their velocity vector $V=-b\nabla\phi$ has been established along the electric field lines. If for simplicity the spatial asymmetry of the distribution function $W(r)$ found in Ref. 7 is neglected, then instead of Eq. (2) the polarization can be written in the form

$$P(t)=1-2\pi\int_0^{r(t)} W(\xi)\xi^2 d\xi. \tag{12}$$

Since $dP/dt=V\cdot dP/dr$, it is easy to find from Eqs. (1) and (12) a relation between the recombination probability and the initial pair distribution density

$$n(t)=4\pi be W(r)r^2\cdot V. \tag{13}$$

In this formula it is assumed that for a purely Coulomb attraction the velocity is $V=eb/r^2$ and the corresponding pair recombination time as a function of distance r is $t=r^3/3be$. Figure 3 shows the function $W(r)$ for different temperatures in the range $0.7\text{ K}\leqslant T\leqslant 1.35$ K. One can see that as temperature decreases, the average interparticle

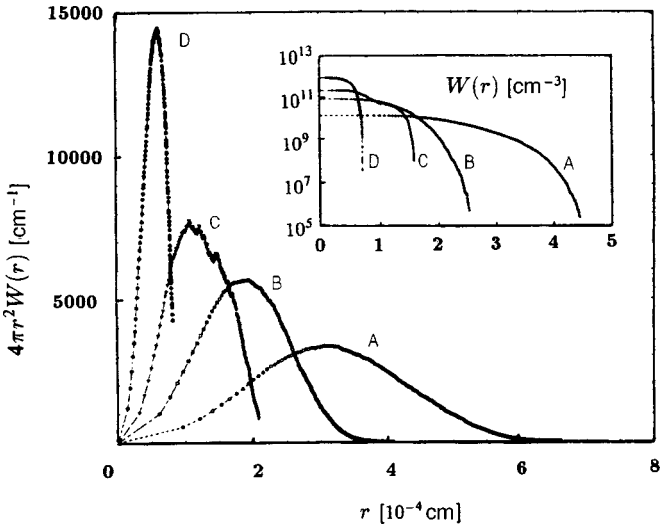

FIG. 3. Radial distribution function $4\pi r^2 \cdot W(r)$ of muon–electron distances at various temperatures. *A*: $T=0.7$ K; *B*: $T=0.8$ K; *C*: $T=1$ K; *D*: $T=1.35$ K. Inset: $W(r)$ on a logarithmic scale for the same temperatures as in the main plot. The distance in units of 10^{-4} cm is plotted along the abscissa in both plots.

distance and its variance increase. In an ordinary condensate the thermalization of particles due to elastic collisions (phonons) is completed in a time 10^{-12}–10^{-10} s. A gap of the order of $\delta=8$ K is present in the excitation spectrum of superfluid helium,[13] as a result of which the mobility of the impurity particles is anomalously high. When the kinetic energy of the charges drops below 8 K, the scattering probability drops sharply and the velocity relaxation time τ_v increases. Evidently, as a result, the average electron–muon distance increases with decreasing temperature. Assuming that before viscous closing is established the impurity particles move with velocity close to the Landau critical velocity, $V_L \simeq 60$ m/s,[13] the order of magnitude of the additional separation is $R \approx V_L \cdot \tau_v$.

Analysis shows that the character of the separation is more complicated. Figure 4 shows the squared position $R^2_{\max}$ of the maximum of the distribution function as a function of the relative mobility of the muon and the electron at this temperature. It is easy to see that the dependence is linear $R^2_{\max} \propto b$ to a high degree of accuracy. Since the mobility b is proportional to τ_v, this dependence reflects the random diffusive character of the low-temperature thermalization of the charges. At temperatures below 0.7 K the separation of the particles become so large that some of them fall outside the Onsager radius $r_c = e^2/\epsilon k_B T$, where ϵ is the dielectric constant and k_B is Boltzmann's constant. The probability of recombination of these muon–electron pairs is small, and a free (muon) fraction appears as a result.

Although, as one can see in Fig. 2, the initial formation rate of muonium increases with decreasing temperature, the total muonium asymmetry decreases. The decrease of A_{Mu} below 0.7 K is due to the fact that its formation time is $\tau_{Mu} \simeq (\gamma_{Mu} H)^{-1} \simeq 0.2$ μs. In this interval $n(0)$ increases but the integral

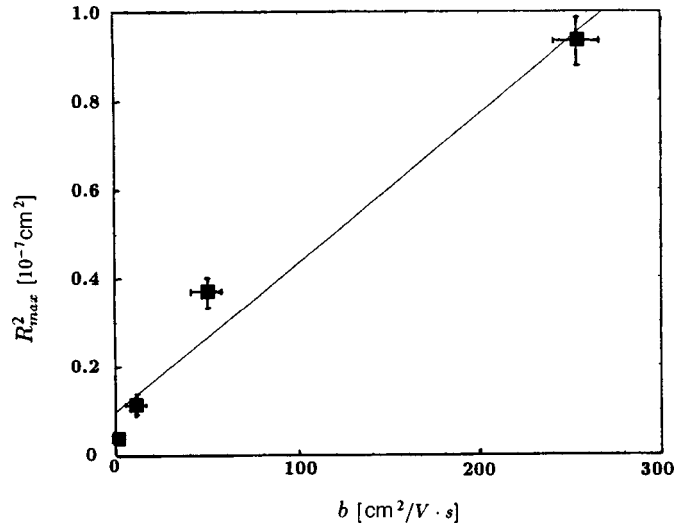

FIG. 4. Squared average separation in muon–electron pairs versus the relative mobility.

$$A_{Mu}=\int_0^{\tau_{Mu}} n(t)dt$$

decreases with decreasing temperature.[5]

In summary, a direct reconstruction of the muonium formation rate in superfluid helium shows that the absence of universality of the function $P(t)$ as a function of temperature (its scaling) is due to an increase in the average interparticle distance in the muon–electron pairs in the process of velocity relaxation.

We thank S. S. Zuev and V. P. Zhigulin for assisting in the calculations. This work was partially performed as part of Project 98-02-16430 of the Russian Fund for Fundamental Research.

*e-mail: kosarev@kapitza.ras.ru
**e-mail: kep@isssph.kiae.ru

[1] E. P. Krasnoperov, V. G. Storchak, S. G. Barsov *et al.*, JETP Lett. **42**, 324 (1985).
[2] D. C. Walker, Mater. Sci. Forum **255-257**, 124 (1997).
[3] V. B. Shikin, Usp. Fiz. Nauk **121**, 457 (1977) [Sov. Phys. Usp. **20**, 226 (1977)].
[4] B. N. Esel'son, V. G. Ivantsov, V. A. Koval' *et al.*, in *Handbook of the Properties of Liquid and Solid Helium. $^3He-^4He$ Solutions* [in Russian], edited by B. N. Esel'son, Naukova Dumka, Kiev, 1982, p. 123.
[5] R. Abela, D. Gerlakh, E. P. Krasnoperov *et al.*, JETP Lett. **57**, 157 (1993).
[6] F. M. Jacobsen, Hyperfine Interact. **32**, 501 (1986).
[7] E. Krasnoperov, E. E. Meilikhov, D. Eschenko *et al.*, Hyperfine Interact. **87**, 1011 (1994).
[8] V. P. Smigla and Yu. M. Belousov, *The Muonium Method of Matter Research* [in Russian], Nauka, Moscow, 1991.
[9] V. I. Gelfgat, E. L. Kosarev, and E. R. Podolyak, Comput. Phys. Commun. **74**, 335 (1993).
[10] E. L. Kosarev, Inverse Probl. **6**, 55 (1990).
[11] E. L. Kosarev and E. Pantos, J. Phys. E **16**, 537 (1983).

[12] E. L. Kosarev and E. P. Krasnoperov, ''A new calculation technique of muonium formation rate,'' in *Proceedings of the Conference on Modern Trends in Computational Physics*, Dubna, June 1998.
[13] E. M. Lifshitz and L. P. Pitaevskiĭ, *Statistical Physics, Part 2, The Theory of the Condensed State*, Pergamon Press, New York [Russian original, Nauka, Moscow, 1978].

Translated by M. E. Alferieff